

AD-A157 040

SHIPBOARD ACOUSTIC CURRENT PROFILING DURING THE COASTAL
OCEAN DYNAMICS EXPERIMENT(U) SCRIPPS INSTITUTION OF
OCEANOGRAPHY LA JOLLA CA P M KOSRO MAY 85 SIO-REF-85-8

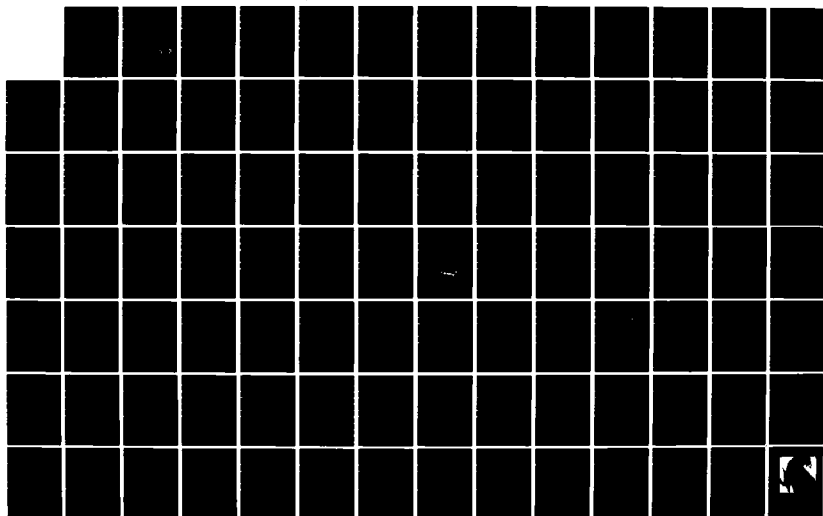
1/2

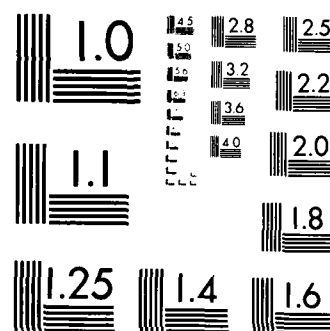
UNCLASSIFIED

N00014-80-C-0440

F/G 17/1

NL





MICROCOPY RESOLUTION TEST CHART
NATIONAL BUREAU OF STANDARDS-1963-A

AD-A157 040

SIO REFERENCE SERIES

SHIPBOARD ACOUSTIC CURRENT PROFILING DURING
THE COASTAL OCEAN DYNAMICS EXPERIMENT

by
P. Michael Kosro

DTIC
ELECTE
JUL 15 1985
G

DTIC FILE COPY

DISTRIBUTION STATEMENT A
Approved for public release
Distribution Unlimited

May 1985

SIO Reference No. 85-8

University of California

Department of Ocean

85 05 24 025

REPORT DOCUMENTATION PAGE		READ INSTRUCTIONS BEFORE COMPLETING FORM
1. REPORT NUMBER SIO Reference No. 85-8	2. GOVT ACCESSION NO. AD - A157040	3. RECIPIENT'S CATALOG NUMBER
4. TITLE (and Subtitle) SHIPBOARD ACOUSTIC CURRENT PROFILING DURING THE COASTAL OCEAN DYNAMICS EXPERIMENT		5. TYPE OF REPORT & PERIOD COVERED
		6. PERFORMING ORG. REPORT NUMBER
7. AUTHOR(s) P. Michael Kosro		8. CONTRACT OR GRANT NUMBER(s) N00014-80-C-0440
9. PERFORMING ORGANIZATION NAME AND ADDRESS Scripps Institution of Oceanography La Jolla, California 92093		10. PROGRAM ELEMENT, PROJECT, TASK AREA & WORK UNIT NUMBERS
11. CONTROLLING OFFICE NAME AND ADDRESS Office of Naval Research Arlington, Virginia 22217		12. REPORT DATE May 1985
		13. NUMBER OF PAGES 119
14. MONITORING AGENCY NAME & ADDRESS (if different from Controlling Office)		15. SECURITY CLASS. (of this report) Unclassified
		15a. DECLASSIFICATION/DOWNGRADING SCHEDULE
16. DISTRIBUTION STATEMENT (of this Report) Approved for public release. Distribution unlimited.		
17. DISTRIBUTION STATEMENT (of the abstract entered in Block 20, if different from Report)		
18. SUPPLEMENTARY NOTES		
19. KEY WORDS (Continue on reverse side if necessary and identify by block number)		
20. ABSTRACT (Continue on reverse side if necessary and identify by block number) The shipboard Doppler Acoustic Log (DAL) to be discussed in this study is a new tool for the measurement of ocean currents. By providing vertical profiles of currents over the upper 150m of ocean at points along the ship's path, it allows the ocean to be sampled in a way which is fundamentally different from moored current meters or drifters, the instruments most commonly used for current measurement. This instrument is used to examine the circulation in a region of strong coastal upwelling off Northern California, where it reveals an unexpectedly energetic and spatially complex synoptic flow ...		

SCRIPPS INSTITUTION OF OCEANOGRAPHY
UNIVERSITY OF CALIFORNIA, SAN DIEGO
LA JOLLA, CALIFORNIA 92093

Shipboard Acoustic Current Profiling During
the Coastal Ocean Dynamics Experiment

by

P. Michael Kosro

Accession For	
NTIS GRA&I	<input checked="checked" type="checkbox"/>
DTIC TAB	<input type="checkbox"/>
Unannounced	<input type="checkbox"/>
Justification	
By _____	
Distribution/	
Availability Codes	
Dist	Avail and/or Special
A/	

Prepared for the National Science Foundation under Grant No. OCE84-10546 and for the
Office of Naval Research under Grant No. N00014-80-C-0440.

Reproduction in whole or in part is permitted for any purpose of the United States Government.

May 1985

SIO Reference No. 85-8.

Table of Contents

List of Figures	
List of Tables	
Acknowledgements	
Vita, Fields of Study	
Abstract	
1. Introduction	1
2. Doppler Acoustic Log	5
3. Data Processing and Error Analysis	12
3.1. Instrumentation	12
3.2. LORAN-C	12
3.3. Thermistor	15
3.4. Data Valid Flag and Depth of Acoustic Measurements	16
3.5. Bottom Reflections	16
3.6. Acoustic Profiles of Relative Velocity in Ship's Coordinates	18
3.7. Rotation to Geographic Coordinates	24
3.7.1. Pitch and Roll	25
3.7.2. Heading	27
3.8. Calibration and Misalignment Errors	30
4. Estimation of Currents	33
4.1. Introduction	33
4.2. Spectrum of Measurements	34
4.3. Endpoint Estimator	37
4.4. Optimum Estimator	38
4.5. Least Squares Drift	40
4.6. Optimum Filtering	42
4.7. Vertical Current Profiles	44
4.8. Summary	44
5. Comparison with Moored Current Meters	46
5.1. Introduction	46
5.2. Comparison within 1 km	46
5.3. Comparison at Larger Separations	53
6. Acoustic Measurements of Coastal Upwelling Currents. Averages	57

6.2. Mean Fields	57
6.3. Discussion and Summary	60
7. Acoustic Measurements of Coastal Upwelling Currents. Surveys	75
7.1. Introduction	75
7.2. Synopticity	75
7.3. DAL Atlas	76
7.4. Wind Relaxation of April 1982	76
7.5. Jet Surveys. July 1981 and July 1982	78
Appendix : DAL Sampling at Hydrographic Stations	108
References	117

List of Figures

- Fig. 1.1 : Schematic view of coastal upwelling circulation (from Huyer 1983). 3
- Fig. 2.1 : The use of acoustic Doppler shift to measure the velocity of ships at sea dates back to this patent by C. Chilowski, submitted in 1924. Note the sophisticated 4 beam Janus design which is still used for first order pitch and roll compensation. 6
- Fig. 2.2 : Range Gated Shipboard Doppler System. Four beams (fore, aft, port and starboard) equally inclined from the ship's vertical axis acoustically probe the ocean. The Doppler shift in backscattered signal measures the relative velocity between ship and ocean. Range gating allows depth profiling of currents. 8
- Fig. 2.3 : A Doppler current profiler which has been bottom mounted for vertical profiling of local currents. 11
- Fig. 2.4 : Bottom mounted Doppler acoustic current measurements superimposed on mechanical current meter records (Pettigrew and Irish [1983]). 11
- Fig. 3.1 : Depth range of shipboard measurements is shown by the percent of pings for which the profiler electronics indicated valid returns at each range bin. Two 12 hour subsets of data are shown, one each from 1981 and 1982. Details of such validity profiles vary with many factors including location and time of day. 17
- Fig. 3.2 : Variability in acoustic measurements of relative velocity, shown as histograms of the deviations of single ping measurements from 100 ping average. 19
- Fig. 3.3 : Autospectra of ping-to-ping relative velocity measurements for 3 subsets of data taken at nearly constant shipspeed while (a) steaming into seas, (b) on station, and (c) steaming with following seas. Solid line is foreward velocity F, dashed line is portward velocity P. Note peak at surface wave encounter frequency rising above a white noise background. 21
- Fig. 3.4 : Coherence of F (solid) and P (dashed) with pitch ϕ and roll ρ of the ship. Data in left panels taken while on station (same as middle panel, Fig. 3.3); data in right panels taken while steaming into seas (same as upper panel, Fig. 3.3) 22

- Fig. 3.5 : Expected residual wave induced and white noise in acoustic measurements of relative velocity after block averaging, as a function of averaging length. 23
- Fig. 4.1 : Sample time series of measurements. Top panel shows the acoustically determined relative velocity \hat{V} , middle panel shows $d\hat{x}_0/dt$ from LORAN-C. Bottom panel shows the sum of these, the fix-to-fix current measurement \hat{u} . 35
- Fig. 4.2 : Spectrum of fix-to-fix current measurements for v (solid line, alongshore current, $317^\circ T$) and u (dashed line, cross-shore current, $47^\circ T$). 36
- Fig. 4.3 : Same as Fig. 4.2 except normalized by $\sin^2 \pi f \Delta t$. White noise in LORAN fixes yields a flat spectrum for fix-to-fix currents under this normalization. 36
- Fig. 4.4 : The mean square error in filtered fix-to-fix current estimates ($\text{cm}^2 \text{sec}^{-2}$) is predicted as a function of filter length (fix intervals) for 3 filters using Eq 4.39, the spectrum of measurements (Fig. 4.2) and the inferred noise spectrum. Increased estimation error at short filter length arises from underfiltering of noise, while rise at longer filter length arises from suppression of true signal. The least squares filter achieves its minimum mse most rapidly, while the Tukey and truncated sinc filters suppress less signal in the case of overfiltering (i.e. where the statistics of the signal deviate from the assumptions of the objective analysis). 43
- Fig. 5.1 : CODE 2 (1982) moored current meter array. Table 5.1 provides details on instrumentation at each mooring. Also shown is the location of wind buoy NDBO 46013. 47
- Fig. 5.2a : Comparison of all DAL current measurements (alongshore component) made within 1 km of a current meter mooring with the simultaneous current meter measurement. At both 20m and 35m depth, over 1000 pairs of measurements are plotted. See Table 5.2 for a statistical summary of these results. 51
- Fig. 5.2b : Same as Fig. 5.2a, except for cross-shore components. 52
- Fig. 5.3a : Average DAL cross-shore and along-shore currents u and v along the Central Line at depths of current meters (20m, 35m, 53m, and 70m), as a function of cross-shelf separation from the C3 mooring. Stars show current meter averages at C2, C3 and C4 over same sample times. Note the strong mean shear in v and divergence in u across the shelf. 54

Fig. 5.3b : Correlation between simultaneous DAL and C3 current meter currents as a function of cross-shelf separation from the C3 mooring. Dashed line gives 95% confidence level for correlation over available samples. Stars show C3 correlation with current meters at C2 and C4.	55
Fig. 5.3c : Root mean square difference between DAL and current meter currents as a function of cross-shelf separation. Stars show C3 rms difference from current meters at C2 and C4.	56
Fig. 6.1 : Alongshore component of surface wind stress (dynes cm^2) at NDBO 46013, computed from hourly wind measurements. The hourly stress values were low passed using a filter with a 40 hour half power point.	61
Fig. 6.2a : Primary grid of CTD stations for CODE. Stations on each line are numbered consecutively from station nearest shore. The Irish Gulch line was sampled by CTD only during 1982. The 1982 Central line was some 3 km south of the 1981 line. See Appendix for times occupied.	62
Fig. 6.2b : Secondary grid of CTD stations for CODE. Stations lie along the 50 and 100 fathom isobaths, and are numbered consecutively from northern station. See Appendix for times occupied.	63
Fig. 6.3a : Number of observations at each depth (m) and distance from shore (km). Each observation was made along one of the primary CTD lines in Fig. 6.2a following the spring transition to upwelling.	64
Fig. 6.3b : Average cross-shore and alongshore currents $u(x,z)$, $v(x,z)$ (cm/sec) over the observations of Fig. 6.3a.	65
Fig. 6.3c : Standard deviation of fluctuations in $u(x,z)$, $v(x,z)$ (cm/sec) for observations in Fig. 6.3a.	66
Fig. 6.3d : RMS expected error of the average of $u(x,z)$, $v(x,z)$ (cm/sec), assuming observations in Fig. 6.2a are independent.	67
Fig. 6.3e : Vertical shear in the mean fields $\partial \bar{u} / \partial z$, $\partial \bar{v} / \partial z$. First differences of the mean fields (Fig. 6.3b) were smoothed using a (3×3) triangular weight filter.	68
Fig. 6.3f : Cross-shore divergence $\partial \bar{u} / \partial x$ and shear $\partial \bar{v} / \partial x$ in mean currents, calculated as in Fig. 6.3e. Values enclosed in boxes are significantly different from zero at the 95% confidence level, assuming errors in the mean are given by Fig. 6.3d and that these errors are independent between adjacent bins. The latter is almost certainly optimistic.	69

Fig. 6.4a : Average $u(x,z)$, $v(x,z)$ along each CTD line. Note the jet in the average alongshore current v , the core of which intensifies and moves offshore from north to south.	70
Fig. 6.4b : Standard error of the mean for Fig. 6.4a.	71
Fig. 6.4c : Standard deviations of u , v about the means in Fig. 6.4a.	72
Fig. 6.5 : Alongshore divergence $\partial \bar{v} / \partial y$ between pairs of primary CTD lines. Values which were non-zero at the 95% confidence level as discussed in Fig. 6.3f are boxed.	73
Fig. 6.6 : Principal axes of fluctuations about the mean currents on each CTD station. Where fluctuations are nearly equal, the orientation of the principal axes is random.	74
Fig. 7.1 : DAL currents at depth of 28m, obtained during a survey from 26 April 0045 to 28 April 1400, 1981 (all times are UT), plotted over a NOAA6 IR image from 27 April 1611. Tic marks every 30 minutes of latitude and longitude (56 and 44 km respectively) and a scale vector for the currents are shown. Pt. Arena ($38^{\circ} 57' N$, $123^{\circ} 44' W$) serves as a landmark. Lighter shades correspond to colder water. For clarity of presentation all measurements within a 3 km radius have been averaged. Note the concentrated zones of flow in which cold water upwelled at the coast is carried offshore. Such flow structures may make significant contributions to the property transport budgets in the coastal zone.	83
Fig. 7.2 : Same as Fig. 7.1, except for ship survey of 2 May 1800 to 6 May 0330, 1981 and NOAA6 image from 6 May 0345. Survey was made during a period of sustained strong equatorward winds (Fig. 6.1). Compare with Davis' Fig. 5 (1984a).	84
Fig. 7.3 : Ship survey from 18 May 1600 to 22 May 0300, 1981. NOAA6 image from 20 May 1550.	85
Fig. 7.4 : Ship survey from 23 May 0100 to 25 May 0600, 1981. NOAA6 image from 20 May 1550 (same as Fig. 7.3).	86
Fig. 7.5 : Ship survey from 20 April 1600 to 22 April 1200, 1982. NOAA7 image from 24 April 2210 (note delay from survey time). This flow occurred during a cessation of winds following a period of strong southward wind forcing, and is discussed in Section 7.3.	87

Fig. 7.6 : Ship survey from 22 April 1400 to 24 April 1130, 1982. NOAA7 image from 24 April 2210 (same as Fig 7.5).	88
Fig. 7.7 : Ship survey from 9 July 0300 to 10 July 1730, 1982. NOAA7 image from 9 July 2211.	89
Fig. 7.8 : Ship survey from 11 July 1100 to 13 July 1400, 1982. NOAA7 image from 9 July 2211 (same as Fig. 7.7).	90
Fig. 7.9 : Ship survey from 14 July 1400 to 16 July 0920, 1982. NOAA7 image from 14 July 2254. Wind forcing was very strong and increasing during the survey period. Note the strong current magnitudes and shears across the northern transects.	91
Fig. 7.10 : Ship survey from 16 July 1730 to 18 July 0845, 1982. NOAA7 image from 15 July 2241. Survey was performed from south to north: winds were strong to moderate along the Central and North lines, but had calmed to airs during the surveys of the Arena and Irish Gulch lines. Northward flow at the inshore ends of the CTD lines is seen, although the flow at the offshore end of the two northern lines remains strong and strongly sheared. Note the developing eddy along the North line.	92
Fig. 7.11 : Ship survey from 19 July 1900 to 22 July 0400, 1982. NOAA7 image from 22 July 2259. Winds were calm during the survey of southern 3 lines, but were moderate to strong along the northern 3 lines. The eddy along the North line has developed strongly. Davis (1983) shows tracks of surface drifters which circulated in this eddy for a week and more, making several circuits.	93
Figs. 7.12 : Cross-shelf sections of alongshore current with depth during the wind relaxation of April 1982. Sections are from the five primary CTD lines, plus a CN line midway between the Central and North lines. Pluses show location of measurements. Contour interval is 10 cm/sec. Equatorward currents are shaded.	94
Fig. 7.13 : Alongshore current $v(x)$ at 28m for the 4 Central line occupations from 20-24 April.	95
Fig. 7.14 : Cross-shelf sections of alongshore currents with depth for the four surveys of the Central line from 20-24 April.	96

Fig. 7.15 : Time series of moored measurements showing alongshore component of wind stress τ at NDBO 46013, and temperature difference and $\partial v / \partial z$ between instruments at 5 and 10m depth at C3 vs day of 1982.	97
Fig. 7.16 : At least 4 large tongues of cold water are seen in this NOAA6 IR image of sea surface temperature between Cape Mendocino and Pt. Conception (image provided by Pierre Flament).	98
Fig. 7.17 : Currents at 28m depth from offshore survey of 4-10 July 1981, overplotted on NOAA6 IR image of sea surface temperature from 8 July.	99
Fig. 7.18 : Currents at 28m depth from offshore survey of 22-26 July 1982, overplotted on NOAA7 IR image of sea surface temperature from 22 July.	100
Fig. 7.19 : Ship track during 1982 offshore survey, indicating locations of sections through the cold water tongue. Clouds obscured the area during the actual survey time, and the location of the front and detailed structure of the temperature field were not available from satellite IR.	101
Fig. 7.20 : T-S diagram from underway thermosalinograph during jet survey (data kindly made available by Pierre Flament, Libe Washburn and Larry Armi). Sampling depth is approximately 5m.	102
Figs. 7.21 : Across-jet sections of along-jet currents through the cold tongue and adjacent waters. Also shown are the temperature, salinity and density (as σ_θ) at 5m depth from the underway thermosalinograph (data kindly made available by Pierre Flament, Libe Washburn and Larry Armi).	103
Fig. A.1 : Central Line occupations vs. day of year.	109
Fig. A.2 : Elk Line occupations vs. day of year.	110
Fig. A.3 : Irish Gulch Line occupations vs. day of year.	111
Fig. A.4 : Arena Line occupations vs. day of year.	112
Fig. A.5 : North Line occupations vs. day of year.	113

Fig. A.6 : Ross Line occupations vs. day of year.	114
Fig. A.7 : Fifty Fathom Line occupations vs. day of year.	115
Fig. A.8 : Hundred Fathom Line occupations vs. day of year.	116

Table 3.1 : Nominal DAB operating parameters

transmit frequency	f	300 kHz
wavelength	$\frac{c}{f}$	0.5 cm
repeat interval		0.63 sec
pulse length	T	20 msec
range bin	$\Delta\tau$	10 msec
beam angle	α_0	30° from vertical
beam width		2° to 3° from centerline
transducer depth	z_0	5 m

Table 3.2 Range Bin Geometry

n range bin number 1,2,...,32
 c speed of sound

range to head of pulse after time t	$c(T-t)$
range to tail of pulse after time t	ct
duration of range bin n	$(n-1)\Delta\tau$ to $n\Delta\tau$

For the n^{th} range bin		Nominal value (m)
center range	$(c/2)(\frac{T}{2} - (n - \frac{1}{2})\Delta\tau)$	$3.8 - 7.5n$
center depth	$(c/2)(\frac{T}{2} - (n - \frac{1}{2})\Delta\tau)\cos\alpha_0 - z_0$	$8.3 - 6.5n$
range extent of returns	$(c/2)(T + \Delta\tau)$	22.5
range extent continuously ensonified	$(c/2)\Delta\tau$	7.5
depth extent continuously ensonified	$(c/2)\Delta\tau\cos\alpha_0$	6.5
greatest range sampled	$(c/2)(T - (n-1)\Delta\tau)$	$7.5(n-1)$

Chapter 3

DATA PROCESSING AND ERROR ANALYSIS

Making shipboard estimates of current profiles requires knowing

- (1) $\mathbf{x}(t)$, the instrument position as a function of time, and
- (2) $\mathbf{V}(z,t)$, the relative velocity

In this section we discuss the measurements made during CODE to obtain these data, devoting special attention to identifying potential sources of error. In the next chapter, these data will be used to estimate the field of currents $\mathbf{u}(z,t;\mathbf{x}_0) \approx \mathbf{u}$. Following that, the currents inferred from the shipboard system will be compared with moored current meter measurements in Chapter 5.

3.1. Instrumentation

The data acquisition system for this study was designed and implemented by Lloyd Regier. The acoustic measurements were made from the R/V Wecoma using a prototype of the Ametek-Straza DCP4015, controlled from a Commodore PET 2001 home computer. Operating characteristics of the acoustic system are given in Table 3.1. Once every 0.63 sec, a 300 kHz acoustic pulse of 20 msec duration was transmitted. The Doppler shift in the acoustic returns was measured by the Ametek electronics for each beam in 32 range bins, each of duration $\Delta r = 10$ msec. Table 3.2 gives the nominal correspondence between range bin and physical depths. The measurements in each range bin also contained a "quality" flag to indicate whether the frequency detection loop was locked. The ship's heading (from the ship's Sperry Mk.37 master gyrocompass), ocean temperature at the transducer, and time (from the internal PET clock) were recorded for each pulse. For every 100 pulses (approximately once per minute), a LORAN-C fix was taken from a Northstar 5000 receiver. In addition, during CODE 1 (1981), gyroscopic measurements of pitch and roll were sampled 16 times per ping, with 16 msec between samples. All data were recorded without further processing onto 9 track magnetic tape.

3.2. LORAN-C

Measurements of the ship's latitude λ and longitude L from a Northstar 5000 LORAN-C receiver were recorded throughout the experiment at intervals of approximately 70 seconds. LORAN-C is the Long Range Aid to Navigation network maintained by the U. S. Coast Guard. It employs low frequency (100 kHz) radio signals to provide a hyperbolic navigation grid. Position on this grid is defined by the differences in reception time of synchronized signals transmitted from at least three well separated

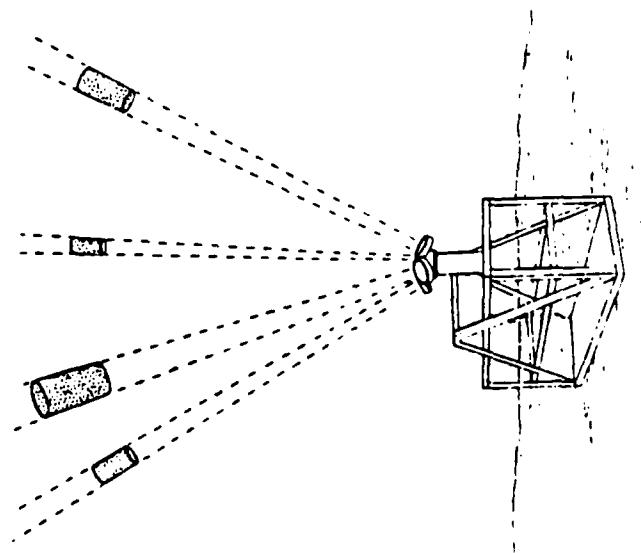


Fig. 2.3 : A Doppler current profiler which has been bottom mounted for vertical profiling of local currents.

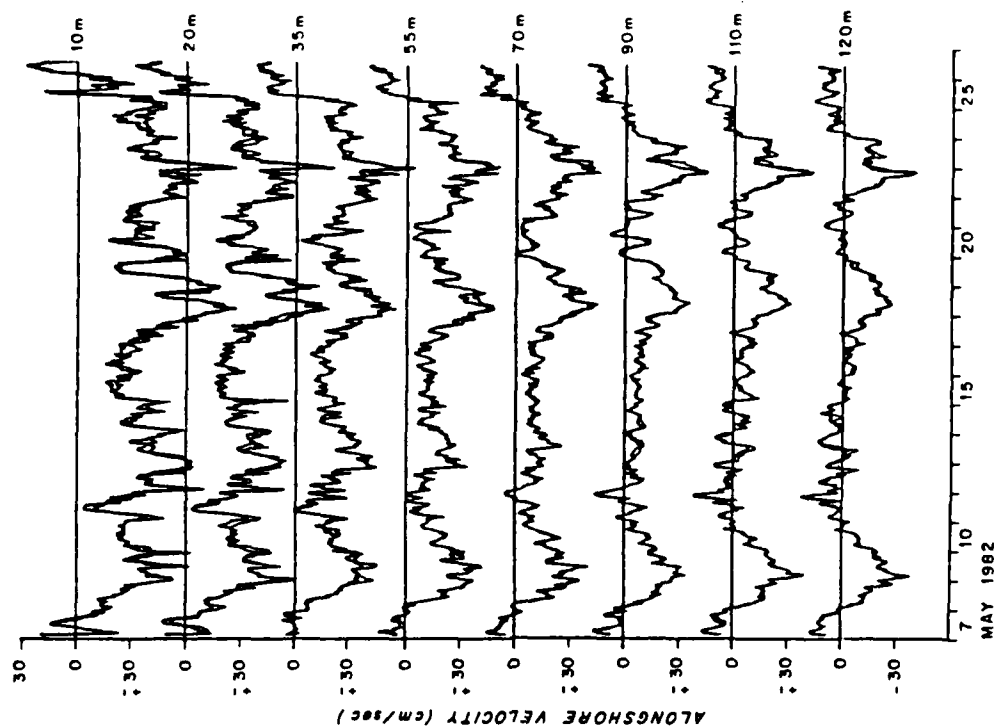


Fig. 2.4 : Bottom mounted Doppler acoustic current measurements superimposed on mechanical current meter records (Pettigrew and Irish [1983]).

Pettigrew and Irish (1983) have made current measurements with a four beam acoustic Doppler instrument similar in most respects to the one described above, the major difference being that their system is designed to make measurements from a stationary platform. The transducer is attached in an upward-looking configuration to a frame which rests on the sea floor (see Fig. 2.3). In Fig. 2.4, hourly averages of current measurements from their Doppler system are plotted along with simultaneous hourly average measurements from a string of moored current meters located approximately 300m away. The striking agreement between the time series indicates that Doppler backscatter provides reliable measurements of ocean flow velocities relative to the transducer for flow speeds up to order 30 cm sec.

Mounting the instrument on a movable platform such as a ship introduces a number of complications. In particular, to obtain ocean currents the platform rotation and translation must be removed from the measurements. This requires introducing imperfect measurements of the platform motion which add error to the final result. Another important difference is that the acoustic environment at the ship's hull is much more variable than that found at the sea floor. Furthermore, since the ship can move at speeds which are one or two orders of magnitude larger than the currents, signal-to-noise limitations can be severe.

This discussion has glossed over a number of important details. For example, Eq 2.1 is only an approximation to the Doppler shift; refractive effects from sound-speed gradients and current shears have been neglected completely, as have second order and higher terms in $\mathbf{V} \cdot \mathbf{c}$. Numerical solutions which include these effects have been explored on a case by case basis in work with Regier. In general, neglect of these factors does not cause significant errors in the determination of \mathbf{V} when a four-beam Janus system is used. The same cannot be said, however, for other beam geometries such as the three-beam Janus system. Moreover, the effects of finite beam width, side lobe levels and multiple scattering have been ignored. Rather than exhaustively catalogue the potential errors, we shall turn to examination of the measurements themselves.

$$\begin{aligned}\hat{\mathbf{r}}_1 &= \sin\alpha_0\hat{\mathbf{x}}' - \cos\alpha_0\hat{\mathbf{z}}' & \hat{\mathbf{r}}_2 &= \sin\alpha_0\hat{\mathbf{y}}' - \cos\alpha_0\hat{\mathbf{z}}' \\ \hat{\mathbf{r}}_3 &= -\sin\alpha_0\hat{\mathbf{x}}' - \cos\alpha_0\hat{\mathbf{z}}' & \hat{\mathbf{r}}_4 &= -\sin\alpha_0\hat{\mathbf{y}}' - \cos\alpha_0\hat{\mathbf{z}}'\end{aligned}\quad (2.5)$$

The spatial dependence of the relative velocity $\mathbf{V}(\mathbf{r})$ in Eq 2.2 comes entirely from shears in the current field, as may be seen from Eq 1.2. Since the currents are expected to be vertically sheared, we expand $\mathbf{V}(\mathbf{r})$ about its value directly below the ship. With

$$\begin{aligned}\mathbf{r} &= x'\hat{\mathbf{x}}' + y'\hat{\mathbf{y}}' + z'\hat{\mathbf{z}}' \\ \mathbf{V}(\mathbf{r}) &= \mathbf{V}(z') + (\mathbf{r} - z'\hat{\mathbf{z}}') \cdot \nabla \mathbf{V}(z') + \dots\end{aligned}\quad (2.6)$$

the Doppler shift (2.2) at time τ can be written for each beam as

$$\begin{aligned}\Delta f_1(\tau) &= \frac{2f_0}{c} \left[\mathbf{V}(z') + z' \tan\alpha_0 \frac{\partial \mathbf{V}(z')}{\partial x'} + \dots \right] \cdot (\sin\alpha_0\hat{\mathbf{x}}' - \cos\alpha_0\hat{\mathbf{z}}') \\ \Delta f_2(\tau) &= \frac{2f_0}{c} \left[\mathbf{V}(z') + z' \tan\alpha_0 \frac{\partial \mathbf{V}(z')}{\partial y'} + \dots \right] \cdot (\sin\alpha_0\hat{\mathbf{y}}' - \cos\alpha_0\hat{\mathbf{z}}') \\ \Delta f_3(\tau) &= \frac{2f_0}{c} \left[\mathbf{V}(z') + z' \tan\alpha_0 \frac{\partial \mathbf{V}(z')}{\partial x'} + \dots \right] \cdot (-\sin\alpha_0\hat{\mathbf{x}}' - \cos\alpha_0\hat{\mathbf{z}}') \\ \Delta f_4(\tau) &= \frac{2f_0}{c} \left[\mathbf{V}(z') + z' \tan\alpha_0 \frac{\partial \mathbf{V}(z')}{\partial y'} + \dots \right] \cdot (-\sin\alpha_0\hat{\mathbf{y}}' - \cos\alpha_0\hat{\mathbf{z}}')\end{aligned}\quad (2.7)$$

where $z'(\tau) = \frac{c}{2}(\frac{T}{2} - \tau)\cos\alpha_0$ is the quasi-vertical coordinate. If we denote the components of \mathbf{V} by (F,P,H) as in Fig. 2.2, then

$$\begin{aligned}F(z') &= \frac{c}{2f_0} \frac{\Delta f_1(\tau) - \Delta f_3(\tau)}{2\sin\alpha_0} = O\left(z' \frac{\partial H}{\partial x'}\right) + \dots \\ P(z') &= \frac{c}{2f_0} \frac{\Delta f_2(\tau) - \Delta f_4(\tau)}{2\sin\alpha_0} = O\left(z' \frac{\partial H}{\partial y'}\right) + \dots \\ H(z') &= \frac{c}{2f_0} \frac{\Delta f_1(\tau) + \Delta f_2(\tau) - \Delta f_3(\tau) - \Delta f_4(\tau)}{4\cos\alpha_0} = O\left(z' \tan^2\alpha_0 \left(\frac{\partial F}{\partial x'} + \frac{\partial P}{\partial y'}\right)\right) + \dots\end{aligned}\quad (2.8)$$

Thus, by combining the measurements from complementary beams the three components of relative velocity can be determined as a function of z' , the quasi-vertical coordinate. Turbulence and high frequency internal waves act as noise to this determination by adding short scale variability through the terms on the right hand side of Eq 2.8.

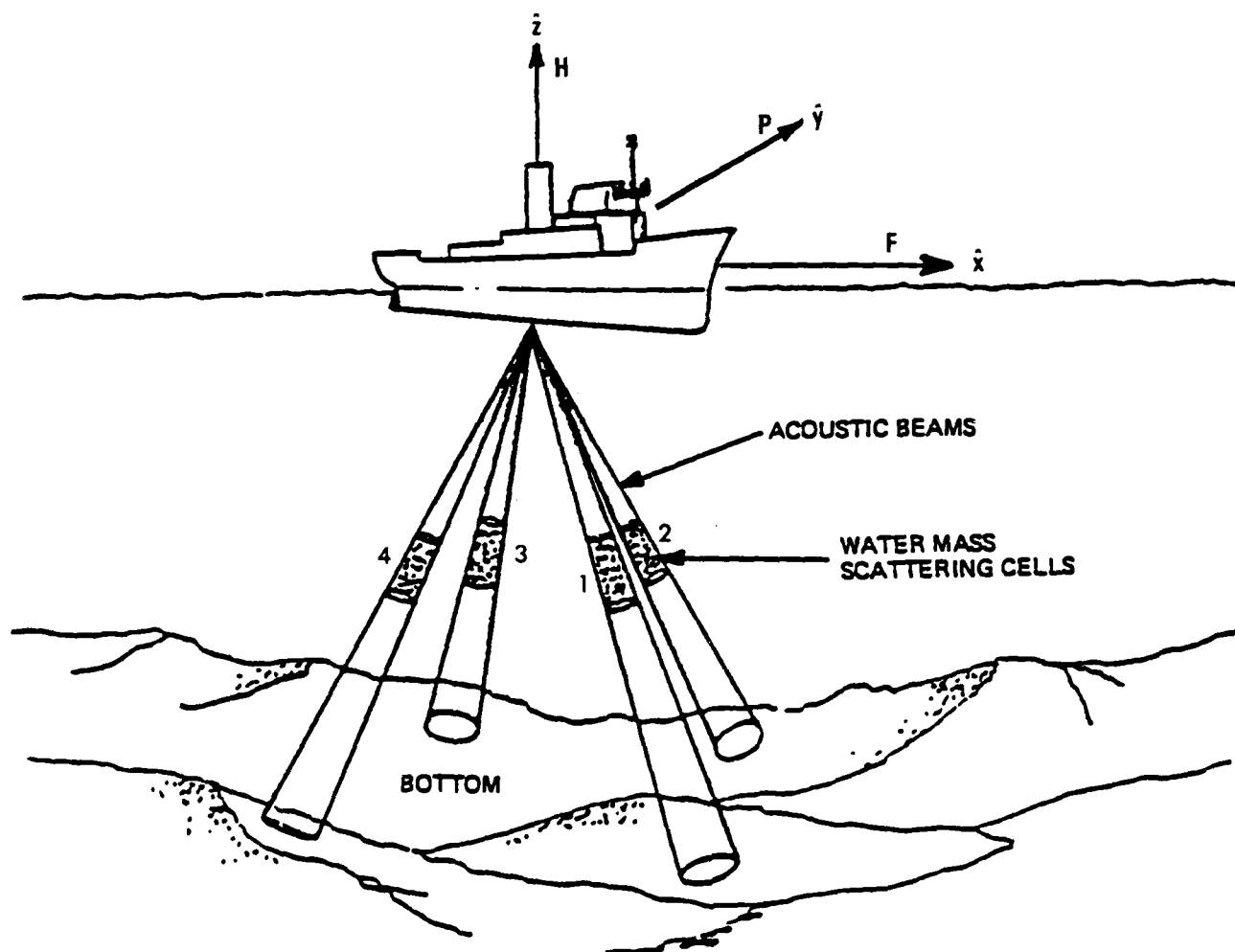


Fig 2.2 : Range Gated Shipboard Doppler System. Four beams (fore, aft, port and starboard) equally inclined from the ship's vertical axis acoustically probe the ocean. The Doppler shift in backscattered signal measures the relative velocity between ship and ocean. Range gating allows depth profiling of currents.

There is a wide variety of acoustic targets in the ocean including zooplankton, air bubbles, fish and the ocean bottom itself. Each such target can contribute energy to the backscattered signal reaching the transducer, at a Doppler shifted frequency corresponding to its own relative velocity \mathbf{V}_t . Thus, in addition to the uncertainty in frequency measurement introduced by short resolution time at each depth, the signal heard at the transducer will contain a spectrum of frequencies due to the range of target velocities. If the velocity of the targets through the water is random, then averaging over many scattering events yields a spectrum which is centered at a Doppler shifted frequency corresponding to \mathbf{V} , the relative velocity of the water.

Because the acoustic energy is transmitted as a short pulse of duration T , the returns heard at any given time τ after transmission must have scattered within the parcel of water at ranges $c\tau/2$ to $c(T+\tau)/2$ along the beam. Returns heard at longer τ were scattered from further down the beam. Thus by measuring the Doppler shift as a function of τ it is possible to profile the along-beam component of \mathbf{V} as a function of along-beam distance.

$$\Delta f_i(\tau) = \frac{2f_c}{c}(\mathbf{V}(\mathbf{r}_i) \cdot \hat{\mathbf{r}}_i) \quad (2.2a)$$

$$\mathbf{r}_i = \frac{c}{2} \left(\frac{T}{2} + \tau \right) \hat{\mathbf{r}}_i \quad (2.2b)$$

In practice, the returning signal is range gated - analyzed in discrete blocks of time $\Delta\tau$ called range bins - rather than continuously recorded. This allows a finite time to resolve the Doppler shift. Note that allowing longer $\Delta\tau$ increases the accuracy with which the spectrum can be resolved, but decreases the range resolution.

The full relative velocity vector \mathbf{V} can be determined as a function of the vertical coordinate by using several beams, provided that \mathbf{V} changes primarily along the vertical symmetry axis of the beams. This may be seen by adopting a coordinate system tied to the ship, with origin at the acoustic transducer and coordinate axes which point along the fore, port and heave directions $\hat{\mathbf{x}}'$, $\hat{\mathbf{y}}'$ and $\hat{\mathbf{z}}'$ respectively (see Fig. 2.2). In these coordinates the i^{th} beam direction is

$$\hat{\mathbf{r}}_i = \cos\psi_i \sin\alpha_i \hat{\mathbf{x}}' + \sin\psi_i \sin\alpha_i \hat{\mathbf{y}}' + \cos\alpha_i \hat{\mathbf{z}}' \quad (2.3)$$

where ψ_i is the azimuthal angle, and α_i is the elevation angle, of the i^{th} beam. For the four-beam Janus system, these angles are

$$\alpha_i = \alpha_0 \quad i = 1, 2, 3, 4 \quad (2.4)$$

$$\psi_i = (i-1) \frac{\pi}{2}$$

so that

June 28, 1932.

C CHILOWSKY

1,864,638

METHOD AND MEANS FOR THE OBSERVATION AND MEASUREMENT OF THE
SPEED OF A VESSEL BY DIRECTED BEAMS OF ULTRA-AUDIBLE WAVES

Filed Dec. 13, 1924

3 Sheets-Sheet 1

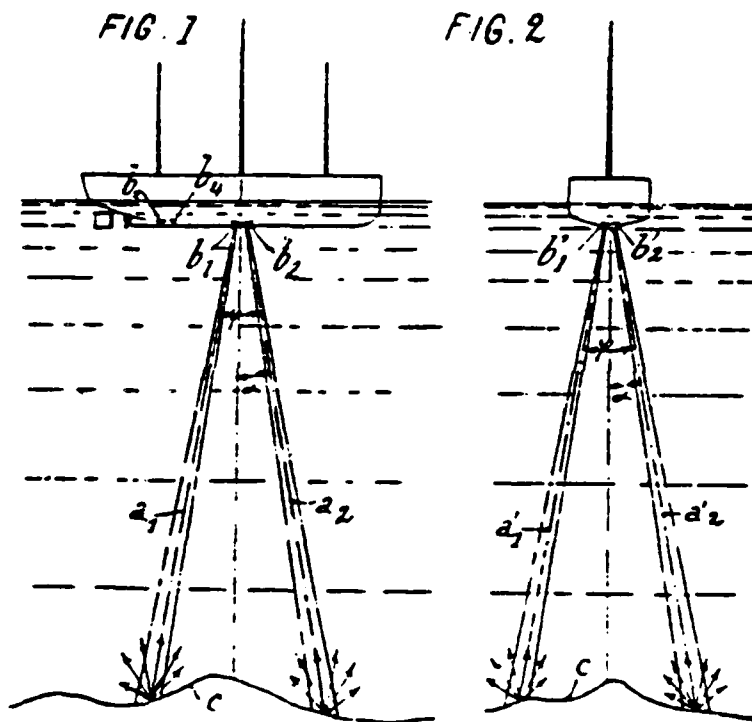


Fig. 2.1 : The use of acoustic Doppler shift to measure the velocity of ships at sea dates back to this patent by C. Chilowski, submitted in 1924. Note the sophisticated 4 beam Janus design which is still used for first order pitch and roll compensation.

Chapter 2

DOPPLER ACOUSTIC LOG

For this study $V(z)$, the relative velocity of the water as a function of depth, was determined acoustically using a commercially available instrument system (Rowe and Young, 1979) which we shall call the Doppler Acoustic Log, or simply DAL. The remote measurement of velocity using a Doppler shift has a long history; applications are found in fields ranging from astrophysics to law enforcement. Meteorologists for some time have used the technique to remotely measure winds from ground based radar systems (Lhermitte, 1973). Since 1972, R. Pinkel of SIO has applied it to make oceanographic measurements from the quasi-stationary research platform FLIP. Most recently Regier (1982), Joyce *et al.* (1982), and Joyce and Stalcup (1984) have used the technique to make shipboard current measurements.

It was realized as early as 1924 that the Doppler shift could be exploited to make a "speed log" for ships. By measuring acoustic backscatter from the ocean bottom or from the water column itself and determining the Doppler shift between transmitted and received signals, the velocity of the ship relative to the scattering medium can be inferred in a manner to be outlined below. The original design concept for such a log, shown in Fig. 2.1 (Chilowski, 1932), already employs the sophisticated four-beam Janus configuration still in use today.

In the modern instrument used for this study, an acoustic transducer mounted to the ship's hull simultaneously transmits a short pulse of acoustic energy (ping) of well defined frequency f_0 along four beams, each inclined 30° from the ship's vertical axis, pointing forward, aft, port and starboard. As each pulse travels down its beam, it "ensonifies" successive volumes of ocean along that beam (Fig. 2.2). Acoustic targets within the ensonified volume may scatter a portion of the incident energy, and a portion of this scattered energy will be directed back toward the transducer. The motion of those targets relative to the transducer will induce a Doppler shift $\Delta f = f_R - f_0$ in the frequency f_R of the backscattered energy received at the transducer. If the relative velocity between target and transducer is V_i and the speed of sound is c , then, to first order in V_i/c

$$\Delta f = \frac{2f_i}{c} (V_i \cdot \hat{r}_i) \quad (2.1)$$

where \hat{r}_i a unit vector along the i^{th} beam. To this order of approximation, the Doppler shift is therefore a measure of that component of the target velocity V_i which lies along the acoustic beam direction.

Since the measurements for this study come from instrumentation which is somewhat novel, we first address some questions regarding the accuracy of the technique. The importance of such questions may be readily appreciated, since the currents are inferred as a difference between two directly measured quantities dx_0/dt and V , each of which may be much larger than the current. For example, to measure currents to an accuracy of 1 cm/sec from a ship travelling at 10 knots (approximately 500 cm/sec), both dx_0/dt and V must be measured to an accuracy of 0.2%. After a brief introduction to the shipboard Doppler system in Chapter 2, the Doppler and collateral measurements are examined, questions of accuracy are explored, and considerations required in transforming the shipboard referenced measurements into an Earth-fixed reference frame are discussed in Chapter 3. In Chapter 4 Doppler measurements are combined with navigation data to extract the currents. Chapter 5 presents a comparison of measured currents from the shipboard Doppler system with those made from moored current meters. With this background we then look at the ocean measurements collected during the CODE experiment in Chapters 6 and 7, where the quasi-synoptic field is mapped and the spatial variability in the mean field and several interesting event scale features are described. We find that the synoptic view of ocean currents shows an astonishingly rich field of energetic eddies and jets which actively transport upwelled coastal water offshore. These features of the synoptic current field occur over a wide range of scales. The mean field, on the other hand, resembles the rather smooth earlier findings shown in Fig. 1.1.

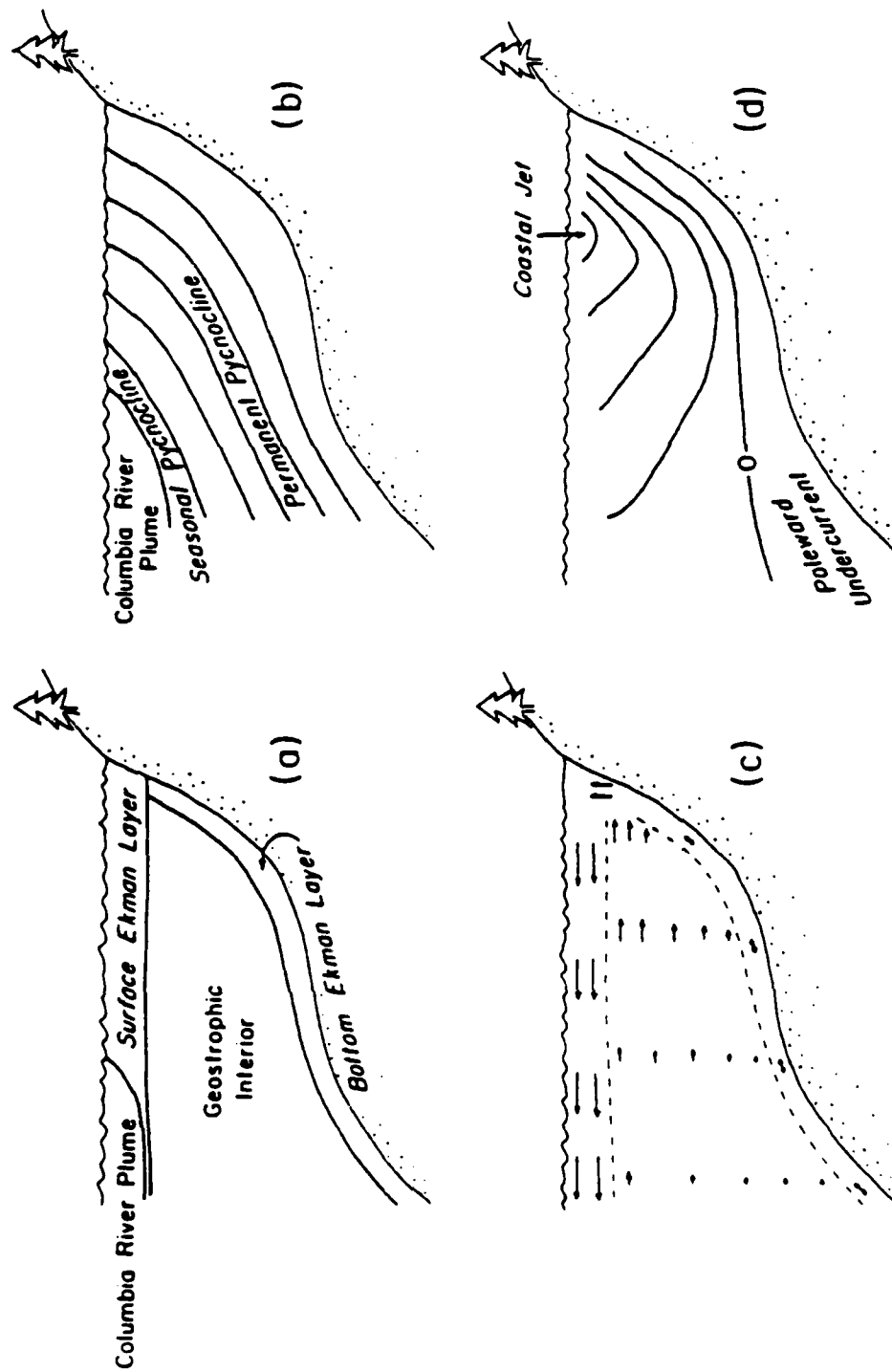


Fig. 1.1 : Schematic view of coastal upwelling circulation (from Huyer 1983).

instrument can sample different locations becomes the new, less restrictive, constraint on the set of (x,y,z,t) points which can be studied.

Over the past two decades, moored current meters have been used to intensively study the current field in coastal upwelling regions. Fig. 1.1 shows a schematic picture of the upwelling circulation which has been derived from such measurements off Oregon (Huyer, 1983). Equatorward wind forcing causes offshore transport of warm surface water in a surface Ekman boundary layer. To replace it, cold dense water at depth flows toward the coast. This cold water surfaces in a band near the coast. The alongshore currents are described by a surface intensified equatorward jet, whose vertical shear is geostrophically balanced by cross-shore density gradients induced by the upwelling. Flowing counter to the direction of wind forcing, a poleward undercurrent is seen at depth. Models of this circulation usually assume that gradients in velocity are small enough that advective terms can be neglected in the momentum balance, and that alongshore variations of the currents are much smaller than cross-shore variations (Allen, 1980).

When spatial variability can be determined synoptically, this simple picture derived from moored instruments gives way to a much more complex one. Satellite images of sea surface temperature show cold upwelled water, rather than occurring in a simple band along the coast, forms very complex patterns with strong alongshore variability. Upwelling centers, patches of coastline with intense upwelling, have been observed in many locations (see Brink, 1983). Tongues of cold water extending several hundred kilometers out to sea have been recognized along the west coast of the U.S. (Bernstein, *et al.* 1972, Breaker and Gilliland 1981, Traganza, *et al.* 1981, Kelly 1983). Because these features are hard to study with moored instruments, little is directly known about the strength or structure of the circulation which forms them. If the features are associated with strong currents, they may represent important pathways of exchange between coastal and offshore waters.

During the Coastal Ocean Dynamics Experiment (CODE), a broad range of techniques were applied to the measurement of ocean variability in the coastal and offshore waters of Northern California during the spring and summer upwelling seasons of 1981 and 1982 (CODE Group 1983). In addition to extensive moored instrumentation, a major effort was made to resolve the spatial structure of the upwelling fields through the use of satellite infra-red (IR) imaging for sea surface temperature, aircraft mapping of sea surface temperature and meteorological data, a large program of drifter measurements, as well as shipboard DAL current profiling. This study reports the results of the DAL program.

Chapter 1

INTRODUCTION

The shipboard Doppler Acoustic Log (DAL) to be discussed in this study is a new tool for the measurement of ocean currents. By providing vertical profiles of currents over the upper 150m of ocean at points along the ship's path, it allows the ocean to be sampled in a way which is fundamentally different from moored current meters or drifters, the instruments most commonly used for current measurement. This instrument is used to examine the circulation in a region of strong coastal upwelling off Northern California, where it reveals an unexpectedly energetic and spatially complex synoptic flow field.

Consider the general problem of measuring the current at the water parcel whose coordinates are $\mathbf{x}_w(t)$ using an instrument whose location is $\mathbf{x}_0(t)$, explicitly a function of time. By a simple identity

$$\frac{d\mathbf{x}_w}{dt} = \frac{d\mathbf{x}_0}{dt} + \frac{d(\mathbf{x}_w - \mathbf{x}_0)}{dt} \quad (1.1)$$

In the notation which will be used throughout this study, Eq (1.1) may be rewritten as

$$\mathbf{u}(\mathbf{x}_0 - \mathbf{r}) = \frac{d\mathbf{x}_0}{dt} + \mathbf{V}(\mathbf{r}) \quad (1.2)$$

where

$$\mathbf{r} \equiv \mathbf{x}_w - \mathbf{x}_0$$

$$\mathbf{u}(\mathbf{x}_0 - \mathbf{r}) \equiv d\mathbf{x}_w/dt$$

$$\mathbf{V}(\mathbf{r}) \equiv d(\mathbf{x}_w - \mathbf{x}_0)/dt$$

The current \mathbf{u} at the measurement point $\mathbf{x}_0 - \mathbf{r}$ must be determined from the sum of two terms. One, the relative velocity $\mathbf{V}(\mathbf{r})$, is the velocity of the water parcel relative to the instrument position. The other, $d\mathbf{x}_0/dt$, is the velocity of the instrument itself with respect to the Earth. Moored instruments and drifters each measure only one of these terms, and are engineered to make the unmeasured term, $d\mathbf{x}_0/dt$ for moored instruments and \mathbf{V} for drifters, negligible. This design constraint places limits upon the types of variability which each instrument can sample. Although ocean currents vary in all three spatial dimensions as well as in time, a moored instrument samples only the temporal variability at a single location, while a drifter samples the time and space variability only along the path of a single water parcel. For an instrument such as the DAL, which directly measures both \mathbf{V} and $d\mathbf{x}_0/dt$, these constraints on possible sampling trajectories are removed, allowing mapping of the current field. The speed with which the

List of Tables

Table 3.1 : Nominal DAL operating parameters	13
Table 3.2 : Range bin geometry	13
Table 3.3 : Gyroscopic measurements of the ship's attitude were used to correct the shipboard profiles of relative velocity $V(z)$ for the effects of pitch and roll during CODE 1. This table shows the errors (in cm sec) which would have been incurred in 100 ping averages of $V(z)$ in the absence of such corrections. Less than 1 cm sec of bias is introduced into the horizontal components of $V(z)$ when pitch and roll compensation is not performed. The added noise in the estimates is likewise small. These calculations were performed on data subsets described in section 3.6 of the text.	26
Table 3.4 : Heading Errors. This table lists several common errors which may be present in gyrocompass data. Magnitudes assume an operating latitude of 38° N, a course due north at 10 knots, and a maneuver in which the ship reverses course over a time which is short compared with the Schuler period. With the exception of the rolling error, these may be corrected either at the gyrocompass or in post-processing.	28
Table 3.5 : Calibration error β and misalignment angle $\delta\theta_0$ calculated from changes in apparent current which accompany changes in ship velocity using Eq 3.12. The large value of $\delta\theta_0$ during CODE 1, Leg 4 decreases substantially for subsequent cruises; this drop coincides with repair and realignment work performed on the gyrocompass following Leg 4.	32
Table 5.1 : CODE 2 moored array. S (SS) denotes a current meter string which is surface (sub-surface) moored. VACM (VMCM) denotes a Vector Averaging (Measuring) Current Meter.	48
Table 5.2 : Current meter DAL comparison statistics. Whenever the DAL was within 1 km of a mooring, comparison of DAL and moored current meter measurements was made. Averages and variances for each instrument are shown, as are covariance, correlation and standard deviation of the difference between measurements from each instrument. Also shown is a comparison between the only closely spaced pair of moored instruments in CODE, a VACM and a VMCM both at 10m near C3.	50

locations. The receiver's internal software converts position from the LORAN grid to λ and L . The system's advantages lie in its wide coverage and continuous availability.

LORAN-C fixes are subject to a number of first order errors, including dual solutions and cycle errors (lane jumps). Dual solutions arise when only two time delay measurements (three transmitters) are available. Since the line of positions which yield a given time delay is a hyperbola, and hyperbolae form closed curves on a sphere, two lines of position will intersect at two distinct points in general, and the intersection corresponding to the receiver location must be selected. The solutions are often well separated, in which case selection of the proper one is easy. Cycle errors are discrete offsets in the time delay measurement by multiples of $10 \mu\text{sec}$. They occur most commonly when the signal is weak, and are caused by the misidentification of the arrival time of the pulse, defined by the third rising zero crossing of the 100 kHz carrier within the pulse. If the wrong zero crossing is tracked, the time delay measurement slips by an integral number of carrier periods. Such a jump usually results in a position displacement of several miles, and so is easily detected. Since the LORAN-C time delays were recorded along with the Northstar λ and L , cycle errors were corrected when they occurred by correcting the time delay and recalculating the associated position change using the algorithm of Campbell (1968). This procedure was also used to correct for times when the secondary solution was erroneously recorded.

More subtle errors also may be present in LORAN-C position data. For example, the time a pulse takes to reach the receiver depends not only on the path length but also on radio wave propagation speed, which in turn depends on conductivity along the path. Day/night (Dean 1978) and land/sea path (Johler *et al.* 1956) differences may thus be important. Another concern is that the data are internally filtered by a proprietary, and thus unknown, scheme before being output by the receiver. Any lag produced in position during accelerations could seriously affect the usefulness of the data for determining ocean currents.

The most direct measure of accuracy for LORAN-C fixes comes from the variability in fixes taken at a single location. Such data were obtained over an eight hour period while the ship was docked at Yerba Buena Island between cruises. (An interruption of ships power aborted the data collection much earlier than planned.) The rms noise during this test was 13 m in latitude and 27 m in longitude. The principal axis of variability was along 249°T ; the major and minor axis rms errors were 29 m and 8 m respectively. No significant serial correlation was found between successive position errors over the sample of 62 fixes, spaced 8.5 minutes apart.

These accuracy estimates are likely to be optimistic for our purposes, since they do not include contributions from receiver motion and probably undersample long term variability. The question of position lag during ship accelerations due to internal filtering was examined by computing lagged correlations between the ship velocity as measured by the acoustic system and ship velocity inferred from LORAN-C fixes. Any filter-induced lag would show up as an asymmetry between positive and negative lagged correlations. No such asymmetry was found for lags separated by the sampling period of 70 sec. Therefore, for our analysis we shall assume that the LORAN yields position measurements which contain errors of order 10 to 30m and that these errors can be modelled as white noise, i.e. uncorrelated in time.

3.3. Thermistor

A manufacturer supplied thermistor provided ocean temperature data at the acoustic transducer. This data was used in the estimation of sound speed at the transducer. Clay and Medwin (1977) write for the speed of sound (m sec)

$$c = 1449.2 + 4.6T + 0.055T^2 + .00029T^3 - (1.34 + 0.010T)(S - 35) + .016z$$

where T , S and z are the temperature in $^{\circ}\text{C}$, salinity in ppt, and depth in m. Thus a rise in temperature of 1°C increases the sound speed 0.3%; an increase in salinity of 1 ppt results in a 0.1% increase in c . From the range of variability seen in surface temperature and salinity maps in the CODE region (e.g. Fleischbein, Gilbert and Huyer, 1982) corrections to the sound speed due to surface salinity changes are at or below the 0.1% level, hence negligible, while the corrections due to temperature variability can be 1% or more, hence essential. Snell's law implies that vertical variability in c , while larger than horizontal variability, does not affect the right hand side of (2.1) for the horizontal components of \mathbf{V} which are of interest.

The thermistor data also provides an underway map of near surface temperatures concurrent with the acoustic data. The data quality was estimated by comparing the measurements with CTD temperature profiles for Leg 4 of CODE 1. Only stations for which the upper water column was well mixed were used in making the comparison. The thermistor temperatures showed a mean error of 0.4°C . The rms variations about this mean difference decrease with time on station, implying that the thermistor is insulated by the acoustic transducer head. The time history of some of the larger differences indicates an exponential decay time for equilibration of order 20-30 minutes.

3.4. Data Valid Flag/ Depth of Acoustic Measurements

To exclude grossly erroneous data, acoustic velocity estimates at any depth were rejected unless all 4 beams showed the "data valid" flag set at that depth. This flag, set by the Ametek hardware, is an indication that the backscattered energy received at the transducer was sufficient to resolve the Doppler shifted peak of the spectrum.

Fig. 3.1 shows how the average data quality over a 12 hour period, as indicated by this flag, varied as a function of depth for 2 subsets of the data taken in water at least 500 m deep. The details between closely spaced vertical profiles can vary, but in general there is first a region near the surface for which the data quality is poor, next a broad region where data quality is excellent, and finally a region in which the data quality diminishes with depth.

Since the intensity of scattered energy falls rapidly with distance from the scatterer, it is not surprising that data quality diminishes with depth. It is conjectured that the near surface region of low validity is associated with spectral spreading caused by scattering from bubbles or directly from the ship's hull. A remarkable example of how scattering strength can vary in unforeseen ways is reported by Cochran and Sameoto (1983).

3.5. Bottom Reflection

Since CODE was a coastal experiment, acoustic data was often collected in waters for which the bottom depth was less than the acoustic range. In such regions, it was necessary to exclude signals reflected from the seafloor. The profile of received power may provide a straightforward means of accomplishing this, but such measurements proved unreliable during the experiment. Screening was thus performed on each average profile based on the bottom depth estimated from the ship's position.

In the CODE region, an efficient computer routine was developed for interpolating a digitized bathymetry, using LORAN-C fixes for position. The accuracy of the predictions, by comparison with depth sounder (PTR) measurements, was markedly improved by adjusting measured LORAN-C positions 0.3' north and 0.25' east. This is consistent with a comparison of satellite vs. LORAN-C derived positions. After adjustment of LORAN-C positions, the rms accuracy of the depth predictions within the DAL depth range was 2.5 m, or less than 1 range bin. Outside the CODE area, minimum depth sounder readings over a time interval, generally 5 minutes, were read manually and keypunched for interpolation. In the absence of depth sounder records, LORAN-C positions corrected by local estimates of the LORAN-C offset from satellite fixes were plotted on depth charts and depths keypunched for interpolation.

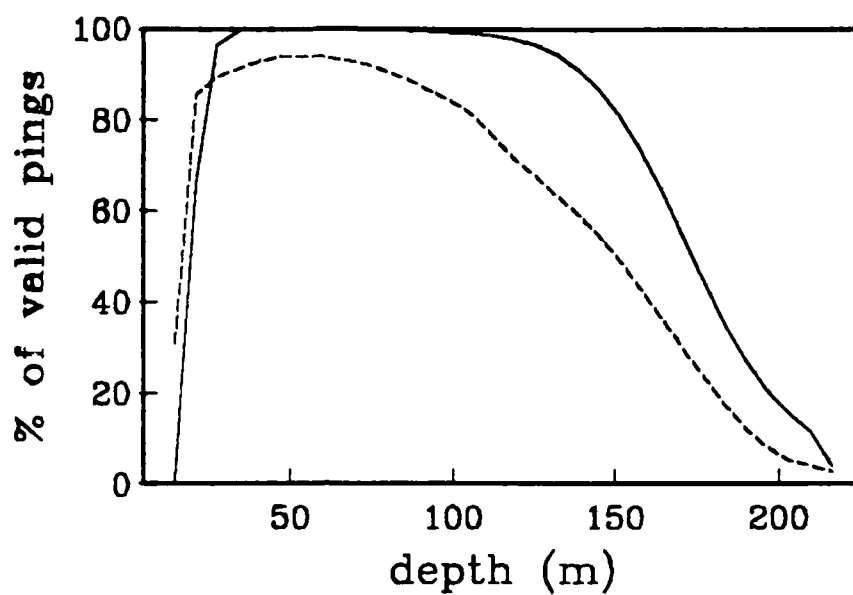


Fig 3.1 : Depth range of shipboard measurements is shown by the percent of pings for which the profiler electronics indicated valid returns at each range bin. Two 12 hour subsets of data are shown, one each from 1981 and 1982. Details of such validity profiles vary with many factors including location and time of day.

Since bottom reflection is expected to be much stronger than ocean backscatter, reflections from transducer sidelobes will degrade the signal. To reject all possible sidelobe reflections from the bottom, the profile was regarded as valid only for range bins whose maximum range is less than the water depth, D , minus the transducer depth, z_0 . From Table 3.2, relating range bin geometry and depth, the relative velocity profile was regarded as valid at depth z only if

$$z < D \cos \alpha_0 - \left[\frac{c(T - \Delta\tau)}{4} \cos \alpha_0 + (\cos \alpha_0 - 1)z_0 \right]$$

or for the nominal values of the parameters

$$z < 0.87D - 9 \text{ meters.}$$

Because of the need to eliminate bottom reflection, near bottom currents cannot be profiled.

3.6. Acoustic Profiles of Relative Velocity in Ships Coordinates

How accurate are acoustic measurements of relative velocity \mathbf{V} made from a moving ship? They will contain errors from a wide variety of sources, and we may expect large variability between individual profiles. Variability arises from measurement noise due to finite bandwidth in the transmitted acoustic pulse, as well as finite time for frequency resolution within a range bin. Variability occurs in the ocean at scales below our resolution, from small scale turbulence within a range bin or horizontal shears at scales smaller than the separation between acoustic beams. Even if the scales of ocean velocity were fully resolved, additional variability is introduced by limited sampling of non-passive motion (swimming) of the objects scattering acoustic energy and by multiple scattering events. Accelerations of the ship, in response to ocean waves or under intentional control from the bridge, also add variability to the relative velocity.

Fig. 3.2 shows histograms of the variability in measurements of $F(z')$ and $P(z')$, the forward and portward components of \mathbf{V} , at constant z' , the depth in ships coordinates (Chap 2). The data come from 1-minute segments (100 pings) over which the ship speed was being held steady. Despite the fact that the data are taken over a short time interval, the rms variability in individual estimates \hat{F} and \hat{P} at fixed z' were

rms variability	on station	at 10 knots
in \hat{F}	38.9 cm/sec	36.3 cm/sec
in \hat{P}	23.0 cm/sec	17.3 cm/sec

The size of this variability is nearly independent of the range bin considered.

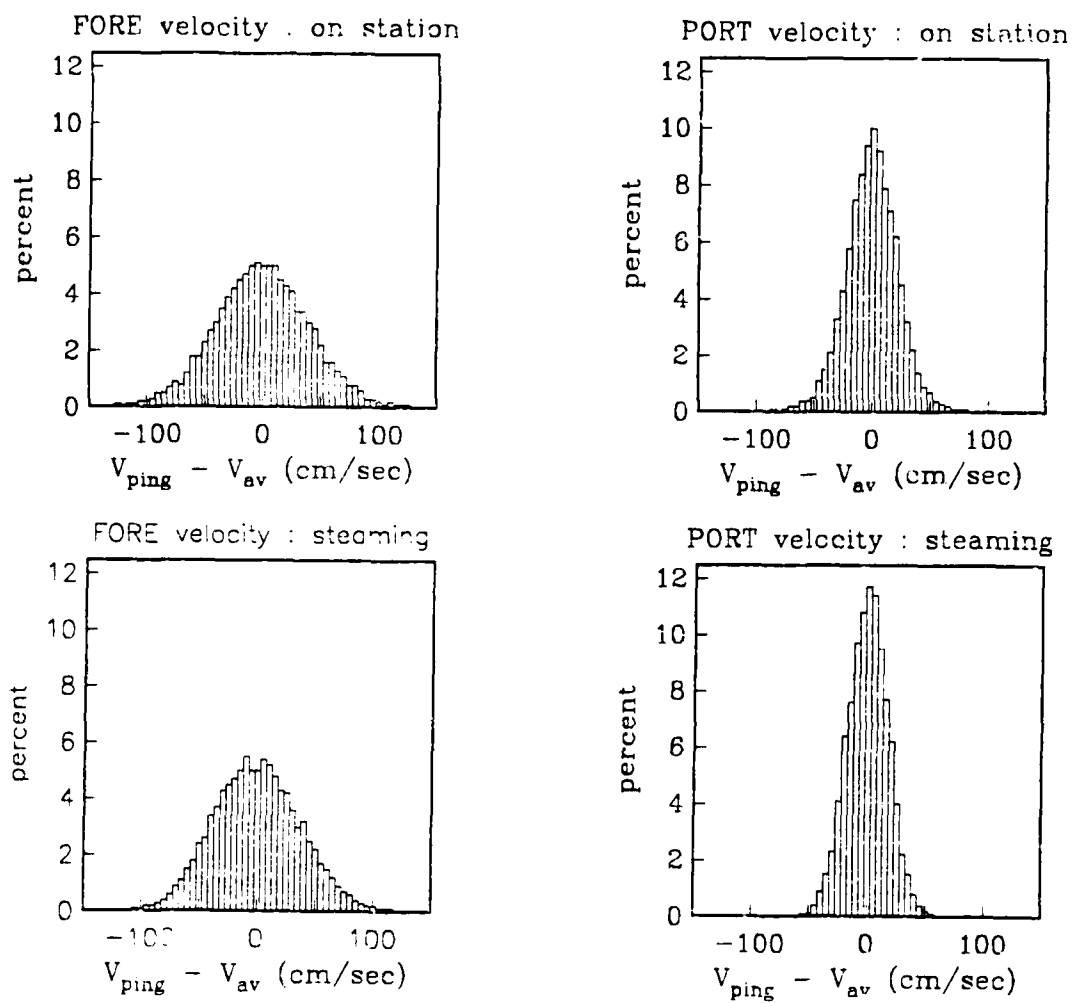


Fig 3.2 : Variability in acoustic measurements of relative velocity, shown as histograms of the deviations of single ping measurements from 100 ping average.

Autospectra of this high frequency variability are shown in Fig. 3.3 for 3 sets of conditions. In each case the ship is steaming at "constant" speed under control from the bridge. The spectra show that the variability in acoustic estimates over periods up to 1 minute is composed of a white noise background plus a broad spectral peak at periods of order 3 to 10 seconds. The frequency of the spectral peak is higher when the ship steams into the waves and lower when steaming away from waves. These characteristics suggest that the peak is due to accelerations of the ship by the surface wave field. This is confirmed by the high coherence found in the 3 to 10 second bands of the cross spectrum of $\hat{F}(z')$ and $\hat{P}(z')$ with the pitch and roll angle of the ship (Fig. 3.4). The contributions to the rms variability from measurement of wave-induced ship accelerations and from the white noise background error level are

rms variability	on station	at 10 knots
in \hat{F} total	38.9 cm sec	36.3 cm sec
wave	37.6 cm sec	34.1 cm sec
white	9.8 cm sec	12.5 cm sec
in \hat{P} total	23.0 cm sec	17.3 cm sec
wave	20.7 cm sec	13.6 cm sec
white	10.0 cm sec	10.7 cm sec

Clearly the majority of variability at periods up to 1 minute arises from sensing of actual wave induced ship motions rather than from white noise inaccuracies in the measurement process itself.

Nonetheless, before they can be used to infer properties of the ocean, the measurements must be filtered to reduce both the white noise and wave induced variability. The success that any proposed filter will have in reducing this variance can be calculated from the spectrum of the noise (Fig. 3.3) and the transfer function of the filter. Fig. 3.5 shows the rms noise as a function of filter length N for a block averaging filter. The variance is reduced rapidly with increasing N up to $N \sim 50$, then more slowly for higher N . This is because the variability due to accelerations in the wave field is highly coherent in time and is reduced approximately as N^{-1} . The white noise component, while smaller, decreases only as $N^{-1/2}$ and so persists longer.

We see then that by regarding the individual estimates \hat{F} and \hat{P} as time series at each range bin and averaging over many pings, the high frequency variability due to waves and white noise inaccuracies can be reduced. Block averaging over $N \sim 100$ samples leads to averaged estimates contaminated by 1-2 cm sec rms noise from the residual effects of white noise measurement errors and wave induced ship motion. As N is increased further, the noise from these sources decreases as $N^{-1/2}$.

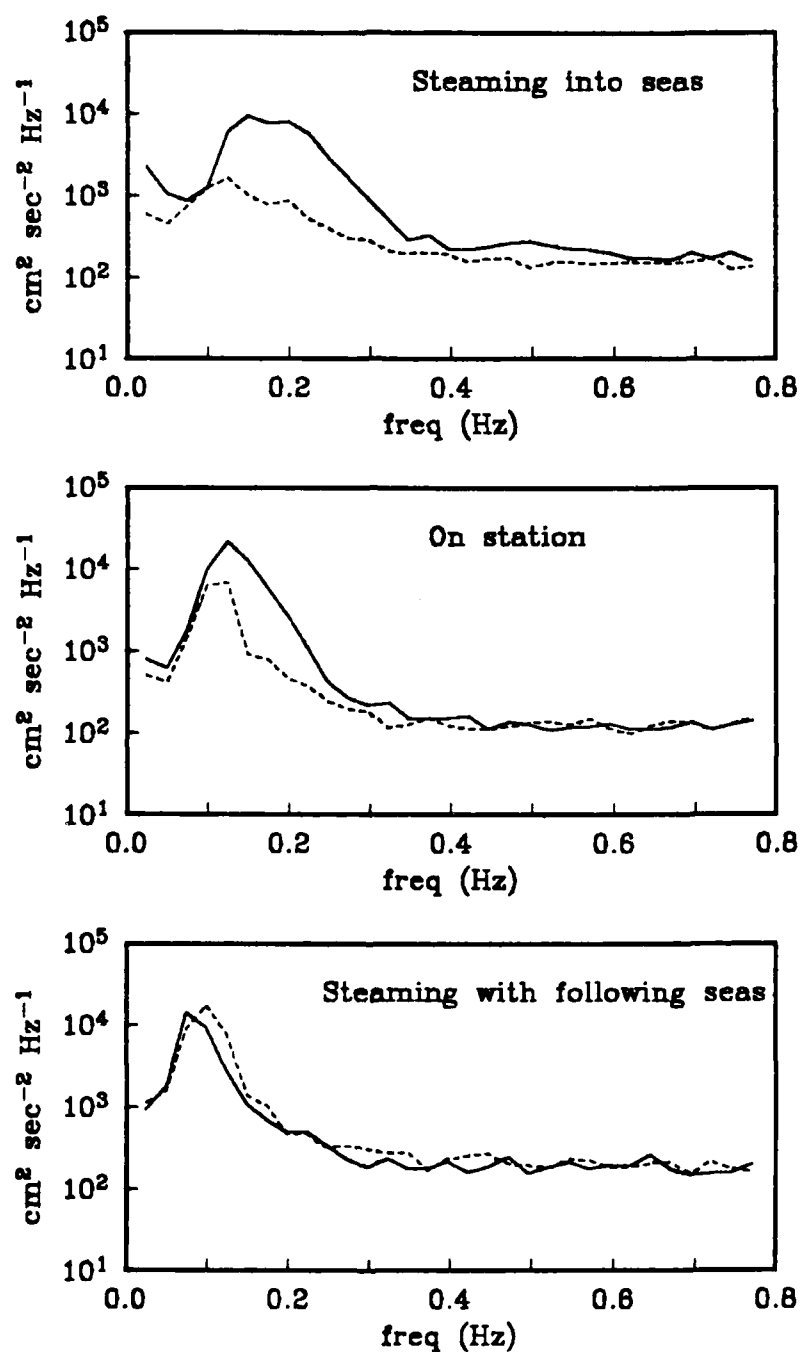


Fig 3.3 : Autospectra of ping-to-ping relative velocity measurements for 3 subsets of data taken at nearly constant shipspeed while (a) steaming into seas, (b) on station, and (c) steaming with following seas. Solid line is forward velocity F, dashed line is portward velocity P. Note peak at surface wave encounter frequency rising above a white noise background.

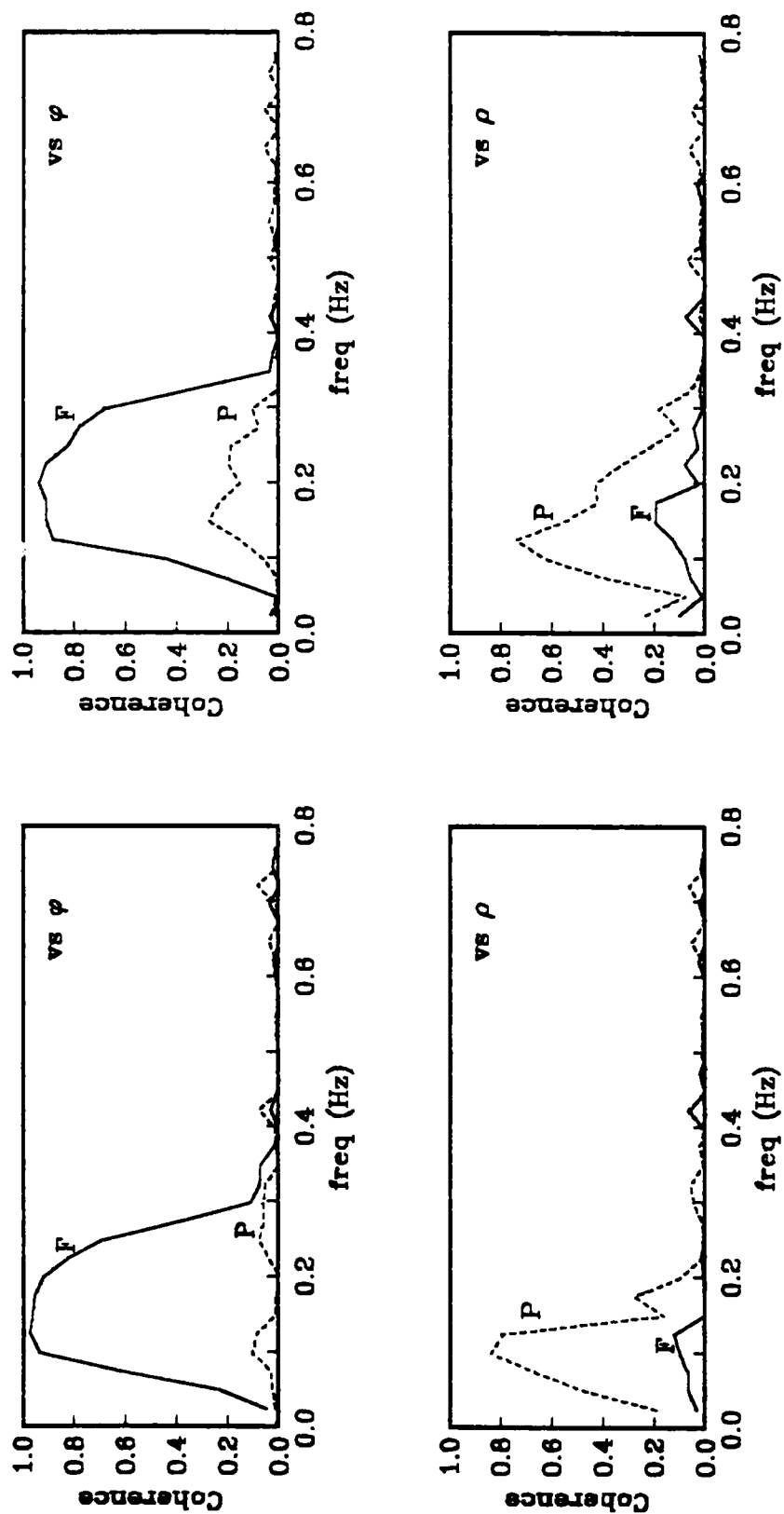


Fig 3.4 : Coherence of F (solid) and P (dashed) with pitch ϕ and roll ρ of the ship. Data in left panels taken while on station (same as middle panel, Fig 3.3); data in right panels taken while steaming into seas (same as upper panel, Fig 3.3)

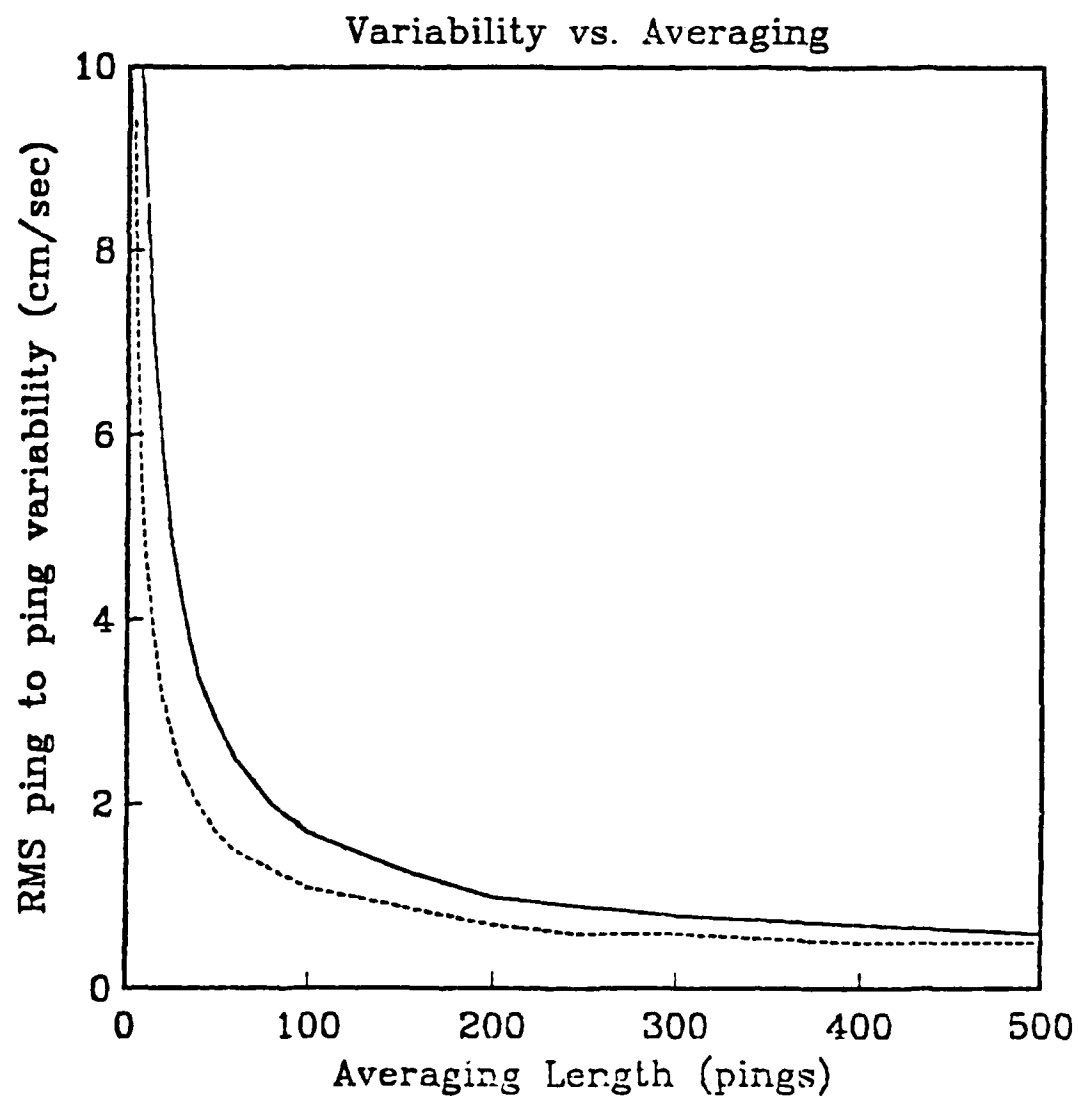


Fig. 3.5 : Expected residual wave induced and white noise in acoustic measurements of relative velocity after block averaging, as a function of averaging length.

3.7. Rotation to Geographical Coordinates

To properly vector average the relative velocity measurements, they must first be transformed from the ship's coordinate system (\hat{x} , \hat{y} , \hat{z}) to geographical coordinates. Let us define a (quasi) geographical coordinate system with origin at the ship's transducer and coordinate axes \hat{x} , \hat{y} and \hat{z} pointing east, north and up respectively. We shall describe the transformation between geographical and ships coordinates by a series of three rotations involving the angles

θ , the ship's heading, measured from \hat{y} (North) to \hat{x} (Fore)

ρ , the roll angle, positive for port side elevated

ϕ , the pitch angle, positive for bow elevated
measured relative to rolled coordinates

Any arbitrary vector whose representation in ship coordinates is \mathbf{A}' will have a representation in geographic coordinates given by

$$\mathbf{A} = \mathbf{R}_\rho \mathbf{R}_\phi \mathbf{R}_\theta \mathbf{A}' \quad (3.1)$$

$$\mathbf{R}_\theta = \begin{bmatrix} \sin\theta & \cos\theta & 0 \\ \cos\theta & \sin\theta & 0 \\ 0 & 0 & 1 \end{bmatrix} \quad \mathbf{R}_\rho = \begin{bmatrix} 1 & 0 & 0 \\ 0 & \cos\rho & -\sin\rho \\ 0 & \sin\rho & \cos\rho \end{bmatrix} \quad (3.2)$$

$$\mathbf{R}_\phi = \begin{bmatrix} \cos\phi & 0 & -\sin\phi \\ 0 & 1 & 0 \\ \sin\phi & 0 & \cos\phi \end{bmatrix}$$

Thus if the relative velocity vector measured in ship coordinates is \mathbf{V}' , the time averaged relative velocity in geographic coordinates will be

$$\mathbf{V} = \mathbf{R}_\rho \mathbf{R}_\phi \mathbf{R}_\theta \mathbf{V}' \quad (3.3)$$

Eq (3.3) emphasizes the fact that, because the transformation between the two systems is time dependent, we must transform the data to geographic coordinates before vector averaging to obtain correct averages. Otherwise, correlations between the ships orientation and its velocity will bias the resulting average and, in turn, the currents calculated from those averages. Since the transformation is performed using measured values of θ , ρ and ϕ , the errors in measuring these angles will affect inferred average velocities. The analysis of the next two sections suggests that the effects of pitch and roll are not

important for the CODE data set, but that errors in ship's heading measurements might be.

3.7.1. Pitch and Roll

Accounting for the effect of pitch and roll of the ship on measured profiles of the relative velocity vector requires consideration of two effects. In the first place, the components of \mathbf{V} must be rotated to level coordinates. In addition, the location of the measurements, z , must also be transformed. Thus

$$\begin{aligned} \mathbf{V}(z) &= \mathbf{R}_r \mathbf{R}_p \mathbf{R}_\phi \left[\mathbf{V}(z) \right] \\ &= \mathbf{R}_r \mathbf{R}_p \mathbf{R}_\phi \left[\mathbf{V}(z) + \delta \mathbf{V} \right] \\ &= \mathbf{R}_r \left[\mathbf{V}(z) + \mathbf{E} \right] \end{aligned} \quad (3.4)$$

where

$$\delta \mathbf{V} = z(1 - \cos \rho \cos \phi) \begin{bmatrix} dF/dz \\ dP/dz \\ dH/dz \end{bmatrix} - z \begin{bmatrix} \cos \rho \sin \phi dH/dz \\ \sin \rho dH/dz \\ \tan^2 \alpha_0 (\cos \rho \sin \phi dF/dz - \sin \rho dP/dz) \end{bmatrix} \quad (3.5)$$

is the term which must be added to the profile in ship's coordinates to correct for displacement of the measurement depths from their nominal positions. It is calculated from the beam equations 2.7 and 2.8 under the assumption that horizontal shears are negligible compared to vertical shears. The full error vector \mathbf{E} is the velocity overestimate if the profile is not corrected for pitch and roll.

$$\mathbf{E} = (\mathbf{I} - \mathbf{R}_r \mathbf{R}_p) \mathbf{V}(z) + \mathbf{R}_r \mathbf{R}_p \delta \mathbf{V}$$

$$\begin{bmatrix} F(1 - \cos \phi) + H \sin \phi \\ P(1 - \cos \rho) + F \sin \rho \cos \phi + H \sin \rho \cos \phi \\ H(1 - \cos \phi \cos \rho) - F \sin \phi \cos \rho + P \sin \rho \end{bmatrix} = \mathbf{R}_r \mathbf{R}_p \delta \mathbf{V} \quad (3.6)$$

Unless pitch and roll compensation is performed separately for each profile, variability in \mathbf{E} will contribute noise to estimates of $\mathbf{V}(z)$ as the ship's attitude changes from profile to profile. More importantly, if \mathbf{E} has a non-zero mean value over the averaging period used, this mean value will bias the estimate of $\mathbf{V}(z)$.

Table 3.3 : Effect of Pitch ϕ and Roll ρ angles
on Relative Velocity Components (cm. sec)

Depth = 30 m								
	Steaming				On Station			
	mean	std dev	max	min	mean	std dev	max	min
Measurements								
F	506.8	11.2	525.2	480.1	19.8	31.8	92.5	-28.7
P	2.4	5.1	11.8	-11.8	1.1	19.0	41.1	-37.0
H	-1.6	1.6	3.1	-5.9	19.2	2.1	26.6	15.3
Depth change error								
δF	.0	.0	.0	.0	.0	.0	.0	.0
δP	.0	.0	.0	.0	.0	.1	.0	.0
δH	.0	.0	.0	.0	.0	.0	.0	.0
Rectification Error								
Fore								
$F(1 - \cos \phi)$.1	.0	.3	.1	.0	.0	.0	.0
$H \sin \phi$.7	.2	1.4	.3	.6	.2	1.0	.2
Port								
$P(1 - \cos \rho)$.0	.0	.0	.0	.0	.0	.2	-.1
$F \sin \phi \sin \rho$	-.1	.0	.0	-.2	.0	.0	.0	.0
$H \cos \phi \sin \rho$	-.1	.1	.2	-.4	.0	.3	1.0	-1.2
Heave								
$H(1 - \cos \phi \cos \rho)$.0	.0	.0	.0	.0	.0	.1	.0
$-F \sin \phi \cos \rho$	4.1	1.2	7.1	.5	-.2	.3	.2	-1.4
$-P \sin \rho$.1	.1	.3	.0	.6	.6	3.0	.0
NET ERROR (cm. sec)								
in F	.8	.2	1.6	.4	.6	.2	1.0	.2
in P	-.1	.1	.2	-.5	.0	.3	1.0	-1.1
in H	4.2	1.2	7.2	.6	.4	.7	3.1	-.9

Table 3.3 : Gyroscopic measurements of the ship's attitude were used to correct the ship-board profiles of relative velocity $V(z)$ for the effects of pitch and roll during CODE 1. This table shows the errors (in cm. sec) which would have been incurred in 100 ping averages of $V(z)$ in the absence of such corrections. Less than 1 cm. sec of bias is introduced into the horizontal components of $V(z)$ when pitch and roll compensation is not performed. The added noise in the estimates is likewise small. These calculations were performed on data subsets described in section 3.6 of the text.

During CODE 1 the pitch and roll of the ship were measured gyroscopically during all acoustic profiling as described in Section 3.1. These data were used to calculate the terms in \mathbf{E} which are introduced when pitch and roll corrections to the profile of relative velocity are neglected. Results are presented in Table 3.3 for two data subsets during which the ship's heading θ was held constant, one while the ship was steaming, the other while the ship maintained position. Each data subset consisted of 60 blocks of 100 pings each (approximately 1 hour) and correspond to the data whose cross-spectra were presented in Fig. 3.4. The results indicate that, while the long term average of ship vertical velocity shows a substantial bias of order 3-4 cm/sec when pitch and roll compensation is not performed, the long term bias in the horizontal velocities is less than 1 cm/sec. Table 3.3 indicates that the major contribution to the bias in the fore component arises from rectification of the heave component through the term $\bar{H}\sin\phi$, while the major contribution to the bias in vertical velocity comes from the $\bar{F}\sin\phi\bar{\omega}\cos\rho$ term. The effect of range bin displacement on long term averages was in general very small. The rms size of the additional noise in a 100 ping average profile due to variability in \mathbf{E} is of order 0.2 cm/sec, which is small compared with the 1 to 2 cm/sec noise from high frequency variability which remains after filtering, as discussed in the previous section.

These results indicate that, for a well-riding vessel such as the R/V Weconia, averages of acoustic profiles can be calculated with minimal error in horizontal velocity estimates by treating the data as though they were measured in a level plane, ignoring corrections for pitch and roll.

3.7.2. Heading

The third reference angle which must be determined before the relative velocity profile can be rotated to geographic coordinates is the ship's heading. Surprisingly, it is measurement of this angle, not pitch and roll, which introduces the largest uncertainty into the data required for determination of currents. This comes about because a small measurement error in θ , the heading angle between North and the Fore direction, can lead to large errors in the inferred geographic components of relative velocity, and therefore to large spurious currents. If the measured heading is $\hat{\theta} = \theta + \delta\theta$, where $\delta\theta$ is the measurement error, then the geographic components of relative velocity computed using Eq (3.2) will be in error by

$$\begin{aligned}\hat{U}(z) &= U(z) - U(z)(\cos\delta\theta - 1) + V(z)\sin\delta\theta \\ \hat{V}(z) &= V(z) - U(z)\sin\delta\theta + V(z)(\cos\delta\theta - 1)\end{aligned}$$

For a ship steaming north at $V = 500$ cm/sec (~ 10 knots), a heading error $\delta\theta$ of 1° would yield errors of (8.7, -0.1) cm/sec in the relative velocities (\hat{U}, \hat{V}), and so add erroneous contributions of the same size to the currents. Since the error is dominated by

and seek the values of \hat{u} , \hat{d} which produce the minimum total squared misfit between the data and the model

$$\epsilon^2 = \sum_{j=1}^N (\hat{d}_j - \hat{u} t_j - \hat{d}_0)^2. \quad (4.31)$$

Note that $\hat{d} = 0$ must be treated as a measurement. This is because the best fit will not, in general, pass through $d_0 = 0$ since all fixes, including \hat{x}_0 , contain measurement error. Minimizing ϵ^2 with respect to \hat{u} and \hat{d} gives

$$\hat{u} = \frac{(N+1) \sum_{j=1}^N \hat{d}_j t_j - \sum_{j=1}^N t_j \sum_{j=1}^N \hat{d}_j}{(N+1) \sum_{j=1}^N t_j^2 - (\sum_{j=1}^N t_j)^2} \quad (4.32)$$

$$\hat{d} = \frac{\sum_{j=1}^N \hat{d}_j \sum_{j=1}^N t_j^2 - \sum_{j=1}^N \hat{d}_j t_j \sum_{j=1}^N t_j}{(N+1) \sum_{j=1}^N t_j^2 - (\sum_{j=1}^N t_j)^2} \quad (4.33)$$

This least squares fitting procedure can be viewed equally well as a filtering procedure. This may be seen by rewriting (4.32) in the form

$$\hat{u} = \sum_{j=1}^N \omega_j \hat{d}_j \quad (4.34)$$

where

$$\omega_j = \frac{(N+1)t_j - \sum_{k=1}^N t_k}{(N+1) \sum_{k=1}^N t_k^2 - (\sum_{k=1}^N t_k)^2} \quad (4.35)$$

The ω_j do not depend on the data values \hat{d}_j and may be viewed as filter weights. If the sampling occurs at equal intervals

$$t_j = j\Delta t \quad (4.36)$$

then

$$\omega_j = \frac{6}{\Delta t} \left(\frac{2j - N}{N(N+1)(N+2)} \right) \quad (4.37)$$

Substituting (4.37) and (4.29) into (4.34) we find

Note that the filter is symmetric, $w_{i-1} = w_{i+1}$. This means that we need not have required the current to be constant over the filtering interval. The weaker condition

$$\frac{1}{2}(u_{i-1} + u_{i+1}) = u_i \quad (4.25)$$

suffices for (4.16) *et seq.* to apply.

This optimum filter is a significant improvement over simple averaging, since the rms measurement noise in the estimated current decreases as $M^{-3/2}$, compared with the rate M^{-1} obtained for simple averaging. The simple average has a clear meaning - rather than calculating the current between sequential fixes, average \hat{V}_i over $(2M-1)$ fix intervals and use only the endpoints $\hat{x}_{i-M+1}, \hat{x}_{i+M}$ to determine the current. The optimum estimate also has a simple physical interpretation. As we show below, it is identical to making a least squares fit to the slope with time of the displacement of a water parcel at the measurement depth.

4.5. Least Squares Drift

During a single measurement interval Δt_i a water parcel at the measurement depth will drift due to the currents by an amount

$$u_i \Delta t_i = (x_i - x_{i-1}) - V_i \Delta t_i = \xi_i. \quad (4.26)$$

We initially assume, as before, that the current is constant over the water parcels sampled during the estimation interval. Then the total drift from time t_0 to time t_j

$$d_j - d_0 = \sum_{i=1}^j \xi_i = x_j - x_0 - \sum_{i=1}^j V_i \Delta t_i \quad (4.27)$$

will increase linearly in time with a slope given by the current. Thus the current can be estimated by using measurements $\{\hat{x}_i\}, \{\hat{V}_i\}$ to calculate the cumulative drifts and then finding the line which best fits them. As we shall see, additional useful information can be obtained by adopting this point of view.

Let

$$\hat{\xi}_i = x_i - x_{i-1} - \hat{V}_i \Delta t_i \quad (4.28)$$

be the measured drift between the $i-1^{\text{st}}$ and i^{th} fixes. Accumulate this in a total drift from the start of the estimation to the j^{th} fix in

$$d_j - d_0 = \sum_{i=1}^j \hat{\xi}_i \quad (4.29)$$

We may define without loss of generality t_0 , the initial time, and \hat{d}_0 , the measured drift at t_0 , to be 0. Since the true current is assumed constant, we model the true drift as

$$d = ut + d_0 \quad (4.30)$$

$$\hat{u} = \sum_{j=1}^M w_j \hat{u}_{j,n} = u_0 \left(\sum_{j=1}^M w_j - 1 \right) \quad (4.16)$$

Assuming that the efforts of Chapter 3 were successful and the bias of the measurements $\hat{u}_{j,n} = 0$, the bias in the filtered estimate is

$$\hat{u} = u_0 \left(\sum_{j=1}^M w_j - 1 \right). \quad (4.17)$$

Zero bias is obtained if the weights $\{w_j\}$ satisfy

$$\sum_{j=1}^M w_j = 1. \quad (4.18)$$

With (4.16) and (4.18), the mean square error is

$$\hat{u}_j^2 = \sum_{j=1}^M \sum_{k=1}^M w_j w_k \delta \hat{u}_{j,n} \delta \hat{u}_{k,n} \quad (4.19)$$

The filter weights are determined by minimizing this mean square error, subject to the constraint (4.18) which can be enforced with the aid of a Lagrange multiplier λ . Letting

$$I = \hat{u}_j^2 + \lambda \left(\sum_{j=1}^M w_j - 1 \right) \quad (4.20)$$

and requiring $\partial I / \partial w_k = 0$ for $k = 1, \dots, M$ yields the $2M-1$ equations

$$\sum_{j=1}^M w_j \delta \hat{u}_{j,n} \delta \hat{u}_{k,n} = -\lambda \quad (4.21)$$

With the constraint (4.18), these equations define at most one solution for the $2M-2$ variables $\{w_j\}$ and λ . Substituting the covariance from (4.12) into (4.21) and solving subject to the constraint (4.18) yields

$$w_j = \frac{3}{(M+1)(2M+1)(2M+3)} \left[(M+1)^2 - j^2 \right]; \quad M+1 \geq j \geq M \quad (4.22)$$

and

$$\lambda = \frac{6}{(M+1)(2M+1)(2M+3)} \left(\frac{\sigma_s}{\Delta t} \right)^2 \quad (4.23)$$

which is also the mean square error of the estimator

$$\hat{u}_j^2 = \lambda \approx \frac{6}{N(N+1)(N+2)} \left(\frac{\sigma_s}{\Delta t} \right)^2 \quad (4.24)$$

as may be verified from (4.19).

The rms noise in \hat{u} , an individual estimate of the current, is then

$$\sigma_{\hat{u}} = \delta \hat{u}^2 = 12 \frac{\sqrt{2}\sigma_v}{\Delta t} \sqrt{1 + \frac{1}{2} \left(\frac{\sigma_v \Delta t}{\sigma_u} \right)^2}$$

$$\approx \frac{\sqrt{2}\sigma_v}{\Delta t}$$

This noise is quite large: for $\Delta t = 70$ sec σ is 8.7 cm/sec and 40 cm/sec for the cross-shore and alongshore currents respectively.

Since this noise is proportional to $1/\Delta t$, an obvious method for improving the accuracy would be to use longer time intervals between fixes. Increasing Δt to $N\Delta t$ results in an N -fold decrease in the rms error $\sigma_{\hat{u}}$. But simply increasing the time between fixes is equivalent to averaging N adjacent u measured over the shorter interval Δt , as may be seen from (4.3). When measurements are available on the shorter time interval Δt , simple averaging thus corresponds to throwing away the information provided by intermediate fixes, and using only the initial and final fixes. On the other hand, by taking the statistics of the signal and errors into account we can improve the filtering beyond the simple averaging of an endpoint estimator.

4.4. Optimum Estimator

The insight gained from spectral analysis of the raw measurements can be used to produce an estimator \hat{u} for the current u which optimally reduces the noise due to errors in the measurements u_i . It is natural to construct this estimate from a linear combination of the $N = 2M + 1$ closest measurements centered at \hat{u}_i ,

$$\hat{u} = \sum_{-M}^M w_i u_i \quad (4.14)$$

The filter weights $\{w_i\}$ are to be determined by minimizing the expected mean square error in \hat{u} for a fixed filter length $N = 2M + 1$. The error in the estimate (4.14) will be

$$\delta \hat{u} = \sum_{-M}^M w_i \delta u_i - \left[\sum_{-M}^M w_i u_i - u_i \right] \quad (4.15)$$

The first term in (4.15) is the error due to noise δu_i in the measurements, while the term in brackets is the error which would arise simply from filtering the field, even in the absence of measurement noise. Clearly it is not possible to choose a single set of weights which minimizes this latter term for arbitrary structure in the true field u_i . Since the analysis of the preceding section suggested that the geophysical signal is contained in the low frequency portion of the spectrum, we tentatively assume that u is constant over the filtering interval (we shall relax this condition later). Then

To test this interpretation of the spectral peaks, we consider a simple model for the signal and noise statistics. The error spectrum is determined by the correlation function of the errors

$$S_{\hat{u}\hat{u}}(f) = 2 \frac{\Delta t}{2M-1} \sum_{n=1}^M \sum_{m=1}^M \delta \hat{u}_n \delta \hat{u}_m e^{-2\pi i(f - m/M)\Delta t} \quad (4.10)$$

Eq (4.6) relates $\delta \hat{u}$ to the errors in the measured quantities, $\delta \hat{X}_x$, $\delta \hat{V}_x$. The discussion in Chapter 3 suggests that it is plausible to model

$$\begin{aligned} \delta \hat{X}_x \delta \hat{X}_x &= \sigma_x^2 \epsilon_{n,n} \\ \delta \hat{V}_x \delta \hat{V}_x &= \sigma_v^2 \epsilon_{n,n} \\ \delta \hat{X}_x \delta \hat{V}_x &= 0 \end{aligned} \quad (4.11)$$

If this model is valid, then the noise in the current measurements

$$\delta u_n \delta \hat{u}_m = \frac{\sigma_x^2}{\Delta t^2} \left(2 - \left(\frac{\sigma_v \Delta t}{\sigma_x} \right)^2 \right) \epsilon_{n,m} + \epsilon_{n-1,m} - \epsilon_{n+1,m} \quad (4.12)$$

so that we should observe a measured spectrum,

$$S_{\hat{u}\hat{u}}(f) = S_{uu} + \frac{8\sigma_x^2}{\Delta t} \sin^2 \pi f \Delta t + 2\sigma_v^2 \Delta t \quad (4.13)$$

Representative values of $\sigma_x \approx 30$ m, $\sigma_v \approx 2$ cm/sec and $\Delta t \approx 70$ sec are cited from the results of Chapter 3. Errors in the position are the dominant source of noise over most of the spectrum, i.e. for $f = \frac{1}{\pi \Delta t} \sin^{-1} \left(\frac{\sigma_v \Delta t}{2\sigma_x} \right) \approx 1 \cdot 10^{-4}$ Hz. We therefore expect that, if the model statistics are correct, the spectrum should be proportional to $\sin^2 \pi f \Delta t$ over the noise dominated frequencies.

In Fig. 4.3 we plot $S_{\hat{u}\hat{u}}(f) \sin^2 \pi f \Delta t$. The constancy of this quantity for $f = 1 \cdot 2 \cdot 10^{-2}$ Hz supports both the identification of the high frequency peak as the noise portion of the spectrum, and also verifies the statistical model (4.11) over this most energetic part of the inferred noise. Below 10^{-3} Hz, \hat{u} contains either signal from the current field or non-white noise. In the absence of other information, we adopt the former possibility as a working hypothesis.

4.3. Endpoint Estimator

Application of (4.13) to the data in Fig. 4.3 allows an estimate of the rms noise in position measurements

$$\begin{aligned} \sigma_x &= 43 \text{ m in the cross-shore direction} \\ &= 20 \text{ m in the alongshore direction} \end{aligned}$$

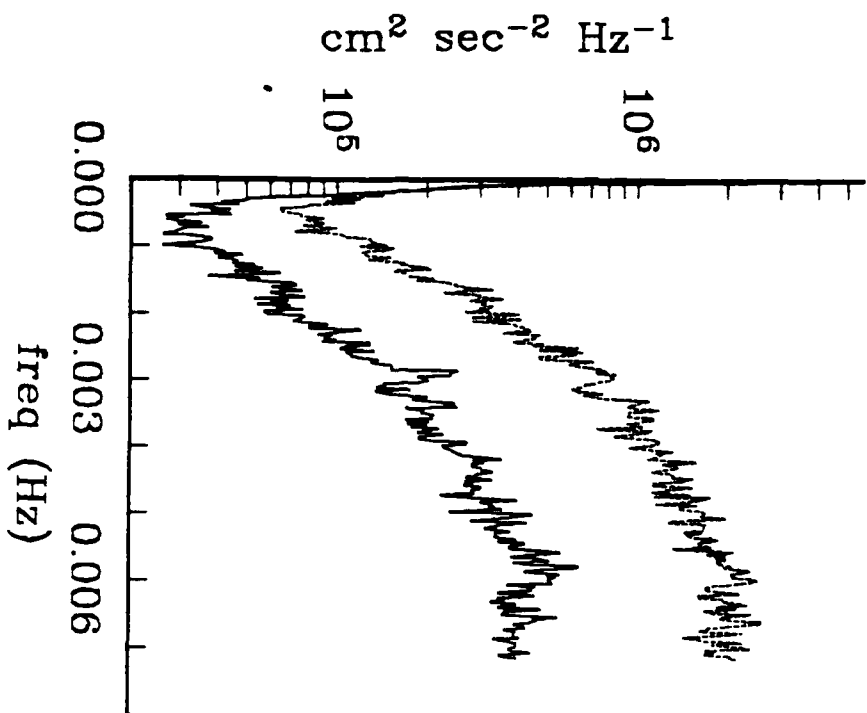


Fig 4.2 : Spectrum of fix-to-fix current measurements for v (solid line, alongshore current, $317^\circ T$) and u (dashed line, cross-shore current, $47^\circ T$).

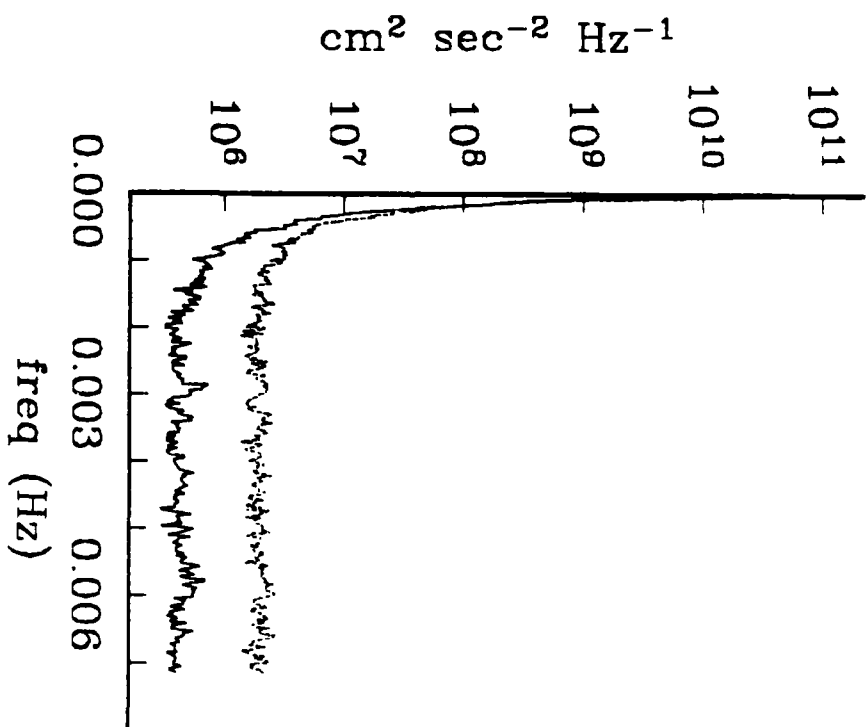


Fig 4.3 : Same as Fig 4.2 except normalized by $\sin^2 \pi (\Delta t)$. White noise in LORAN fixes yields a flat spectrum for fix-to-fix currents under this normalization.

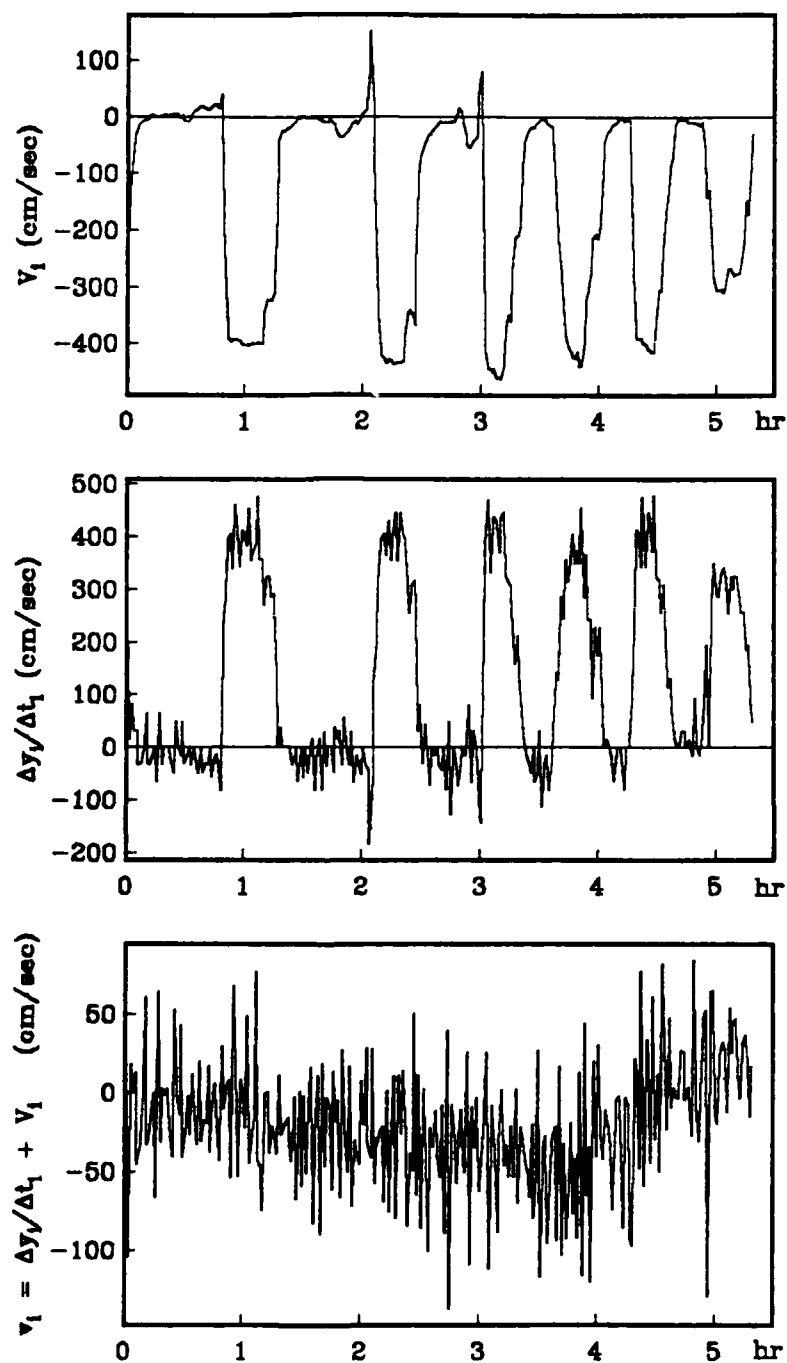


Fig. 4.1 : Sample time series of measurements. Top panel shows the acoustically determined relative velocity \bar{V} , middle panel shows $d\bar{x}_0/dt$ from LORAN-C. Bottom panel shows the sum of these, the fix-to-fix current measurement \bar{u} .

$$\hat{u}_i = u_i + \delta u_i \quad (4.4)$$

where

$$u_i = \frac{1}{\Delta t} \int_{t_{i-1}}^{t_i} u(\mathbf{x}_i - \mathbf{z}_k \mathbf{z}) dt \quad (4.5)$$

and

$$\delta \hat{u} = \frac{1}{\Delta t} (\delta \hat{x}_i - \delta \hat{x}_{i-1}) = \delta \hat{V}_i. \quad (4.6)$$

Fig. 4.1 shows representative time series of the measured quantities \hat{V}_i , $\Delta \hat{x}_i / \Delta t_i$, and \hat{u}_i .

4.2. Spectrum of the Measurements

The fix-to-fix current measurements $\{\hat{u}_i\}$ are a time series, whose spectrum $S_{\hat{u}\hat{u}}(f)$ may be evaluated via a discrete Fourier transform. If the fixes are equally spaced so that $\Delta t_i = \Delta t$ for all i ,

$$S_{\hat{u}\hat{u}}(f) = \frac{2}{(2M-1)\Delta t} \Delta t \sum_{m=-M}^M \hat{u}_m e^{-2\pi m f \Delta t} \quad (4.7)$$

Then from (4.4), assuming signal and noise are uncorrelated,

$$S_{\hat{u}\hat{u}}(f) = S_{uu}(f) + S_{\delta \hat{u}\delta \hat{u}}(f) \quad (4.9)$$

i.e., the spectrum of the measurements is the sum of the noise and true field variability spectra.

Figure 4.2 shows the spectrum $S_{\hat{u}\hat{u}}(f)$ of the fix-to-fix current measurements \hat{u}_i for a subset of the data described in Section 3.6. The solid curve is for measurements of the current component along 317°T , the alongshore direction in CODE; the dashed curve is for cross-shore currents. The variance in the measurements, given by the area under the spectrum, is larger for the cross-shore currents than for the alongshore currents. Both components show similar spectral shapes, characterized by a sharp peak at low frequencies, a broad rise at higher frequencies, and a spectral gap in between. It is tempting to identify the low frequency peak as the geophysical signal $S_{uu}(f)$ and the broad high frequency peak as the contribution of the noise spectrum $S_{\delta \hat{u}\delta \hat{u}}(f)$. The spectral gap between these two would be encouraging, indicating that the energetic part of the noise could be filtered with minimum loss of the geophysical signal.

ESTIMATION OF CURRENTS

4.1. Introduction

We now address the problem of obtaining the best estimate of the current field using the data described in Chapter 3. In Chapter 1 we wrote

$$\mathbf{u}(\mathbf{x}_0 + \mathbf{r}) = \frac{d\mathbf{x}_0}{dt} + \mathbf{V}(\mathbf{r}) \quad (4.1)$$

where \mathbf{x}_0 is the location of the instrument, \mathbf{r} is the location of the measurement relative to the instrument, and \mathbf{u} , $d\mathbf{x}_0/dt$ and \mathbf{V} are the current, instrument velocity and relative velocity respectively. Our data set consists of measurements of consecutive fixes \mathbf{x}_0 and of the average vertical profile of relative velocity $\mathbf{V}(z)$ between fixes.

First consider the problem using measurements from a single depth, with each velocity component treated separately. Using tildes to identify measured quantities and hats to identify estimates, we define

$$t_i = \text{the time of the } i^{\text{th}} \text{ position fix} \quad (4.2a)$$

$$\Delta t_i = t_i - t_{i-1} \quad (4.2b)$$

$$\mathbf{x}_i = \mathbf{x}_0(t_i), \text{ the true position at time } t_i \quad (4.2c)$$

$$\hat{\mathbf{x}}_i = \mathbf{x}_i + \delta \hat{\mathbf{x}}_i, \text{ the measured position at time } t_i \quad (4.2d)$$

$$\mathbf{V}_i = \frac{1}{\Delta t_i} \int_{t_{i-1}}^{t_i} \mathbf{V}(z_k) dt, \text{ the true average } \mathbf{V} \text{ between fixes} \quad (4.2e)$$

$$\hat{\mathbf{V}}_i = \frac{1}{\Delta t_i} \int_{t_{i-1}}^{t_i} \hat{\mathbf{V}}(z_k) dt = \mathbf{V}_i + \delta \hat{\mathbf{V}}_i, \text{ the measured average } \mathbf{V} \text{ between fixes} \quad (4.2f)$$

where z_k is the depth of the k^{th} range bin and $\delta \hat{\mathbf{x}}_i$, $\delta \hat{\mathbf{V}}_i$ are the errors in the measurements.

Each pair of fixes, together with the average relative velocity between them, constitutes a measurement of the average current at z_k

$$\hat{\mathbf{u}}_i = \frac{1}{\Delta t_i} (\hat{\mathbf{x}}_i - \hat{\mathbf{x}}_{i-1}) + \hat{\mathbf{V}}_i \quad (4.3)$$

From (4.1) and (4.2) then

Table 3.5 : Calibration and Misalignment Errors

	Samples	Misalignment $\delta\theta_0$ (degrees)	Calibration β
CODE 1, Leg 4	161	-1.4	-.006
Leg 5	153	-0.2	-.012
Leg 7	138	0.1	-.010
CODE 2, Leg 4-6	174	0.4	-.009
Leg 9	174	0.0	-.010

Table 3.5 : Calibration error β and misalignment angle $\delta\theta_0$ calculated from changes in apparent current which accompany changes in ship velocity using Eq 3.12. The large value of $\delta\theta_0$ during CODE 1, Leg 4 decreases substantially for subsequent cruises; this drop coincides with repair and realignment work performed on the gyrocompass following Leg 4.

Obtaining current estimates \hat{u} and \hat{v} is discussed in Chap. 4. With these estimates and the measured relative velocity \hat{U} and \hat{V} we can estimate a and b from the dependence of measured currents on the ship velocity. We might simply assume the currents should be uncorrelated with the ship velocity and calculate a and b from the measured correlations and Eq 3.8 above. Even better, we can consider *local* changes in measured currents which accompany local changes in ship velocity. Define measures of change in current and ship velocity by

$$\hat{q} = \frac{1}{2}(\hat{u} - \hat{u}_0) - \hat{u} \quad (3.11)$$

$$\hat{Q} = \frac{1}{2}(\hat{V} - \hat{V}_0) - \hat{V}$$

where \hat{u} , \hat{u}_0 , and \hat{u}_1 are the independent current estimates obtained steaming toward, steaming away from, and while on station respectively, with corresponding definitions for the relative velocity estimates \hat{V} . Then for each station we can form an estimate of the constants a, b from Eq 3.8 by assuming that the true values q and Q are uncorrelated (i.e. that the change in true current is uncorrelated with the change in ship velocity), and by approximating the true relative velocity by the measured relative velocity.

$$\hat{a} = \hat{z}(\hat{q} \cdot \hat{Q}) / (\hat{Q} \cdot \hat{Q}) \quad (3.12)$$

$$\hat{b} = (\hat{q} \cdot \hat{Q}) / (\hat{Q} \cdot \hat{Q})$$

We can then simply average the estimates \hat{a} , \hat{b} . In practice, only estimates involving large Q for which the error signal should be correspondingly large, were used, and estimates lying more than 3 standard deviations from the mean were rejected.

Table 3.5 shows the results of this analysis for several CODE cruises. The calculation indicates a calibration error of about 1%, with uncorrected ship velocity being low. The large value of $\delta\theta_0$ observed during CODE 1, Leg 4 decreases substantially for subsequent cruises; this drop coincides with repair and realignment work performed on the gyrocompass following Leg 4. The data were corrected for the calibration error (assumed to be constant at 1%) and for the Leg 4 misalignment error before further analysis.

In summary, the heading measurement obtained from a Sperry-type gyrocompass contains several sources of error of sufficient magnitude to degrade estimates of the cross-ship relative velocity component. While most of these can be accounted for once their presence in the data is recognized, the rolling error arising from wave induced tilt and accelerations can not.

3.8. Calibration and Misalignment Errors

As the research vessel moves through the water, each component of its horizontal velocity can vary over a range from +500 cm/sec to -500 cm/sec. Since the currents may constitute as little as 1% of this signal, it is essential to recognize and remove errors which depend on the ship velocity.

Speed dependent errors arise from a wide variety of sources. Terms of order $(V/c)^2$ in the Doppler shift, constant errors in the oscillator frequency or speed of sound used, splaying of the acoustic beams, etc. have the effect of calibration errors, causing the ship velocity to be over or underestimated. Rotation of the transducer head relative to the gyro reference line, the misalignment angle, causes the relative velocity to be over or underrotated when referred to geographical axes.

Suppose the data contain errors caused by a calibration error, β , and a misalignment angle, $\delta\theta_c$. Then the measured horizontal components of relative velocity will be

$$\hat{U} = (1 - \beta)U \cos \delta\theta_c + (1 - \beta)V \sin \delta\theta_c \quad (3.7)$$

$$\hat{V} = (1 - \beta)U \sin \delta\theta_c + (1 - \beta)V \cos \delta\theta_c$$

where U, V are the true components of relative velocity. The inferred currents computed from Eq 1.2 will thus be related to the true currents u, v by

$$\hat{u} = u + bU + aV \quad (3.8)$$

$$\hat{v} = v + aU + bV$$

where

$$a = (1 - \beta) \sin \delta\theta_c \quad (3.9)$$

$$b = (1 - \beta) \cos \delta\theta_c - 1$$

If we can use the data to infer (a, b) , we can determine the calibration and misalignment angle errors as

$$\delta\theta_c = \tan^{-1} \left(\frac{a}{b+1} \right) \quad (3.10)$$

$$\beta = \left[a^2 - (b+1)^2 \right]^{1/2} - 1$$

rotation of the large fore component of velocity into the cross-ship component, the error currents will be polarized in the cross-ship direction, and will increase with the speed of the ship. Unfortunately, errors $\delta\theta$ of this order of magnitude cannot be ruled out.

The heading data for this study were taken directly from the ship's Sperry Mk.37 master gyrocompass. One reading was taken for each acoustic pulse (0.6 sec sampling). To provide a heading measurement, the gyrocompass must sense its orientation relative to 3 directions. The fore-aft axis of the ship, the direction of gravitational acceleration and the rotation axis of the Earth provide these reference directions. An error in the detection of any one of these will yield an error in the measured heading. A complete discussion of the mechanics of gyrocompasses will not be undertaken here, and interested readers are referred to texts such as Arnold and Maunder (1961) or Wrigley *et al.* (1969). Table 3.4 summarizes some characteristics of measurement errors which are present in gyrocompasses of the Sperry type. The misalignment angle is the constant angle between the gyrocompass fore direction and the fore direction defined by the acoustic beams. Fasham (1976) discusses a technique for determining this angle which requires steaming a course in a steady cross-wind at a variety of speeds and attributing covariance between foreward and portward relative velocity measurements to transducer misalignment. A test run using this procedure was made during CODE; it showed that during the test the acoustic transducer was aligned to within 0.2° of the fore-aft axis of the ship as defined gyroscopically by the heading. A post-processing method for estimating both the misalignment angle and calibration error is presented in the next section which requires neither special test courses to be run nor strong assumptions about the steadiness of the wind and horizontal structure of the current shear field to be made. The latitude error and velocity error in Table 3.4 are usually corrected in the course of normal ship operations. The crew manually enters the speed and latitude of the ship into compensators located on the bridge. Were this not the case, these corrections could have been applied (more accurately) in post-processing. Acceleration error, which takes the form of damped oscillations in the heading, at 84 minute period, following a maneuver involving north-south accelerations, can also be corrected in post-processing if the history of the ship velocity is known for a long enough time. The wave-induced rolling (also called quadrantal) error depends on the details of the gyrocompass construction and I am not aware of any method for removing it. The magnitude of 0.75° listed for this error comes from engineers at the Sperry Corporation (Herschel Porter, personal communication).

Table 3.4 : Heading Errors

Error	Forcing	Form	Magnitude
Misalignment Angle	installation error	constant	?
Latitude Error	λ	$-\gamma \tan \lambda$	1.6°
Velocity Error	$\dot{\lambda}$	$\tan^{-1} \left[\frac{V}{\Omega R \cos \lambda - U} \right]$	0.8°
Acceleration Error	$\ddot{\lambda}$	$-\gamma \left[\frac{\ddot{\lambda}}{R \Omega^2 \cos^2 \lambda} \right] \Delta V e^{-\gamma t} \sin \sqrt{1-\gamma^2} \omega_s t$	0.4°
Rolling Error	wave induced ship tilt	-	0.75°

where

γ = gyrocompass damping parameter, 2° for Sperry Mk 37

$\omega_s \equiv \sqrt{g/R}$, the Schuler frequency

R = radius of Earth

Ω = rotation rate of Earth

$$\zeta = \frac{\gamma \omega_s}{2\Omega}$$

λ = latitude

(U, V) = (east, north) ship velocity

ΔV = change in V during maneuver, assumed to occur quickly compared to $2\pi/\omega_s$

t = time since maneuver

Table 3.4 : Heading Errors. This table lists several common errors which may be present in gyrocompass data. Magnitudes assume an operating latitude of 38° N, a course due north at 10 knots, and a maneuver in which the ship reverses course over a time which is short compared with the Schuler period. With the exception of the rolling error, these may be corrected either at the gyrocompass or in post-processing.

$$\hat{u} = \frac{6 \Delta t}{N(N-1)(N-2)} \sum_{i=1}^N (2i-N) \sum_{j=1}^N \hat{\xi}_j$$

$$= \frac{6 \Delta t}{N(N-1)(N-2)} \sum_{j=1}^N \hat{\xi}_j \sum_{i=1}^N (2i-N)$$

or

$$\hat{u} = \frac{6}{N(N-1)(N-2)} \sum_{i=1}^N i(N+1-i) \left(\frac{\hat{x}_i - \hat{x}_{i-1}}{\Delta t} - \hat{V}_i \right) \quad (4.38)$$

This is identical to the results (4.14), (4.22) since $N = 2M + 1$.

The two methods of deriving the filter produce the same estimator, but each provides a different piece of supplementary information. From the optimum estimator calculation we obtained (4.23), the expected rms error in the filtered estimate. On the other hand, the least squares formulation provides not only a current estimate \hat{u} (4.34) from the slope of the drift, but also an estimate of the intercept \hat{d}_0 . Since the drift at time zero must be zero, \hat{d}_0 is just minus the error in the initial fix \hat{x}_0 . By correcting the initial position and integrating $(\hat{u} - \hat{V}_i)$ over time, an improved estimate of the ship's position can be obtained. This allows the location to which the estimate applies to be determined more reliably than would be possible by using raw fixes alone.

4.6. Optimum Filtering

The result (4.24) gives the expected rms error for the estimator (4.38). But because we have assumed the true current is constant (or, more precisely, that 4.25 holds), Eq 4.24 predicts that this rms error will decrease to zero as the filter length N is increased. In fact, of course, at sufficiently large N , Eq 4.25 no longer is a valid assumption, and increasing the filter length will increase the error in the estimate by oversmoothing true structure in the current field. Choice of an appropriate filter length is achieved by minimizing the net error due to both sources, which can be written as

$$(\hat{u} - u)^2 = \int S_{uu}(f) (1 - W(f))^2 df + \int S_{\epsilon u \epsilon u}(f) W^2(f) df \quad (4.39)$$

where the first term represents loss of signal due to filtering and the second term represents the noise which passes through the filter. $W(f)$ is the transfer function of the filter,

$$W(f) = \sum_{k=-M}^M w_k e^{-2\pi i k f \Delta t} \quad (4.40)$$

which, after some tedious algebra, can be determined for the optimum estimator weights (4.22) to be

$$W(f) = \frac{3}{2N(N-1)(N-2)} \frac{(N-2)\sin N\pi f \Delta t - N\sin(N-2)\pi f \Delta t}{\sin^3 \pi f \Delta t} \quad (4.41)$$

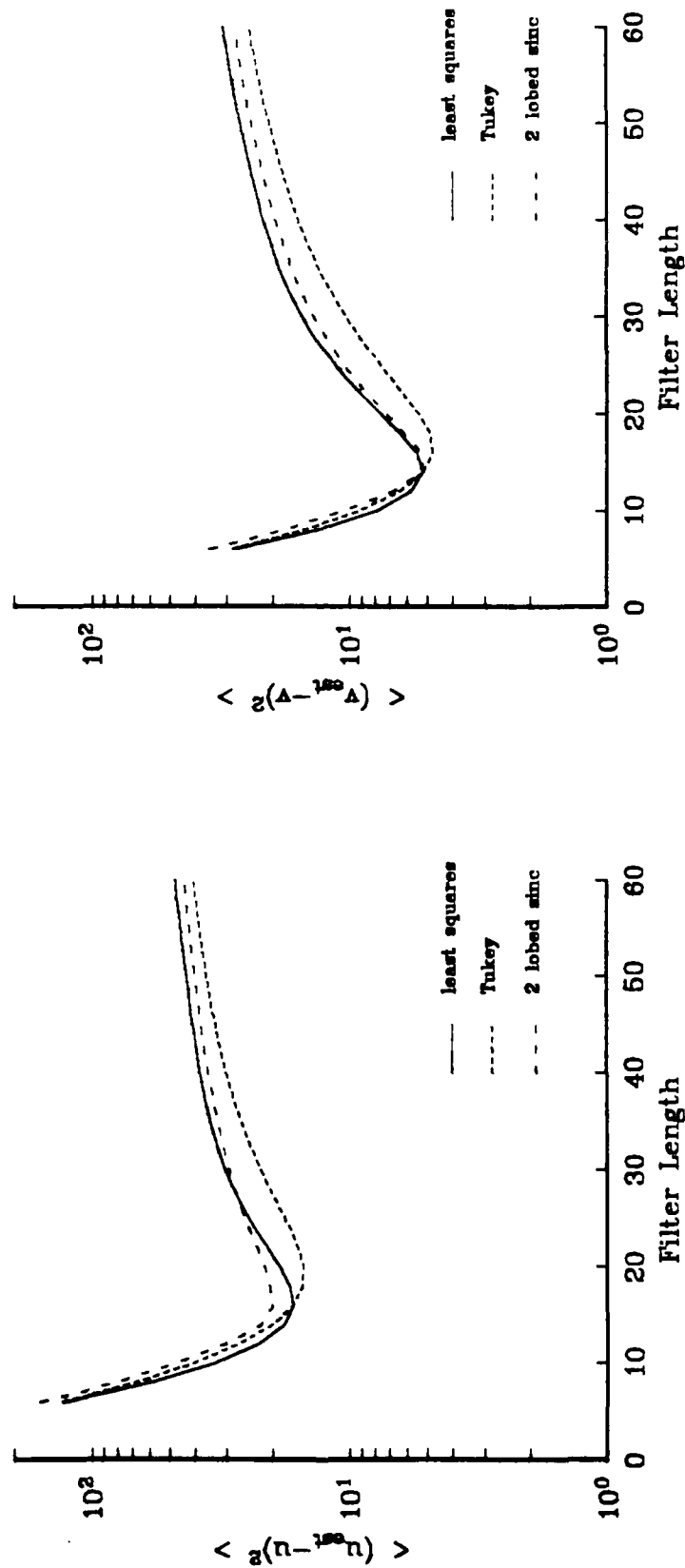


Fig. 4.4 : The mean square error in filtered fix-to-fix current estimates ($\text{cm}^2 \text{sec}^{-2}$) is predicted as a function of filter length (fix intervals) for 3 filters using Eq 4.39, the spectrum of measurements (Fig. 4.2) and the inferred noise spectrum. Increased estimation error at short filter length arises from underfiltering of noise, while rise at longer filter length arises from suppression of true signal. The least squares filter achieves its minimum mae most rapidly, while the Tukey and truncated sinc filters suppress less signal in the case of overfiltering (i.e. where the statistics of the signal deviate from the assumptions of the objective analysis).

Since we have a model of the noise spectrum $S_{\hat{u}\hat{u}}$ and can infer S_{uu} from $S_{\hat{u}\hat{u}}$ and $S_{\hat{u}\hat{u}u}$, (4.39) can be evaluated as a function of the filter length N , and the value of N which minimizes $\sigma^2 = (\hat{u} - u)^2$ can be chosen. This technique also allows us to test the performance of alternative filters by simply inserting the appropriate transfer function into (4.39). The results of such a test are shown in Fig. 4.4 for 3 choices of filter - the least squares filter of Eq 4.34, a lowpass Tukey filter and a truncated sinc filter. The results are nearly identical for the three filters, with the least squares estimator yielding somewhat lower expected errors at short filter lengths and achieving minimum error more rapidly than the other low pass filters, and the other filters removing somewhat less signal in the case of overfiltering. In all cases, the mean square error drops steeply to the minimum, then rises slowly as the filter length is increased past the optimum value. Since we don't know with great confidence where the signal truly begins, the data were processed conservatively by using a filter of length $N=30$. Fig. 4.4 suggests an rms uncertainty of 2-3 cm sec in v , the alongshore current, and 4-5 cm sec in u , the cross-shore current, should be expected.

4.7. Vertical Current Profiles

The analysis to this point has focussed on predicting the current $\mathbf{u}(z_k)$ at a single depth z_k from acoustic measurements for that depth and from navigational data. To estimate the current at another depth, of course, the filtering procedure could simply be repeated using the acoustic data from the new depth. However, we have seen that the acoustic data is much less noisy than the navigation data, so that while 30 minutes of combined measurements are required to determine the absolute current at any level, vertical shears between levels can be determined from 5 minutes of acoustic data alone. Estimating the current at one depth using 30 minutes of data, the vertical profile of currents could then be determined from the shear over the shorter 5 minute period, retaining shorter scale variability in the current profiles. To obtain the current profiles for this study, 30 minute time series of vertically averaged \mathbf{V} were used to estimate the average current over a vertical slab of ocean. The vertical deviations from this average were then determined from the central 5 minute average profile of \mathbf{V} . Use of this slab determination results in equal smoothing of currents at all levels by the 30 minute filter.

4.8. Summary

The goal of this section was to use the imperfect measurements of position and relative velocity described in Chapter 3 to best extract the current. Our approach has been to use each pair of adjacent fixes and the average relative velocity between them to produce a single noisy measurement of the current. We have shown that

- (a) the spectrum of such measurements shows a strong spectral gap separating two

peaks.

- (b) the high frequency peak is modelled well over most of its range by assuming it arises from white noise error in the position measurements.
- (c) the noise in an estimate \hat{u} formed by averaging N adjacent measurements decreases as $1/\sqrt{N}$, and
- (d) an estimator formed by increasing the time between fixes is equivalent to (c).

By assuming the true current obeyed (4.25) over the filtering interval, we

- (e) derived the estimator (4.14 or 4.22) which gives the minimum mean square error (4.24), and
- (f) showed that this estimator is equivalent to making a least squares estimate of the drift of a water parcel.

By assuming the true current had variability described by the measured spectrum after removing the spectrum of white noise fix errors, we

- (g) tested the robustness of the optimum estimator, and found it to be not much better or worse than other possible low pass filters, and
- (h) found the dependence of rms error in the filtered signal on filter length.

We then commented on how to extend the single depth analysis to vertical profiles.

Chapter 5

COMPARISON WITH MOORED CURRENT METERS

5.1. Introduction

The CODE 2 moored array of current meters provides an independent set of measurements taken while the Doppler acoustic log was being operated. By comparing the current meter measurements with those inferred from the shipboard Doppler as it moved through the current meter array we may learn about the reliability of the shipboard Doppler technique. Furthermore, the fixed current meter movable DAL geometry yields simultaneous measurements along a continuum of spatial separations. This means that spatial scales can be investigated directly with the combined data set, without the inherent mixing of space and time variability to which survey measurements alone are subject.

The CODE-2 moored array (Fig. 5.1) was deployed in March 1982 by scientists from Scripps Institution of Oceanography and Woods Hole Oceanographic Institution, and was recovered in July-August 1982. Moorings were set along 4 lines (designated I, N, C, and R from north to south) perpendicular to the coast, in water depths of 60m (except the I line), 90m, 130m and 400m (C line only). Details of mooring locations and instrument depths are given in Table 5.1.

Data from these moorings were kindly made available by R. Davis, C. Winant and R. Beardsley as vector averaged hourly currents.

5.2. Comparison within 1 km

Direct comparison between the DAL and current meter measurements was made as follows:

Whenever the ship location (from LORAN-C positions corrected as described in Chapters 3 and 4) was within 1 km of the nominal location of a mooring (also corrected for constant LORAN-C offset), the DAL profile was linearly interpolated to the current meter depths, and the hourly current meter values were linearly interpolated to the DAL measurement time. Current meters which were either too deep or too shallow for valid DAL estimates were not used. Comparisons are made using the alongshore and cross-shore components, where the alongshore direction is taken to be 317°T everywhere, except for the I moorings, where it is taken to be 0°T .

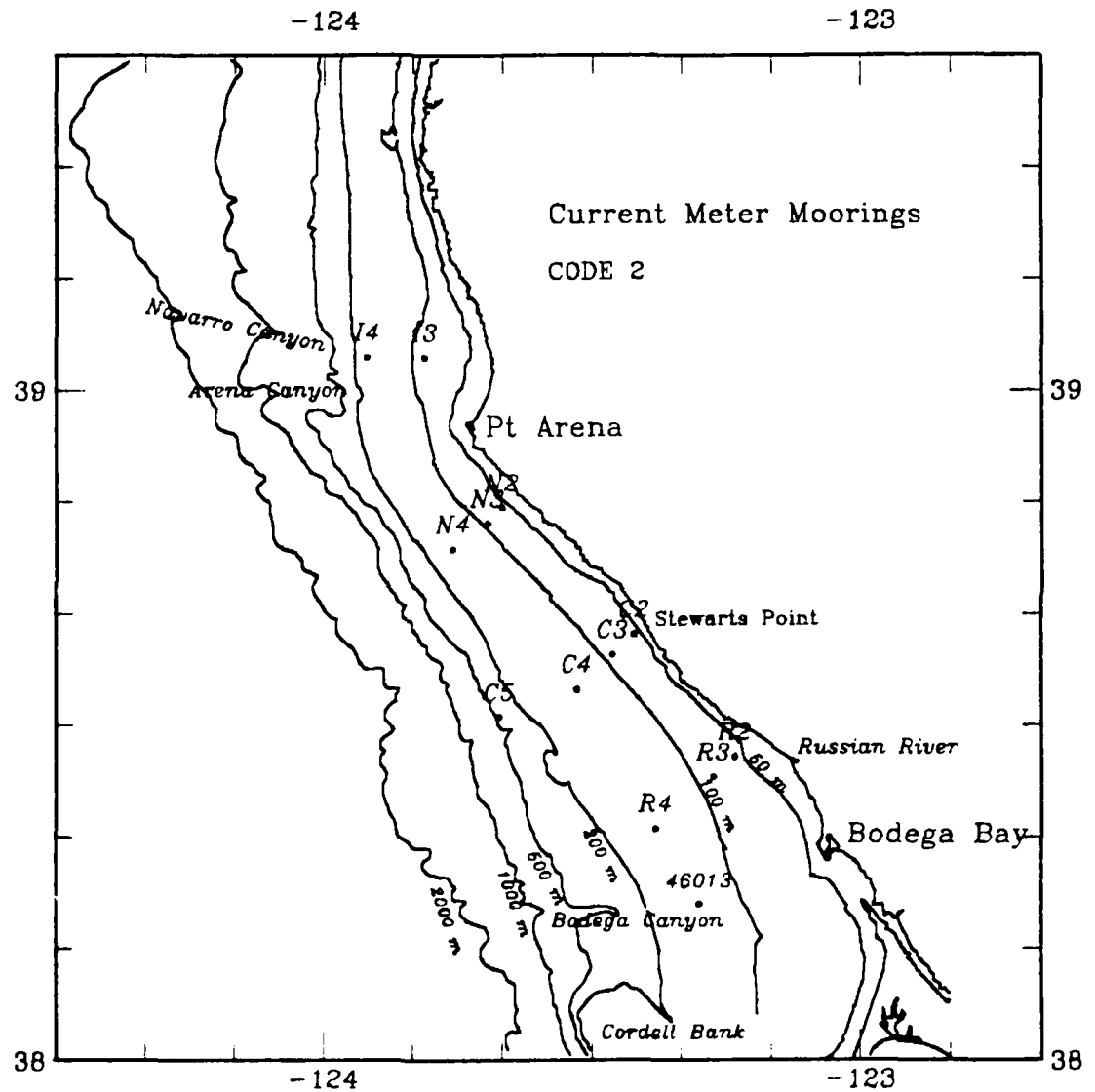


Fig. 5.1 : CODE 2 (1982) moored current meter array. Table 5.1 provides details on instrumentation at each mooring. Also shown is the location of wind buoy NDBO 46013.

Table 5.1 CODE 2 MOORED CURRENT ARRAY

mooring name	latitude	longitude	water depth (m)	mooring type	instr type	instr depth (m)	offshore dist (km)
I3	39° 3.00	123° 48.67	90	S	VMCM	10,20,53	10
I4	39° 3.00	123° 55.18	130	S	VMCM	10,20,53	19
N2	38° 49.50	123° 40.11	60	S	VMCM	10,20	3
	49.56	40.25		SS	VMCM	35.53	
N3	38° 48.07	123° 41.71	90	S	VMCM	10	7
	48.09	41.77		SS	VMCM	35.53,70.83	
	38° 45.79	123° 45.60		S	VACM	10	
N4			129		VMCM	20	
	45.71	45.55	130	SS	VMCM	35.55,70.90,110	14
					VACM	121	
C2	38° 38.16	123° 25.32	60	S	VMCM	10,20	2
	38.20	25.28		SS	VMCM	35.53	
	38° 36.38	123° 27.71	93	S	VMCM	5,15	
C3					VACM	10	7
	36.40	27.72	90	S	VMCM	10,20	
	36.35	27.70	90	SS	VMCM	35.53,70.83	
	38° 33.26	123° 31.68		S	VACM	10	
C4			130	SS	VMCM	20	15
	33.26	31.56			VMCM	35.55,70.90,110	
					VACM	121	
	38° 30.80	123° 40.25		S	VMCM	20,35,55	
C5	30.88	40.41	400	SS	VACM	70,110,150, 250,350	28
					VMCM	90	
R2	38° 27.17	123° 13.97	60	S	VMCM	20	5
	27.14	13.94		SS	VMCM	35.53	
R3	38° 25.38	123° 16.40	90	S	VMCM	10,20	9
	25.33	16.36		SS	VMCM	35.53,70.83	
	38° 20.76	123° 22.94		S	VACM	10	
R4			130		VMCM	20	22
	20.84	22.95		SS	VMCM	35.55,70.90,110	

Table 5.1 : CODE 2 moored array. S (SS) denotes a current meter string which is surface (sub-surface) moored. VACM (VMCM) denotes a Vector Averaging (Measuring) Current Meter.

Comparisons were performed for the entire CODE 2 data set over a wide range of processing options. Filter lengths of half hour, hour and two hours, filters of the least squares, Tukey and endpoint type, slab and single level determinations, as well as various calibration corrections were all tested. No alternatives to the half hour, least squares filtered, slab averaged, calibration corrected processing consistently yielded improvement in the comparison statistics. A substantial improvement in comparison results was obtained, however, by an *ad hoc* change from the nominal depths of the DAL range bins. By treating the acoustic data in range bin $n-1$ as if they had come from range bin n , the rms difference between current meter and DAL measured currents was dramatically reduced (typically 30% reduction in the variance of the difference signal). Subsequent measurements by Regier (personal communication) confirmed the presence of hardware sources for such delays in the Ametek electronics. The results presented here use the corrected depths for the measurements.

The intercomparison results are shown graphically by the scatter plots in Fig. 5.2; a statistical summary of the results is given in Table 5.2. In the table there are two columns which count the number of comparison points: the first, N_{tot} , gives the total number of comparison pairs (one DAL measurement per 5 minutes) and corresponds to the number of points shown in the scatter plots, while the second, labelled N_{indep} , counts only those samples for which distinct pairs of hourly current meter averages were used in deriving a time-interpolated current to compare with the DAL, and is the more applicable figure for determining significance levels.

The mean cross-shore current component u at each depth as measured by the DAL differs by 0.6 cm/sec or less from the mean over simultaneous measurements by the moored current meters; however the means for the alongshore component v differ by up to 1.6 cm/sec, with the DAL consistently showing stronger downcoast flow than the current meters. There is a strong cross-shore and vertical gradient in the mean alongshore component of current over the shelf, as we shall see later, and the differences in v may arise from small errors in our knowledge of the positions for the measurements being compared. Correlations between the two sets of measurements are high, ranging from .76-.82 for u and .95-.97 for v . Standard deviations of the differences are 4.1-5.4 cm/sec in u and 3.6-4.4 cm/sec in v ; recall that errors of 4-5 cm/sec in u and 2-3 cm/sec in v were expected in the DAL currents from the considerations in Chapter 4. The size of the differences between DAL and moored current meter measurements of currents was found to increase by small but statistically significant amounts as either the ship's speed or distance from the mooring increased, indicating that both measurement errors and geophysical variability contribute to observed differences. No tendency was found for the mean or fluctuating differences to have a preferred orientation relative to the ship. The variance of the DAL measurements is consistently larger than that of the current

Table 5.2: Current Meter - DAL Comparison Statistics

CROSS-SHORE CURRENTS									
z	N _{tot}	N _{diff}	\bar{u}_{DAL}	\bar{u}_{CM}	var{ u_{DAL} }	var{ u_{CM} }	covar	corr	Δ_{std}
20 m	1022	194	-1.0	-1.3	74.2	71.3	58.4	.80	5.3
35 m	1001	195	.4	.1	50.2	41.4	35.8	.79	4.5
50 m	927	178	.6	.1	50.0	33.3	33.3	.82	4.1
70 m	245	62	.8	.2	60.8	38.7	28.3	.79	4.8
90 m	225	52	1.8	1.5	62.1	35.4	35.6	.76	5.1

ALONG-SHORE CURRENTS									
z	N _{tot}	N _{diff}	\bar{v}_{DAL}	\bar{v}_{CM}	var{ v_{DAL} }	var{ v_{CM} }	covar	corr	Δ_{std}
20 m	1022	194	-6.7	-6.4	388.9	379.5	374.3	.97	4.4
35 m	1001	195	-6.1	-4.8	206.0	155.7	173.5	.97	3.9
50 m	927	178	-2.3	-1.6	221.3	179.0	193.6	.97	3.6
70 m	245	62	-0.7	-5.1	187.4	146.2	158.6	.96	4.0
90 m	225	52	-4.4	-2.8	156.5	121.6	131.6	.95	3.9

VACM vs VMCM, z = 10 m								
comp	N	VACM	VMCM	var{VACM}	var{VMCM}	covar	corr	Δ_{std}
u	2916	-4.1	-3.6	125.3	116.6	112.0	.93	4.2
v	2916	-3.9	-6.1	644.9	683.0	649.9	.98	5.3

Table 5.2: Current meter - DAL comparison statistics. Whenever the DAL was within 1 km of a mooring, comparison of DAL and moored current meter measurements was made. Averages and variances for each instrument are shown, as are covariance, correlation and standard deviation of the difference between measurements from each instrument. Also shown is a comparison between the only closely spaced pair of moored instruments in CODE, a VACM and a VMCM both at 10m near C3.

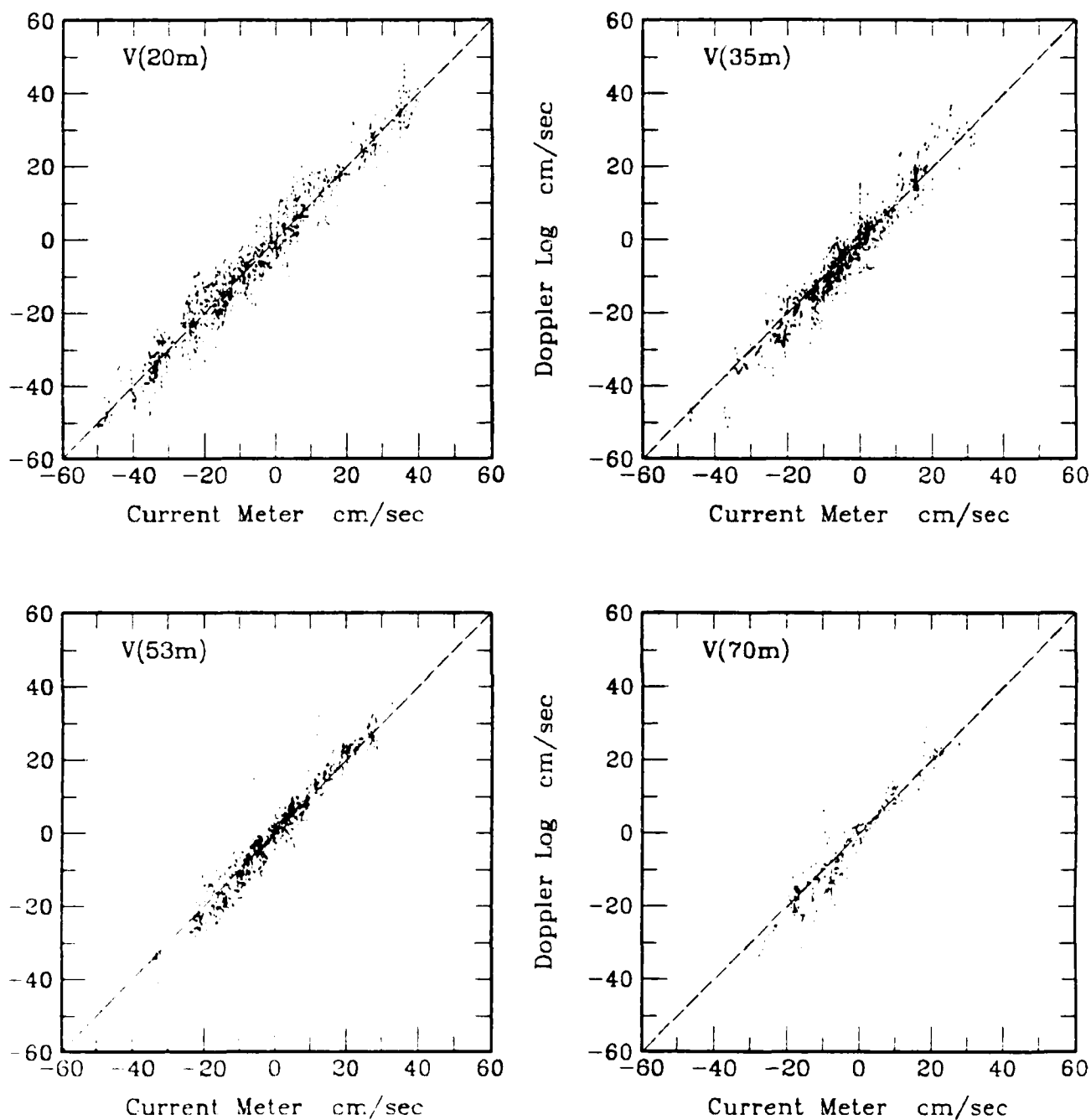


Fig. 5.2a : Comparison of all DAL current measurements (alongshore component) made within 1 km of a current meter mooring with the simultaneous current meter measurement. At both 20m and 35m depth, over 1000 pairs of measurements are plotted. See Table 5.2 for a statistical summary of these results.

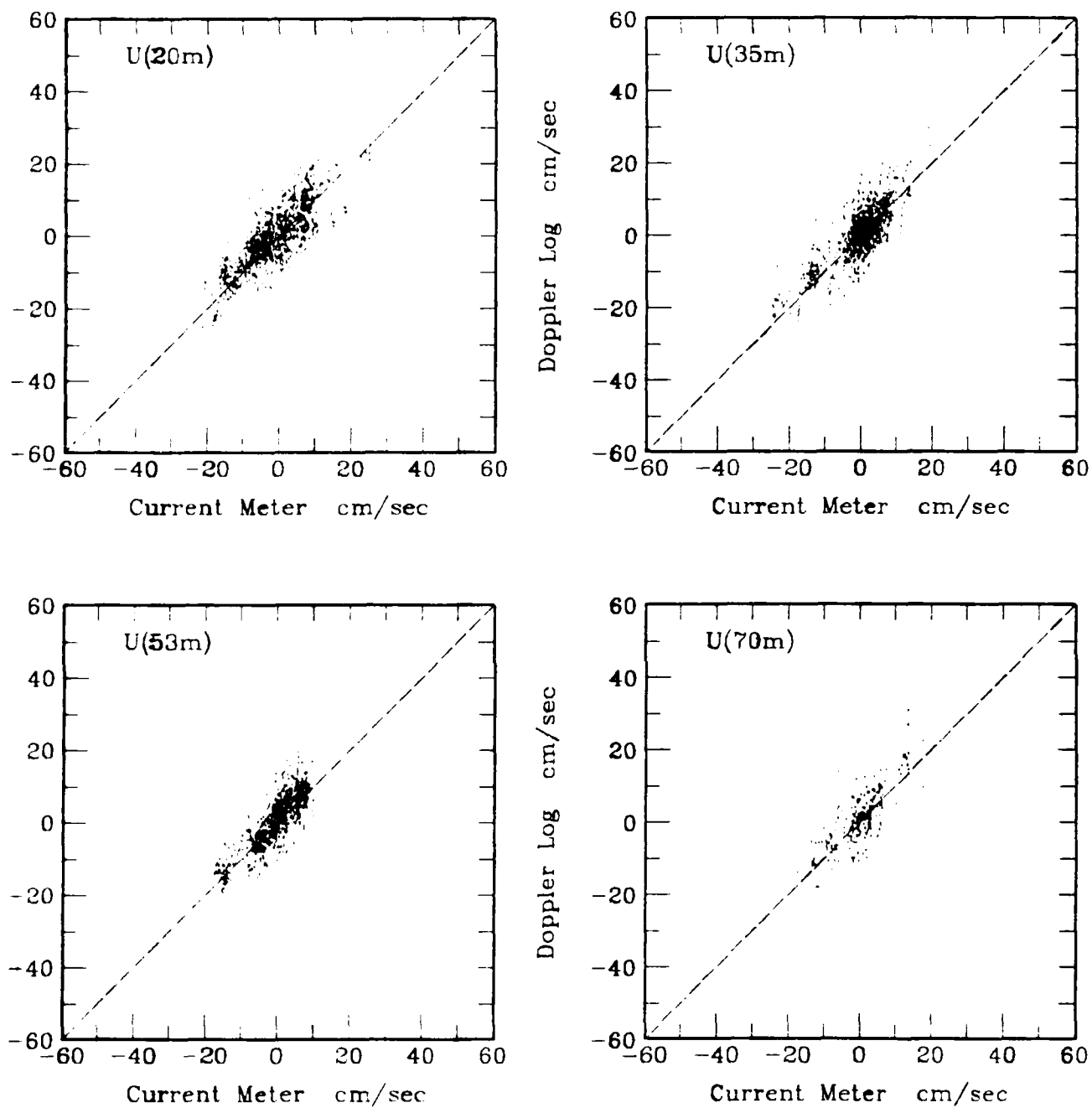


Fig. 5.2b : Same as Fig. 5.2a, except for cross-shore components.

meters measurements.

In assessing this comparison it is useful to know how two "standards" compare with one another. Therefore direct comparison was also made between the only pair of current meters in CODE 2 which were located at the same depth and closely spaced horizontally, one a VACM, the other a VMCN. Both were located 10m below surface moorings in approximately 90m of water along the C line; the separation between moorings was approximately 100m, considerably less than the typical distance the ship occupied during comparison times. The comparison was made for the common time period of 121.5 days beginning at 1300 GMT on 24 March 1982. The results are also presented in Table 5.2. The differences between the measurements are surprisingly large - mean differences of 0.5 and 2.5 cm sec and standard deviations of the differences of 4.2 and 5.3 cm sec in u and v respectively. These differences do not correlate well with the currents, and so are not easily explained in terms of fouling, broken fans, calibration errors, etc.

The comparison results are quite encouraging and demonstrate that meaningful current measurements can be obtained from the shipboard DAL. More accurate measurements of position and heading should reduce errors further. An important obstacle which is more difficult to surmount is assessing and correcting for variability in the acoustic environment below the ship, especially the influence that bubbles have on sound speed and thus on the relation between Doppler shift and relative velocity (cf Eq. 2.1).

5.3. Comparison at Larger Separations

Moored current meters continuously measure the current at a single location. The shipboard DAL measures current at the ship's location. Thus as the ship moves in the vicinity of a current meter the two instruments form an adjustable array and allow simultaneously measured currents to be compared at a variety of spatial lags. During CODE the C-line was the region for which shipboard sampling was most intensive (Appendix), and thus statistical reliability highest. Fig. 5.3a shows how the mean currents measured by the DAL varied across the shelf along the C line. The origin is taken at the C3 mooring. A strongly varying mean field, as observed for $v(x)$, increases the apparent noise for intercomparison experiments such as the one just discussed. Divergence in the mean cross-shore current u, expected in the presence of coastal upwelling, is clearly seen. Fig. 5.3b shows how the correlation between DAL and moored measurements at C3 fall off as a function of offshore separation of the ship from the mooring. For u, correlation between the instruments falls to values not significantly different from zero at separations less than the mooring separations, while for v, the cross-shore correlation length is substantially longer. Fig. 5.3c shows that the rms difference between currents grows rapidly as a function of cross-shelf separation.

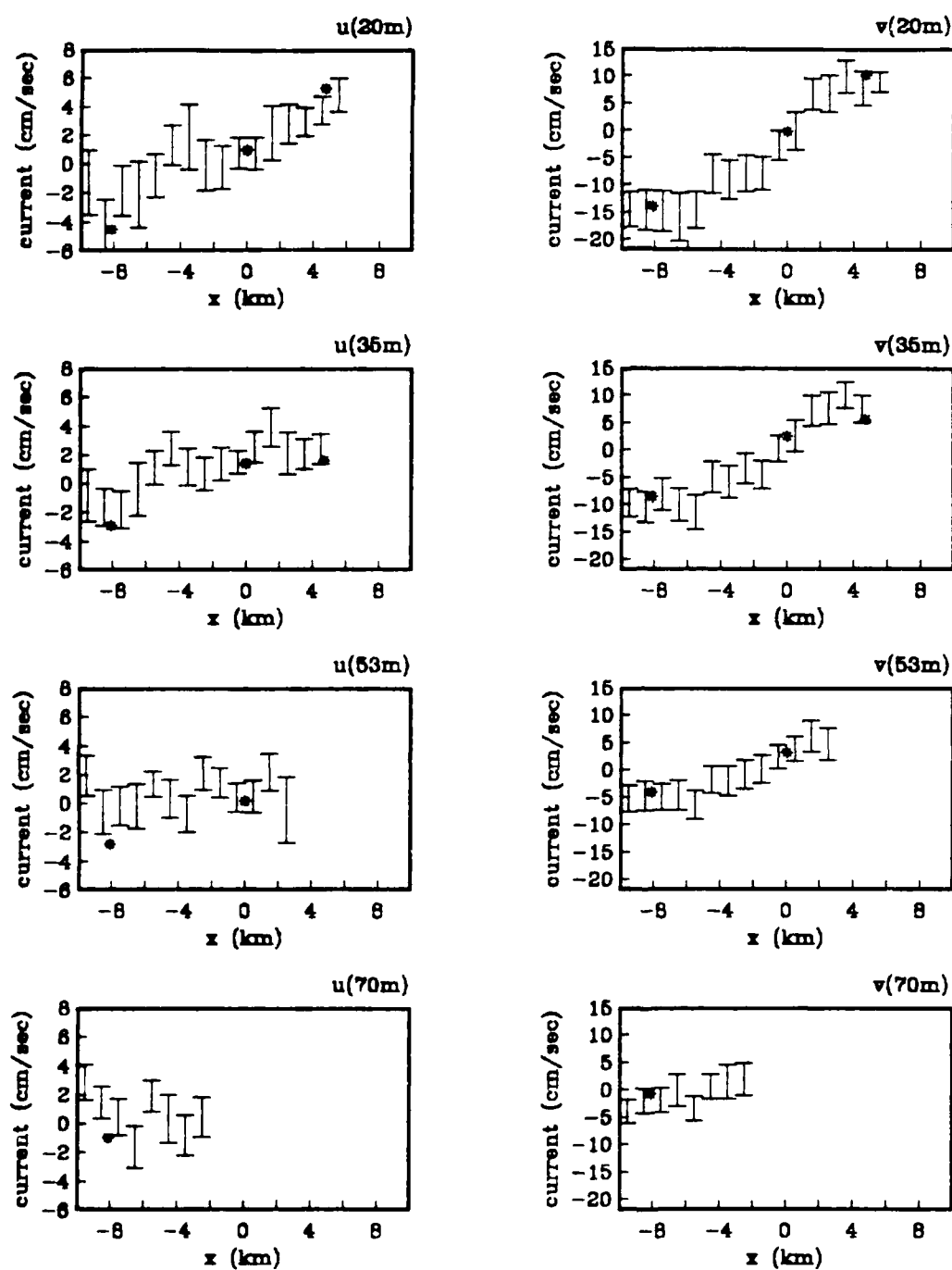


Fig. 5.3a : Average DAL cross-shore and along-shore currents u and v along the Central Line at depths of current meters (20m, 35m, 53m, and 70m), as a function of cross-shelf separation from the C3 mooring. Stars show current meter averages at C2, C3 and C4 over same sample times. Note the strong mean shear in v and divergence in u across the shelf.

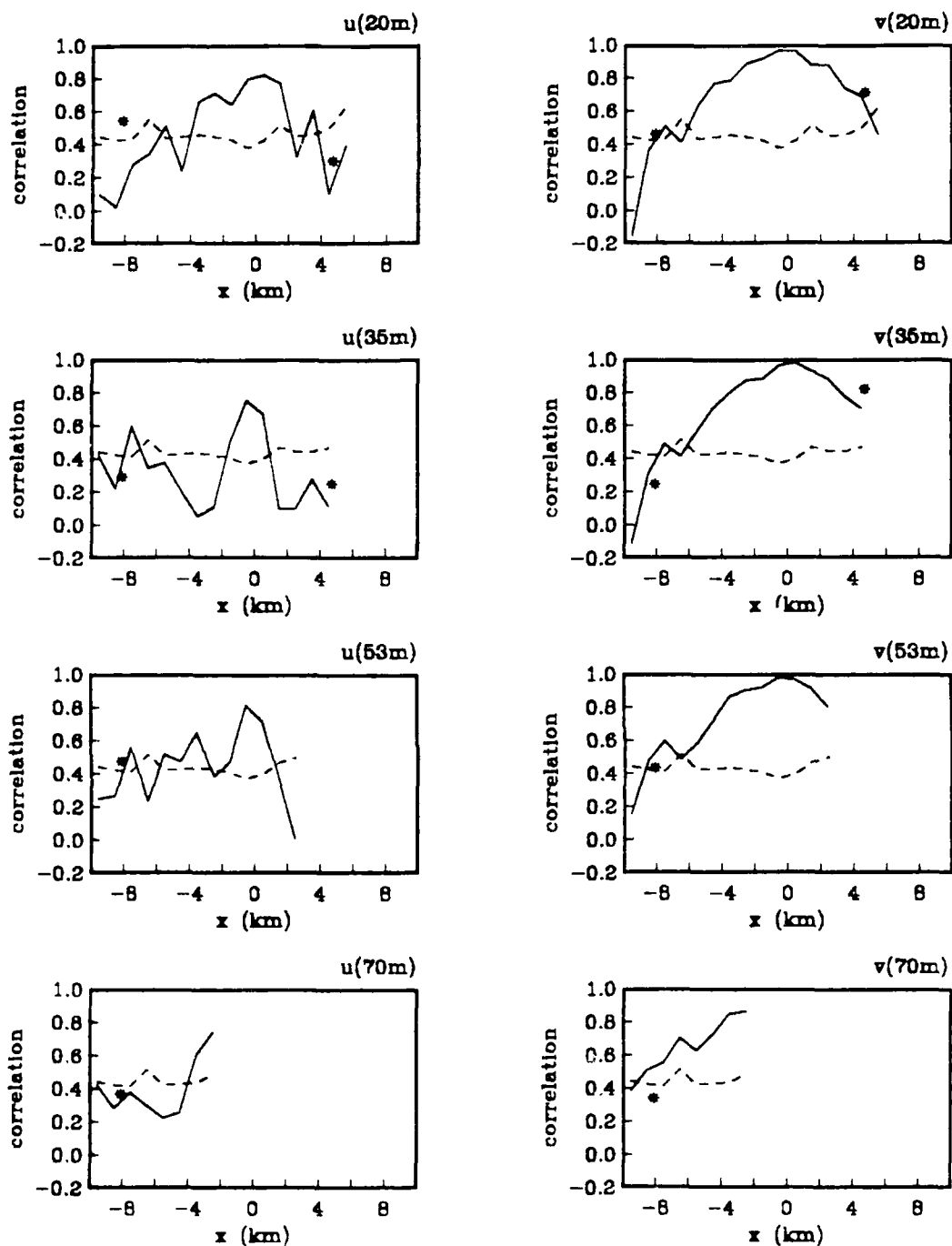


Fig. 5.3b : Correlation between simultaneous DAL and C3 current meter currents as a function of cross-shelf separation from the C3 mooring. Dashed line gives 95% confidence level for correlation over available samples. Stars show C3 correlation with current meters at C2 and C4.

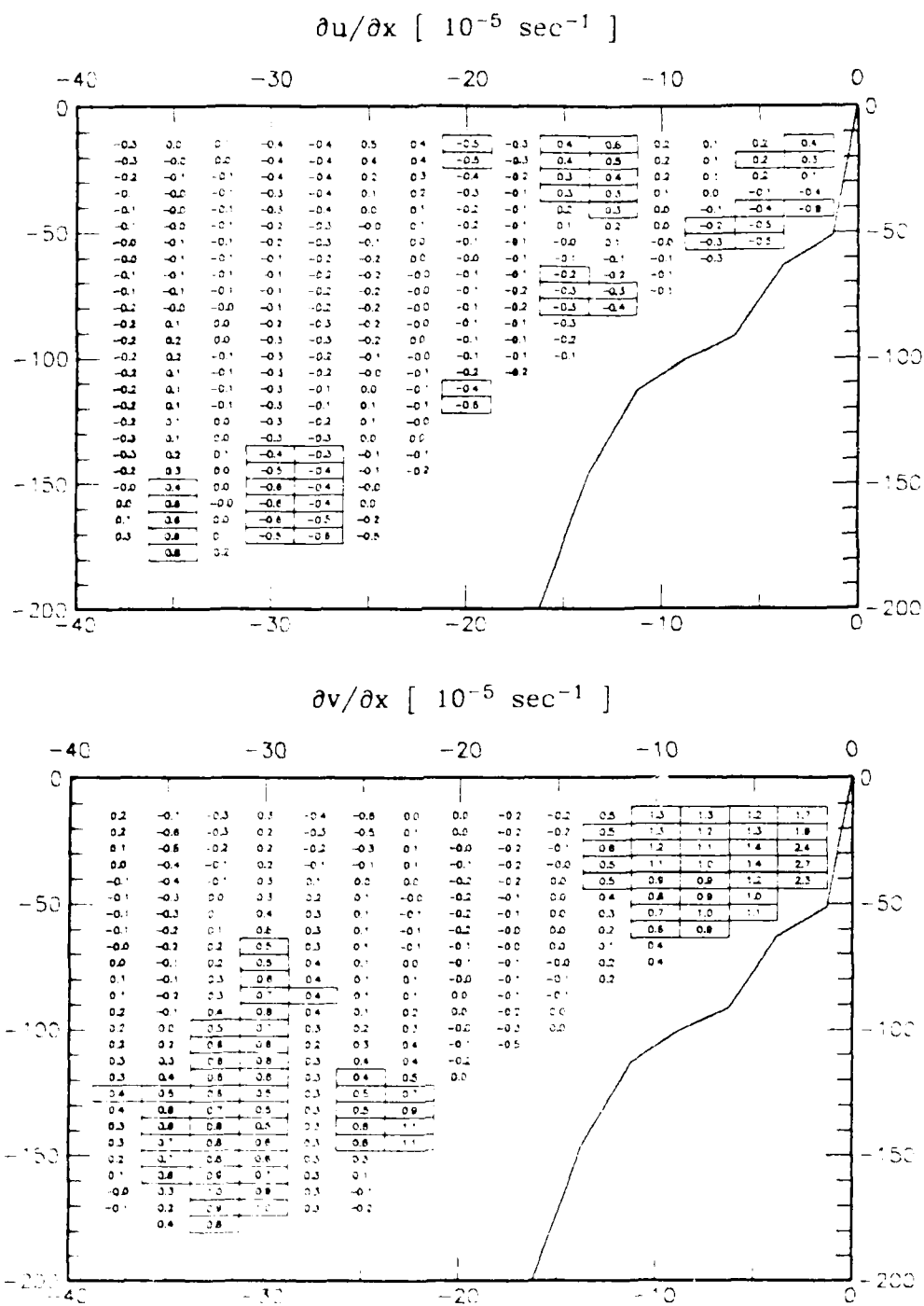


Fig. 6.3f : Cross-shore divergence $\partial u / \partial x$ and shear $\partial v / \partial x$ in mean currents, calculated as in Fig. 6.3e. Values enclosed in boxes are significantly different from zero at the 95% confidence level, assuming errors in the mean are given by Fig. 6.3d and that these errors are independent between adjacent bins. The latter is almost certainly optimistic.

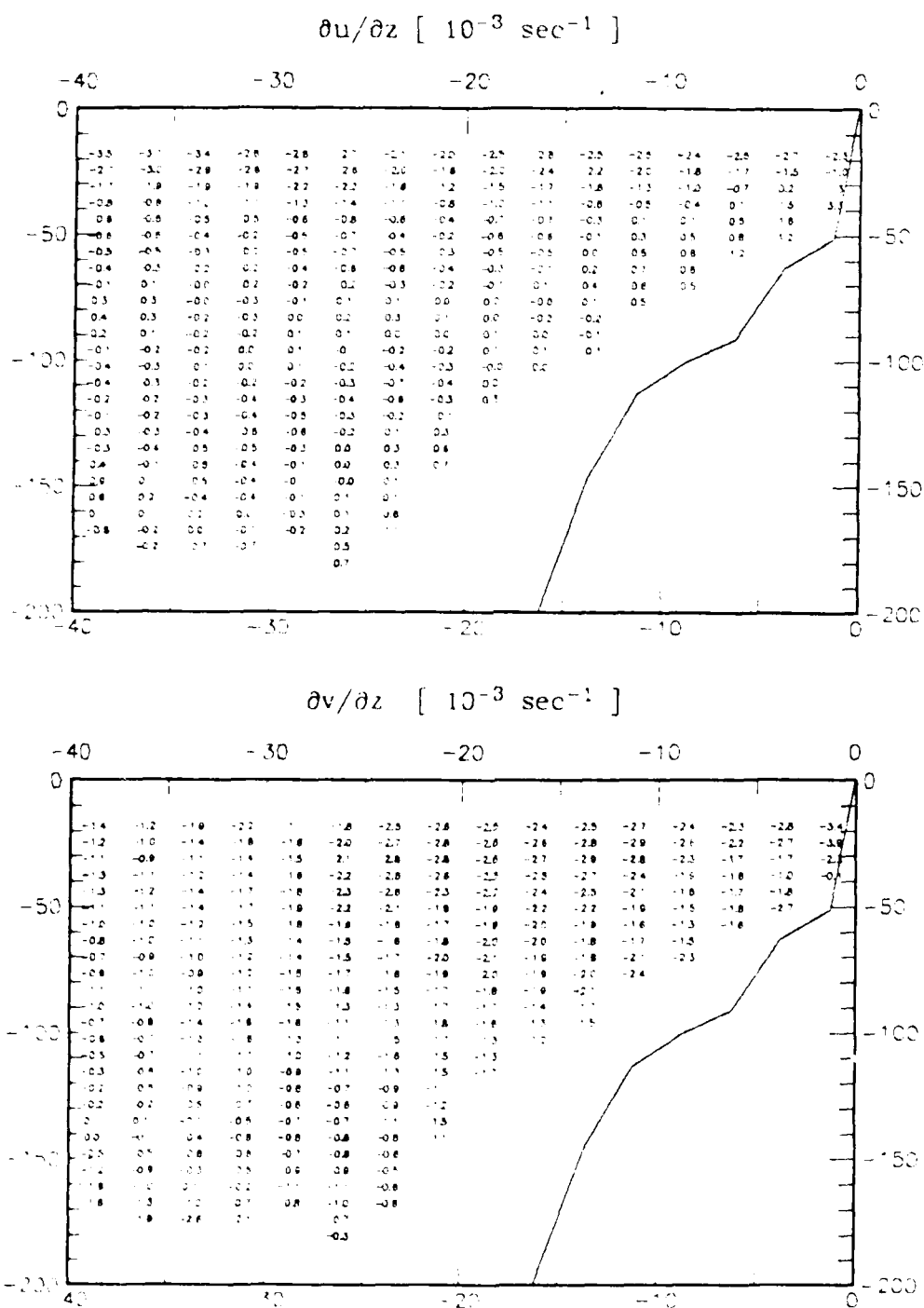
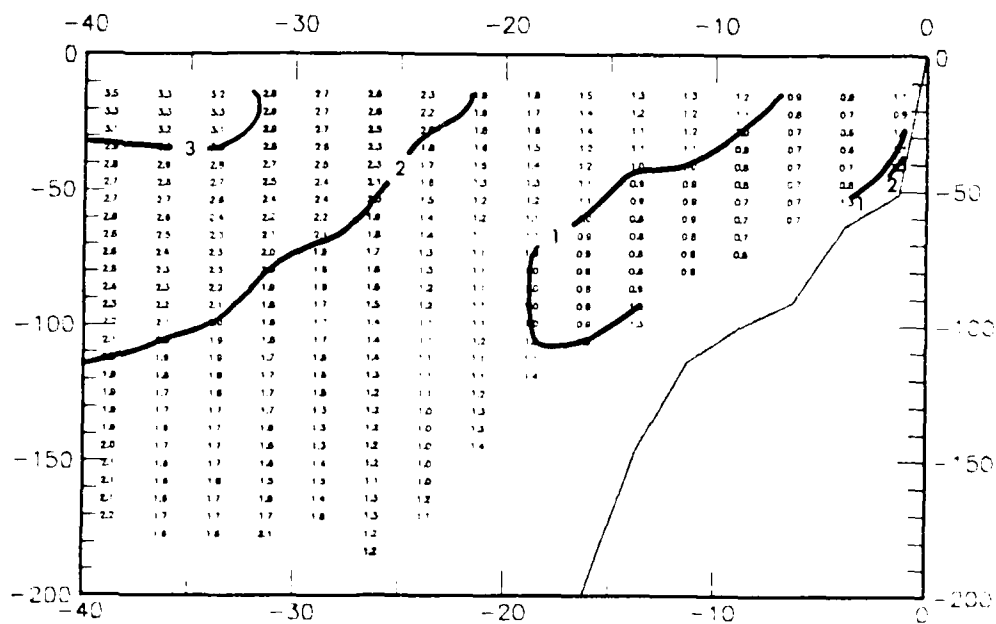


Fig. 6.3e . Vertical shear in the mean fields $\partial u / \partial z$, $\partial v / \partial z$. First differences of the mean fields (Fig. 6.4b) were smoothed using a (3×3) triangular weight filter.



RMS expected error of mean along-shore current

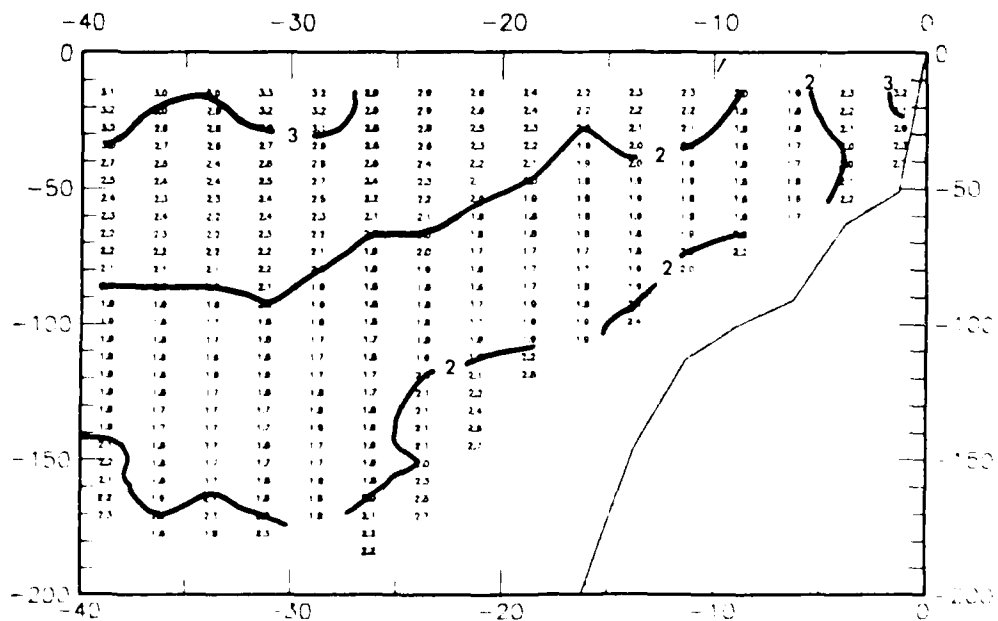


Fig. 6.3d : RMS expected error of the average of $u(x,z)$, $v(x,z)$ (cm sec), assuming observations in Fig. 6.3a are independent.

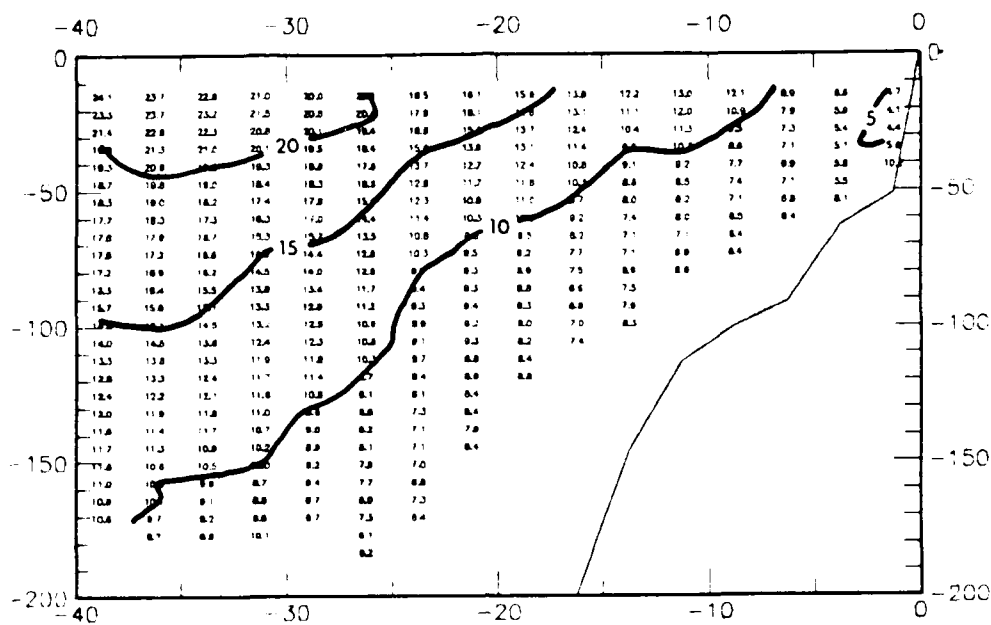
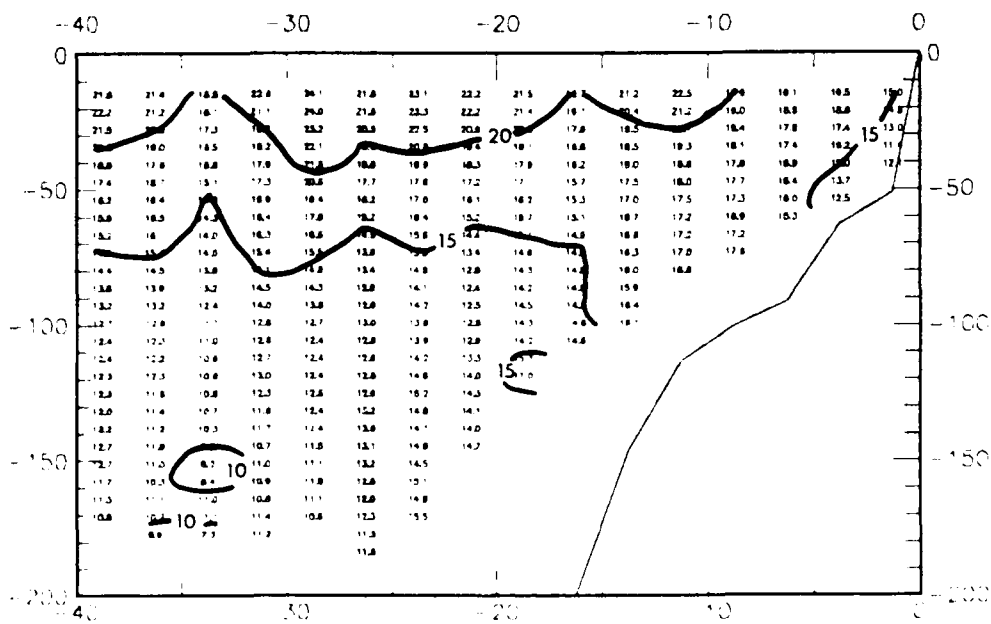
Standard deviation of cross-shore current $\sigma_u(x,z)$ Standard deviation of along-shore current $\sigma_v(x,z)$ 

Fig 6.3c . Standard deviation of fluctuations in $u(x,z)$, $v(x,z)$ (cm/sec) for observations in Fig 6.3a

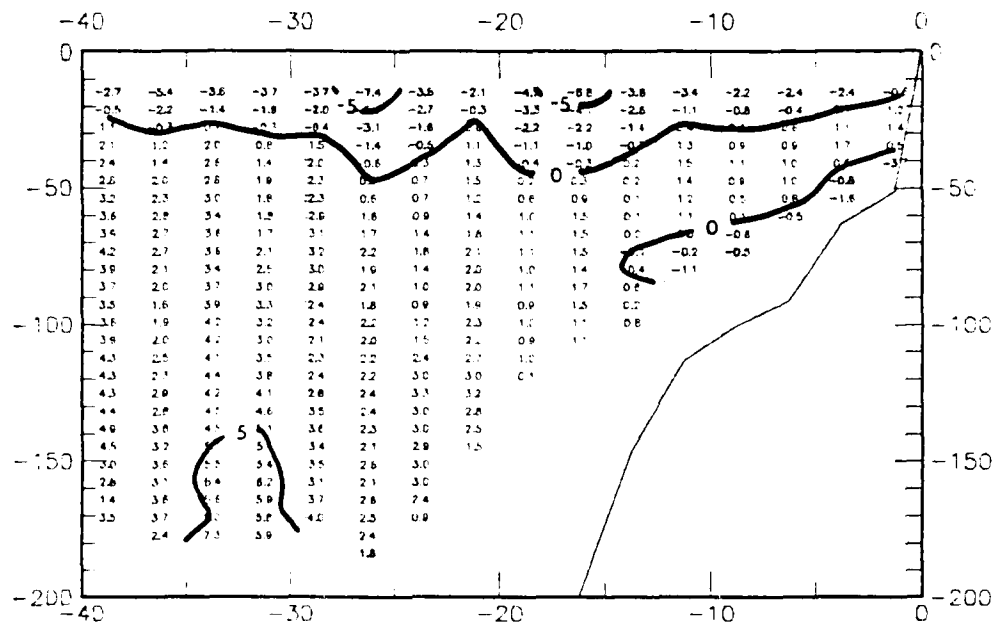
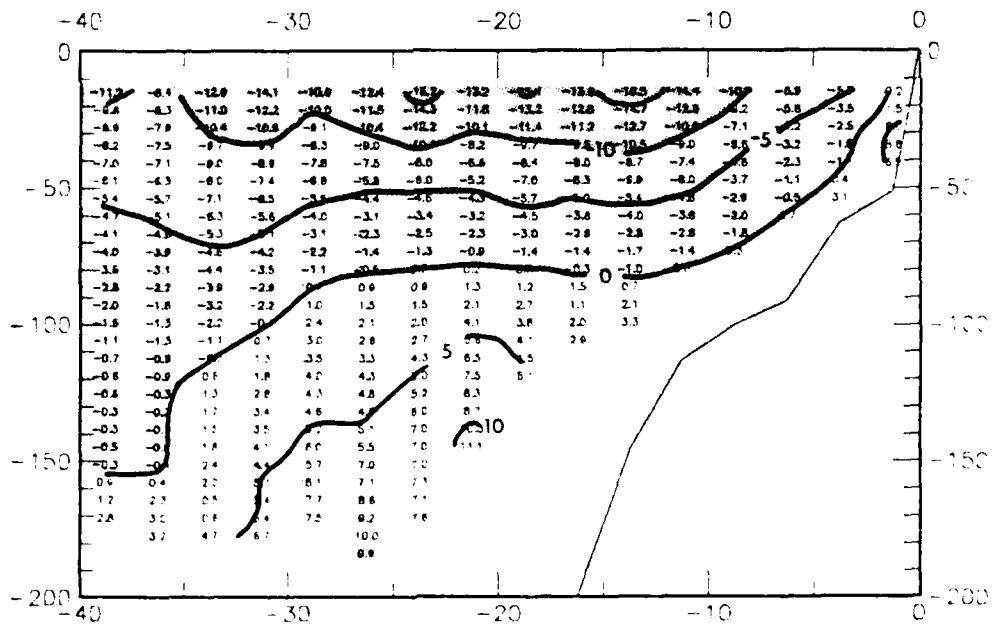
Average cross-shore current $u(x,z)$ Average along-shore current $v(x,z)$ 

Fig. 6.3b : Average cross-shore and alongshore currents $u(x,z)$, $v(x,z)$ (cm/sec) over the observations of Fig. 6.3a.

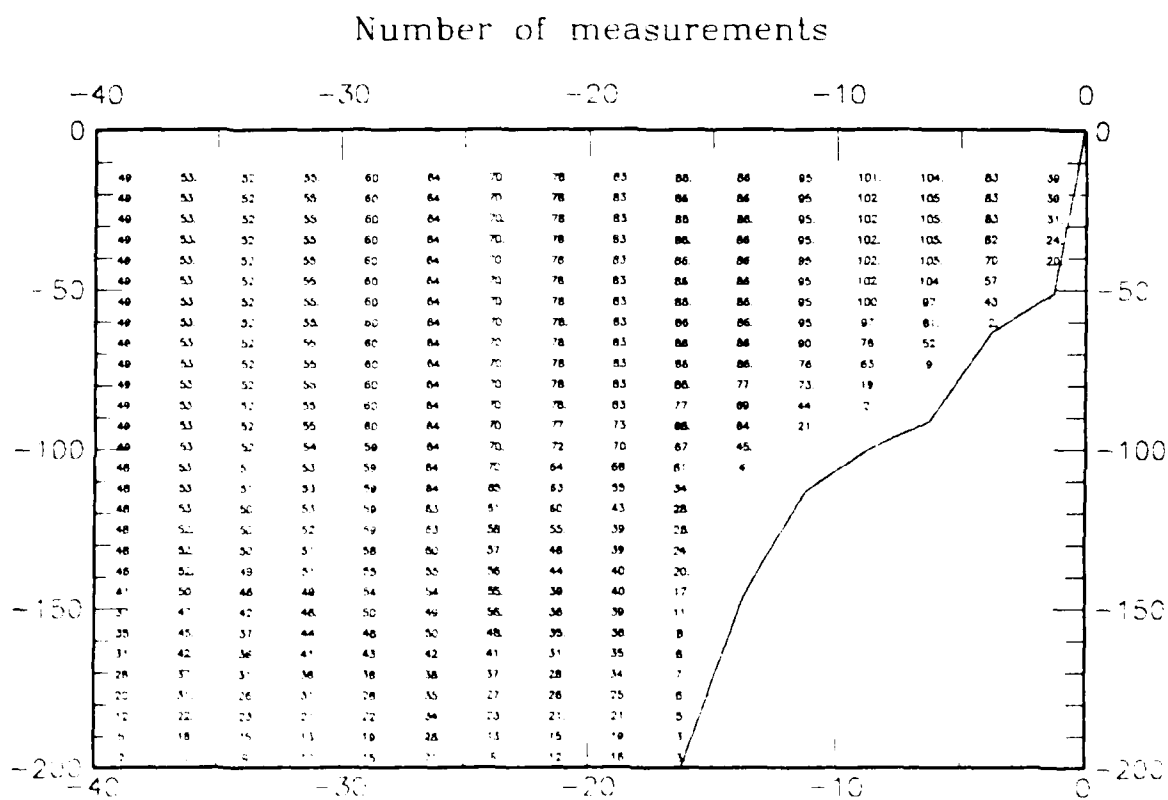


Fig. 6.3a : Number of observations at each depth (m) and distance from shore (km). Each observation was made along one of the primary CTD lines in Fig. 6.2a following the spring transition to upwelling.

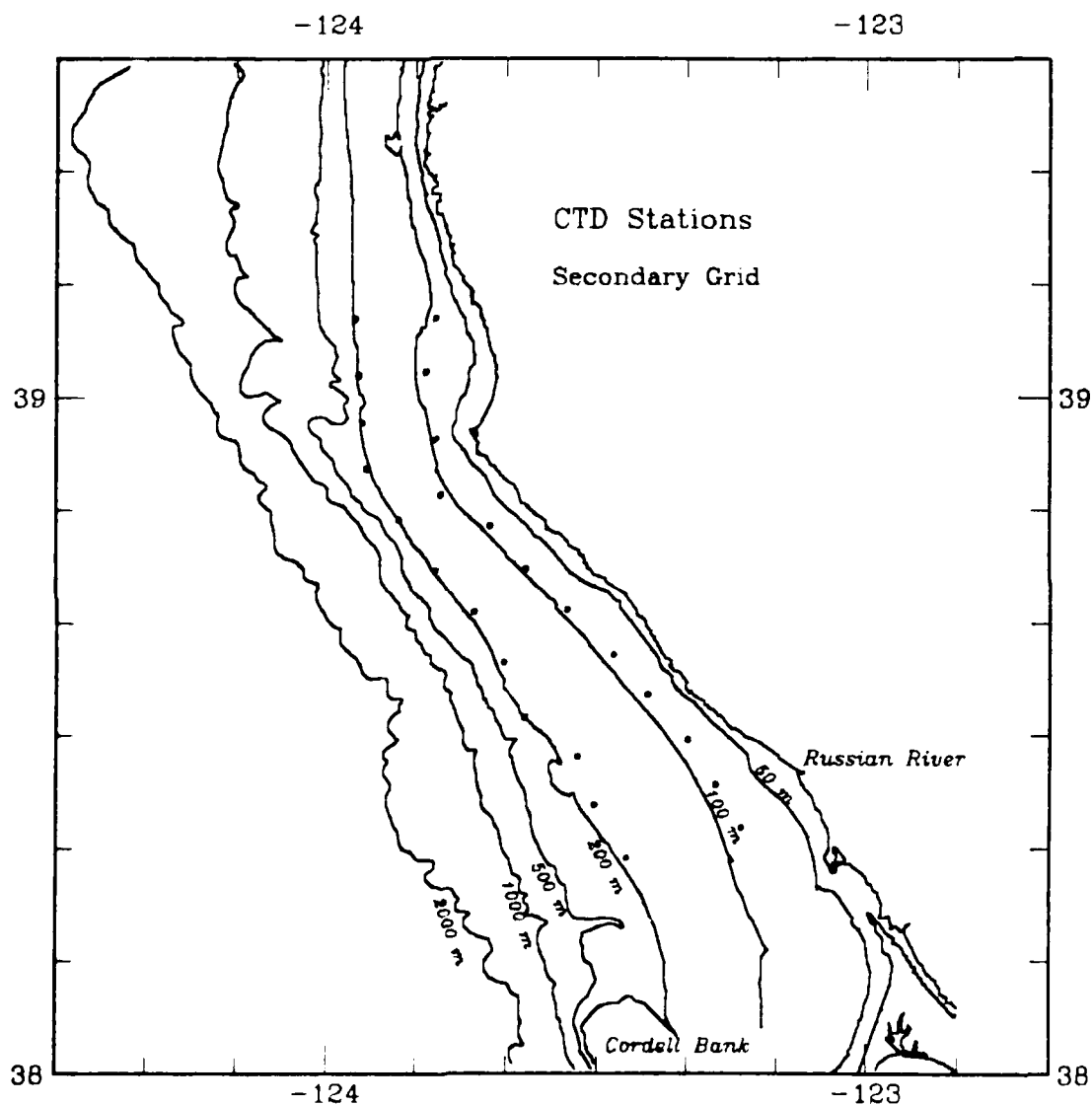


Fig. 6.2b : Secondary grid of CTD stations for CODE. Stations lie along the 50 and 100 fathom isobaths, and are numbered consecutively from northern station. See Appendix for times occupied.

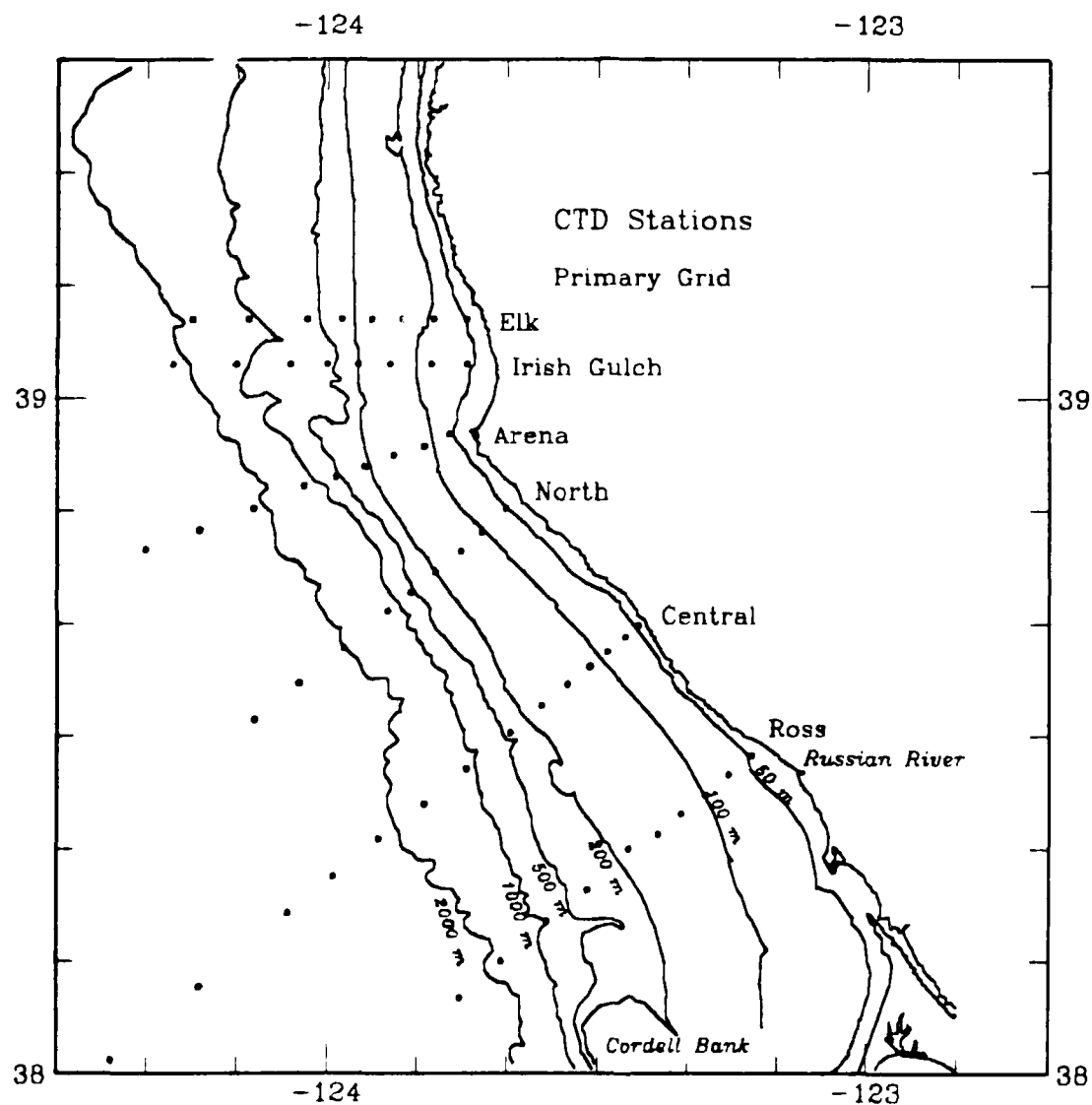


Fig. 6.2a : Primary grid of CTD stations for CODE. Stations on each line are numbered consecutively from station nearest shore. The Irish Gulch line was sampled by CTD only during 1982. The 1982 Central line was some 3 km south of the 1981 line. See Appendix for times occupied.

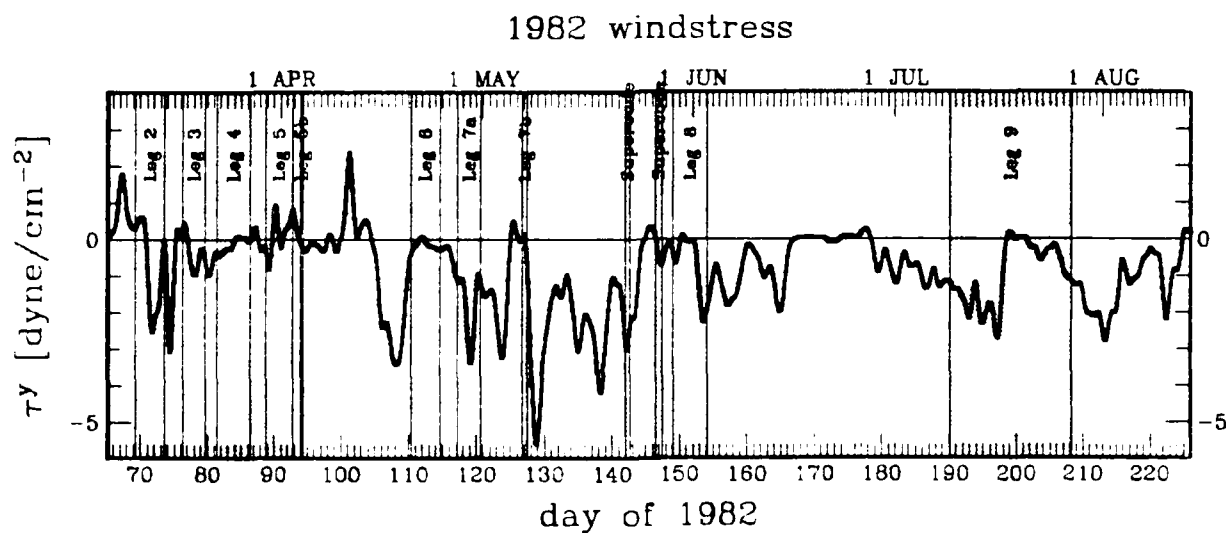
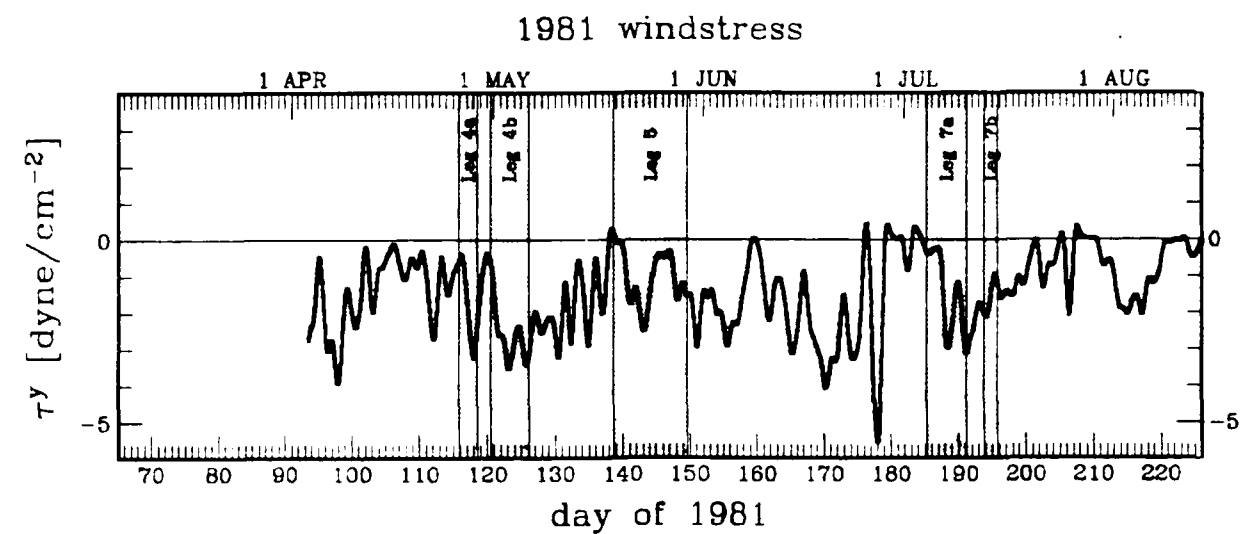


Fig. 6.1 : Alongshore component of surface wind stress (dynes/cm^2) at NDBO 46013, computed from hourly wind measurements. The hourly stress values were low passed using a filter with a 40 hour half power point.

Fig. 6.6 is a map showing a principal axis analysis of current fluctuations about the mean at each CTD station for a depth of 30m. As noted by Kundu and Allen (1976) there is a strong alignment of the principal axes near the coast, while farther from shore the fluctuations approach isotropy and so the principal axes lie along random directions. Over the shelf, the principal axis direction rotates offshore in the same sense as, but somewhat more strongly than, the isobaths. Along the Arena line, representing the flow around a corner, this rotation is especially pronounced and fluctuations quickly become strongest in a direction which is distinctly away from the coast.

6.3. Discussion and Summary

The shipboard current measurements provide a view of the mean circulation which is very well sampled in space, but not continuously sampled in time. It is apparent from Fig. 6.1 that, especially during 1982, sampling may be biased toward periods of low winds. The bias in the mean currents due to shipboard sampling of the wind forcing was estimated at each CTD station from a simple regression analysis of the moored current measurements on the wind stress at NDBO 46013. The predicted bias was small and did not significantly affect the structure of the fields presented above.

The dense spatial sampling provided by the shipboard DAL clearly delineates the extent and intensity of features in the coastal upwelling circulation. As expected, the mean cross-shelf circulation shows an Ekman layer of offshore transport near the surface with return flow below. Out to the shelf break, the layer of offshore flow deepens with distance from the coast. The poleward undercurrent is clearly seen in the mean alongshore current; it appears strongest near the shelf break, and surfaces near the coast. A near surface equatorward jet is apparent in the mean alongshore current across each hydrographic line, but since its core moves offshore from north to south, it is artificially smoothed out when means are calculated as a function of offshore distance alone. The currents show significant divergence in both alongshore and cross-shore components, from which the mean vertical current can be calculated. Mean upwelling appears to occur over the entire shelf, providing enough vertical transport to balance the predicted mean Ekman transport in the CODE region. Fluctuations about the mean current are strongly polarized in the alongshore direction near the coast and essentially isotropic far from the coast. However, flow near the coastal corner at Pt. Arena shows fluctuations polarized away from the coast. Perhaps the most interesting finding of the CODE DAL measurements, however, is that the relative simplicity of the average field does not carry over to the synoptic field, as the mapping surveys discussed in the next chapter show.

for the dynamic height (e.g. Reid and Mantyla, 1976) which are required to infer the geostrophic *current* in shallow water. An example of the limitations of such schemes is given in section 7.4.

Significant divergence $\partial u / \partial x$ is observed in the mean cross-shore current over the shelf (Fig. 6.3f), positive in the upper water column and negative deeper down. In the upper water column over the shelf, the cross-shore divergence averages $3 \cdot 10^{-6} \text{ sec}^{-1}$; this agrees with Davis' (1984b) estimate of surface divergence from drifter measurements. If the divergence in the alongshore current can be neglected, mass conservation and the data in Fig. 6.3f imply that the mean vertical (upwelling) current will be directed toward the surface, with a maximum along the $\partial \bar{u} / \partial x = 0$ contour. Although the DAL data do not reach the surface or the bottom, integration over the data shown suggests a mean upwelling rate at the midwater maximum of at least $0.7 \cdot 10^{-2} \text{ cm sec}^{-1}$ or 6 m day⁻¹, averaged over the inner 15 km of shelf. The implied vertical mass transport over this part of the shelf would be about $10^5 \text{ m}^2 \text{ day}^{-1}$, an amount equal to the offshore Ekman transport forced by a mean surface wind stress of 1 dyne cm^{-2} .

Significant divergence in u is also indicated in the vicinity of the deep maximum in u near the shelf break; whether this result represents true physics or simply an over-optimistic estimate of statistical reliability is not known. The limited evidence from the moored instruments at C5 do show an increase in u in this region.

Averaging over y in the above analysis implicitly assumes that alongshore inhomogeneity in the statistics is unimportant. This is done in order to provide increased density of observations in a broad overall section. Aspects of alongshore variability in the statistics can be examined by comparing the average sections obtained along each CTD line. The sections are shown in Figs. 6.4a,c and the uncertainty, significantly increased over that of the y -averaged section, is shown in Fig. 6.4b. The structure of the mean alongshore current v is considerably more jet-like in these individual sections than in the overall average Fig. 6.3b. From north to south, the core of the jet accelerates and migrates offshore. The latter result is consistent with the fact that the strongest offshore flow appears in Fig. 6.4a to be associated with the core of the jet.

The alongshore structure in the mean field implies a non-zero $\partial v / \partial y$, negative onshore (positive offshore) of the core of the jet, which contributes to the total divergence responsible for the mean upwelling. Because the core of the jet migrates offshore, $\partial v / \partial y$ is a function of the alongshore coordinate y . Rather than attempt a simple y independent representation of $\partial v / \partial y$ to combine with $\partial u / \partial x$ from Fig. 6.3f, $\partial v / \partial y$ was estimated from two pairs of CTD lines and the results shown in Fig. 6.5. The effect of $\partial v / \partial y$ is to substantially increase the inferred maximum w over the shelf and to decrease it beyond the shelf break.

The mean alongshore and cross-shore currents are shown in Fig. 6.3b. Many of the classical features expected for a coastal upwelling flow field (e.g. Allen (1980), Huyer (1983)) can be seen clearly in the average fields. Consistent with the observed equatorward mean wind stress, a near surface layer of offshore transport is evident at all offshore locations in Fig. 6.3b. The thickness of this layer increases from less than 20m near the coast to about 50m near the shelf break. Weak onshore flow occurs everywhere below this layer, except in a region over the shelf near the bottom of the DAL resolution (where the difference from zero is generally not significant according to Fig. 6.3d). It is this pattern of cross-shore circulation which produces the upwelling of cold water near the coast. Near the surface, the alongshore mean flow is characterized by an equatorward jet extending from midshelf to beyond the shelf break. Flowing counter to the equatorward mean wind stress, a poleward undercurrent, strongest near the shelf break, surfaces near the coast.

Fluctuations in u and v about their mean values (Fig. 6.3c) are at least as large as the means themselves. Far from shore, the fluctuations in u and v are equally energetic. As the coast is approached, the fluctuations in u are damped dramatically. These results echo the schematic picture of the upwelling flow field inferred over the past two decades from point current measurements and hydrography (Fig. 1.1).

Cross-shore and vertical gradients in the mean fields were computed by smoothing first differences between adjacent (x,z) bins with a (3×3) triangular weight filter. The results are shown in Figs. 6.3e and f. In the interior, away from surface and bottom stresses, the vertical shear in u is small (generally less than 10^{-2} sec^{-1}). Above 40m, u becomes increasingly sheared as the surface is approached, as expected in the presence of wind forcing. For v , by contrast, substantial vertical shear is evident over a much greater depth range, as expected if the upwelled density surfaces are geostrophically balanced. A rough estimate of the mean geostrophic shear can be made from Huyer's report of the average of 17 post-transition hydrographic sections along the Central line during 1981 (Huyer 1984). Substituting measured isopycnal slopes and $\partial \rho / \partial z$ from Huyer's Fig. 4 into the thermal wind equation

$$\frac{\partial v}{\partial z} = \frac{g}{\rho f} \frac{\partial \rho}{\partial z} \left[\frac{dz}{dx} \right],$$

yields a mean shear of 1.5×10^{-2} as a broad average for depths greater than 50m over the shelf. This is in rough agreement with, though slightly smaller than, the directly measured values. A detailed comparison over paired DAL CTD measurements is indicated, and will be undertaken, to find the small deviations from geostrophy which are of most dynamical interest. Note that such direct comparison of measured and geostrophic shears obviates the need to invoke any of the necessarily *ad hoc* extrapolation schemes

ACOUSTIC MEASUREMENTS OF COASTAL UPWELLING CURRENTS : AVERAGES

6.1. Data

During the spring and summer upwelling seasons of 1981 and 1982, in conjunction with CODEL, some 74 days of current data were collected in the coastal and offshore waters of Northern California using the Doppler Acoustic Log on board the R/V *Wecoma*. The data were collected, for the most part, during normal ship's operation relating to other aspects of CODEL, primarily during the hydrographic surveying cruises. Figure 6.1 shows the periods of Doppler log operation in the CODEL area, together with the alongshore component of the surface wind stress, computed from hourly wind measurements at Coast Guard Buoy NDBO 46013 and 40 hr low-pass filtered (this data was kindly made available by George Halliwell). Figures 6.2 show the CTD stations which comprised the primary and secondary survey grids during Doppler Log operation. The sampling history at each CTD station is shown in the Appendix. Some additional data were obtained in 1982 during mooring deployment and recovery cruises. In order to focus on coastal dynamics during the upwelling season, data obtained prior to the 1982 spring transition (Legs 2-5) were not included in the analysis.

We shall first discuss the averaged measurements, then consider spatial variability in the averages, and conclude in the next section with an examination of the synoptic fields from which the averages are formed. The notation will be standard, with x, y, z, t indicating onshore, upcoast, vertical (positive upwards) and time coordinates respectively. Currents are resolved into cross-shore and alongshore components (u, v) along each primary CTD line, with the alongshore direction being defined as 0° T for the Elk and Irish Gulch lines, 338° T for the Arena line, and 317° T for the North, Central and Ross lines.

6.2. Mean Fields

Figures 6.3 present statistics of the coastal current measurements as functions of offshore distance and depth. The results were obtained by first averaging the data in space-time bins of size $(dx, dy, dz, dt) = (2.5 \text{ km}, 5 \text{ km}, 6.5 \text{ m}, 1 \text{ day})$ centered along each primary CTD line in Fig. 6.2a, then averaging over y and t . The number of observation bins at each (x, z) is shown in Fig. 6.3a. Each bin has been treated as an independent sample (the short time scale was chosen because, in general, resampling of a station after more than 1 but less than 2 or 3 days was not done at random, but by design when wind conditions had shifted significantly).

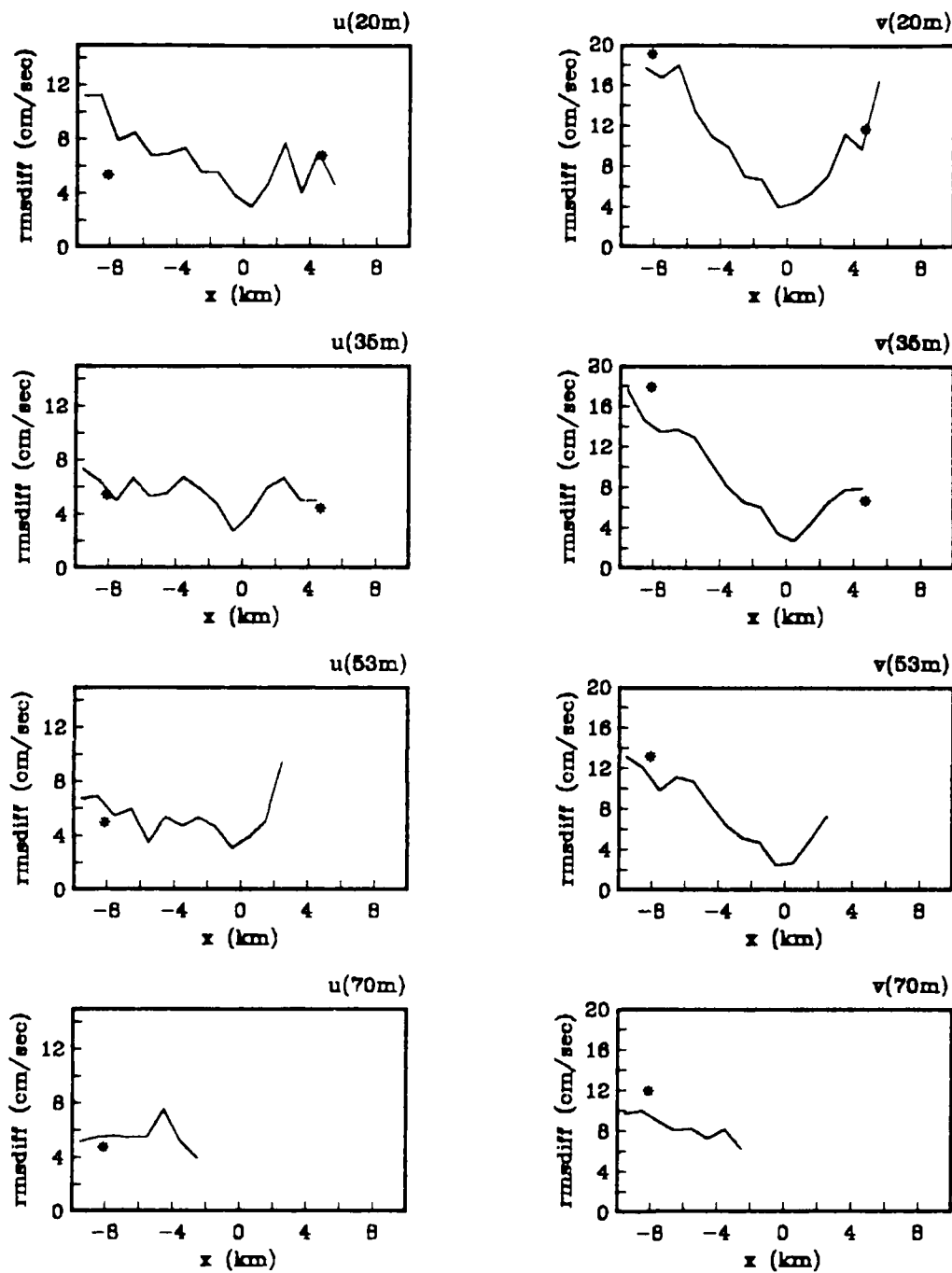


Fig. 5.3c : Root mean square difference between DAL and current meter currents as a function of cross-shelf separation. Stars show C3 rms difference from current meters at C2 and C4.

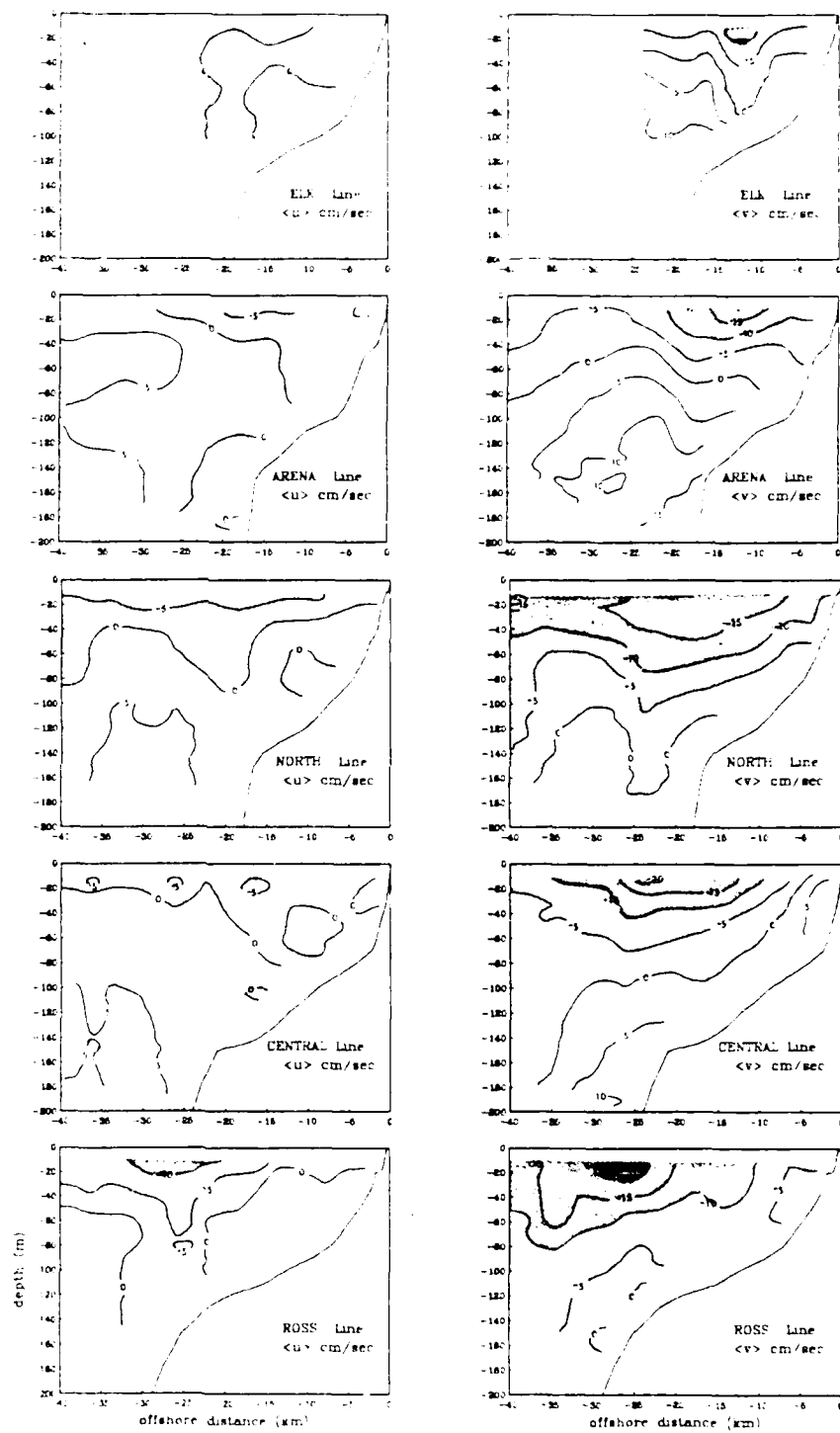


Fig 6.4a : Average $u(x,z)$, $v(x,z)$ along each CTD line. Note the jet in the average alongshore current v , the core of which intensifies and moves offshore from north to south.

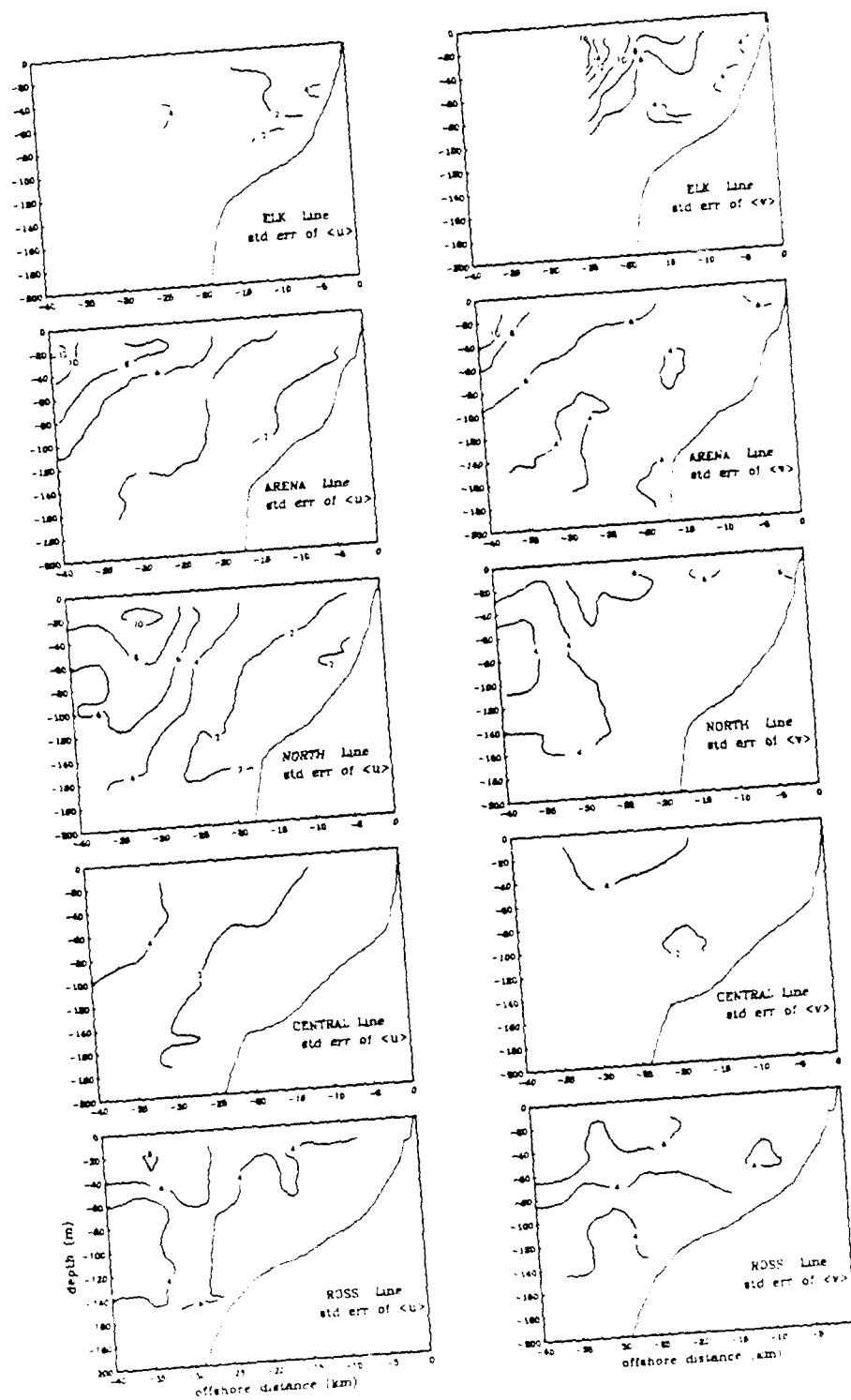


Fig. 6.4b : Standard error of the mean for Fig. 6.4a.

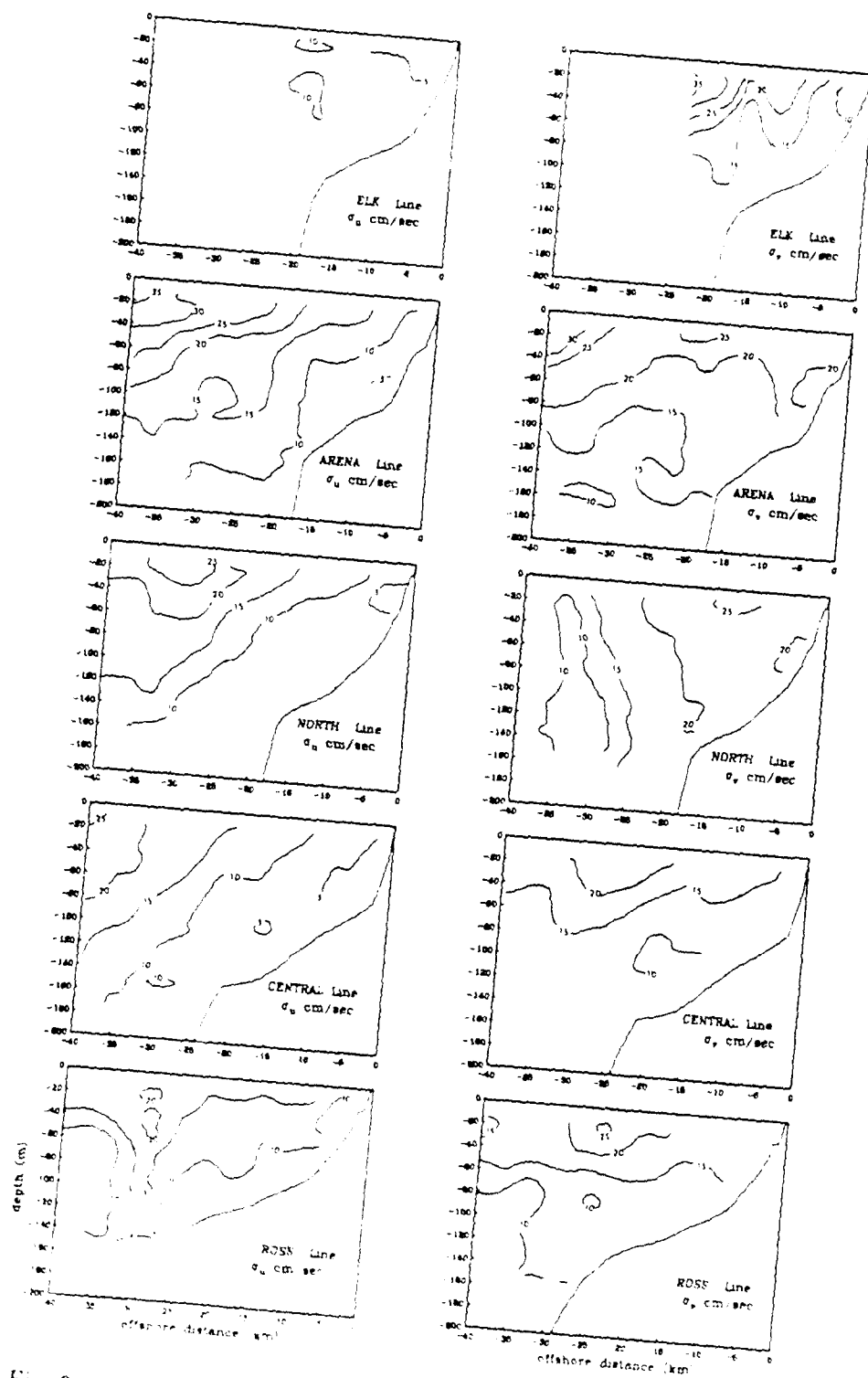


Fig. 6.4c: Standard deviations of u , v about the means in Fig. 6.4a.

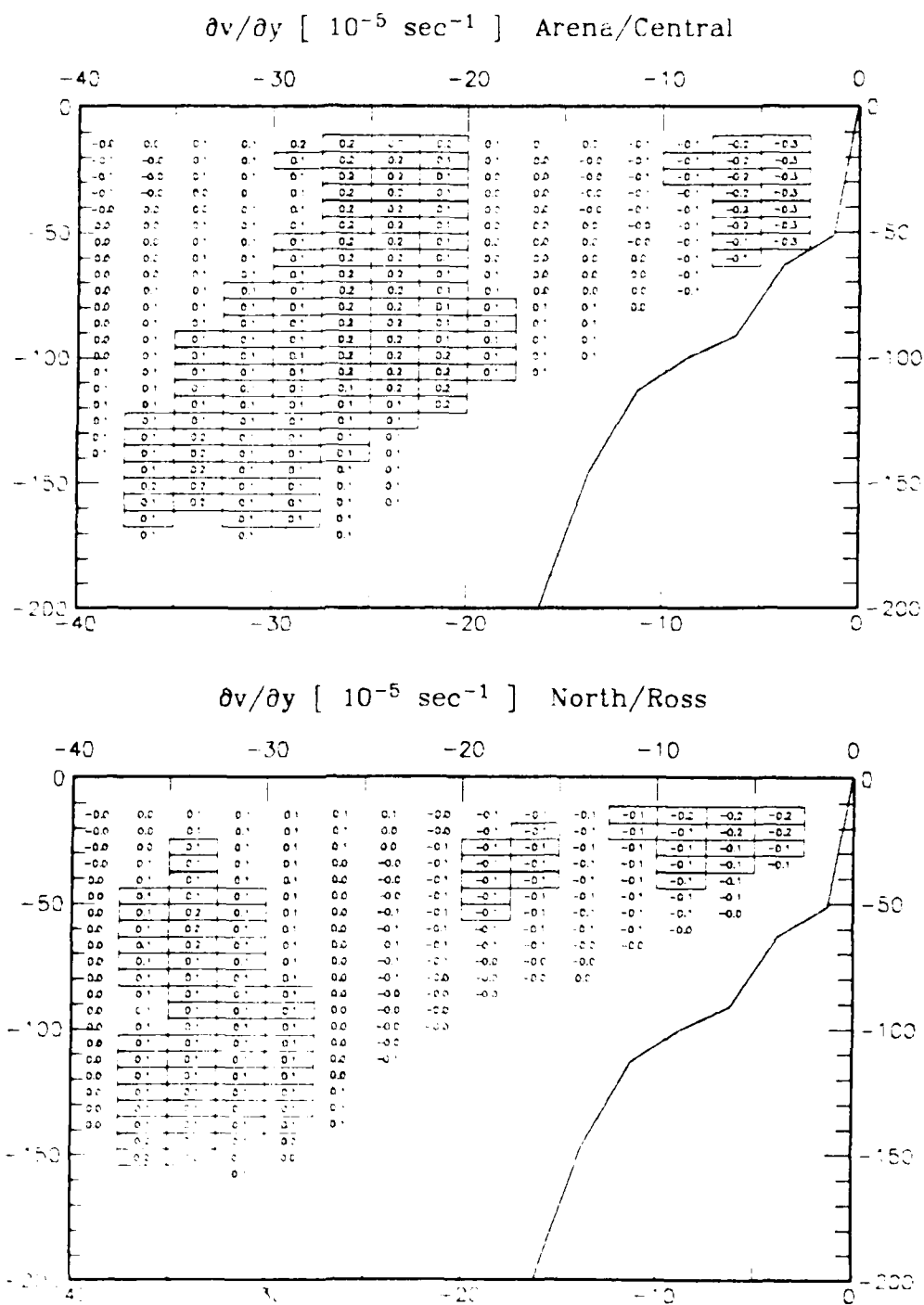


Fig 6.5 Alongshore divergence $\partial v / \partial y$ between pairs of primary CTD lines. Values which were non-zero at the 95% confidence level as discussed in Fig. 6.3f are boxed.

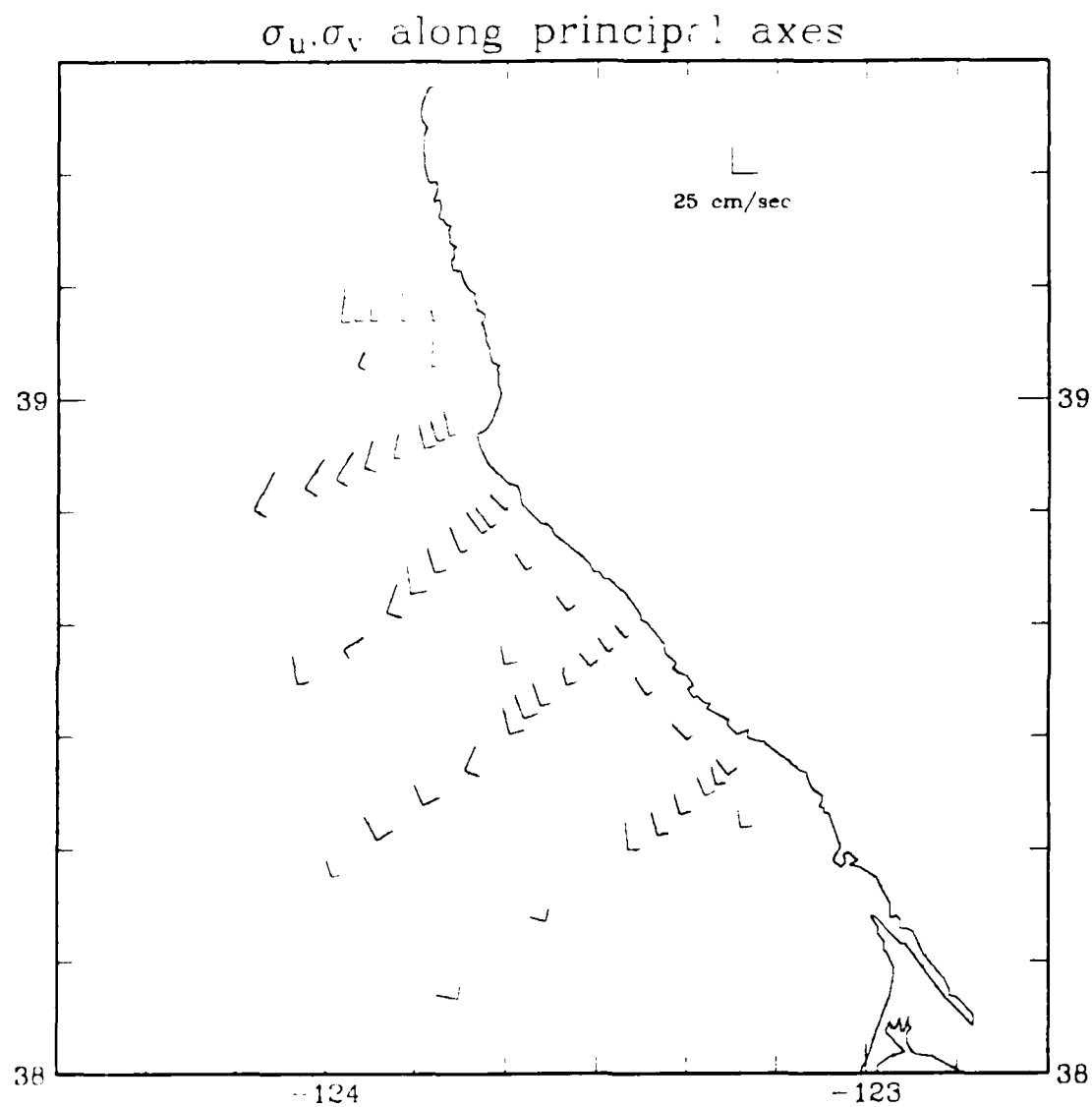


Fig. 6.6 : Principal axes of fluctuations about the mean currents on each CTD station. Where fluctuations are nearly equal, the orientation of the principal axes is random.

Chapter 7

ACOUSTIC MEASUREMENTS OF COASTAL UPWELLING CURRENTS :
SURVEYS**7.1. Introduction**

The preceding description of the average current field is deceptive in its simplicity. The average field is smooth. Fluctuations about the local means, however, are at least as large as the means themselves (Figs. 6.3). The average field is then not necessarily the typical field. In this chapter we shall present maps of currents measured during individual DAL surveys. These maps reveal a high degree of spatial variability in the typical field. Within this generally complex flow field, some features appear to recur. Two of these, the relaxation from strong wind forcing and the tongues of cold water injected from coastal into offshore waters, will be discussed briefly.

7.2. Synopticity

To what extent will maps made from the CODE Doppler data be synoptic? Davis (1984b) has estimated a Lagrangian time scale of 1.5 days for current fluctuations from surface drifter measurements, and points out that this is significantly shorter than the 5 day Eulerian time scale determined from 24-hour filtered current meter measurements, indicating the presence of strong, relatively long-lived structure in the current field. It should be noted that, since the ship travels through spatial structure an order of magnitude faster than do the drifters, the DAL time scale will be much shorter than even the drifter time scale.

To determine the time scales of the energetic patterns of current variability, spatial empirical orthogonal functions (EOFs) were determined from the CODE-2 hourly moored current meter data from 35m depth and the decorrelation times (Davis, 1976) calculated for the time varying amplitudes of each EOF. As expected the more energetic modes have larger spatial scales, while the less energetic modes contain the shorter scale structures. Decorrelation times for the energetic modes were also longer. The first four EOFs explain 79% of the total variance (48%, 19%, 7%, and 6% respectively) and have an energy-weighted decorrelation time scale of 4.8 days (3.5, 9.5, 2.5 and 2.4 days respectively). For the coastal DAL surveys to be shown, the average time separating pairs of measurements, $\tau = (t_2 - t_1)/2$, ranges from less than 1.8 to about 1.4 of this decorrelation time. Thus although the DAL surveys are not a snapshot, the features seen are much more indicative of spatial structure than temporal variability.

7.3. DAL Atlas

In Figs. 7.1 to 7.11 we present an atlas of the phenomena observed in the coastal current field during the shipboard mapping effort of CODE. The current measurements come from a depth of 28m. For clarity, measurements separated by less than a minimum distance (typically 3 km) have been averaged. The currents have been overlaid on satellite IR images of sea surface temperature whenever relatively cloud-free images, close enough in time to the ship surveys, were available from the Scripps Remote Sensing Facility. Each image contains a legend showing the dates of both the satellite image and ship survey. Tic marks have been placed every half degree of latitude and longitude, and a scale vector for the currents is shown. The length of any current arrow corresponds to the displacement by that current over a 4.6 hour period (9.3 hours for the 2 large surveys). Fig. 6.2 can be overlaid on each image to relate the features seen to the bathymetry. Fig. 6.1 can be used to gauge the wind forcing during each survey. The hydrographic measurements taken during each survey are described in a series of Data Reports by Huyer and co-workers (OSU Reference series).

The satellite IR shows that sea surface temperature varies strongly in both the alongshore and cross-shore direction. Although such alongshore variability has long been noted in satellite images (Bernstein, *et al.* 1972), its relevance as an indicator of coastal circulation and exchange processes has remained in doubt. Without *in situ* measurements, the depth extent of the features and strength of the associated circulation was unclear.

The DAL current measurements exhibit a strong visual correspondence with the satellite derived surface temperature field. Where this is true, the features in the satellite images cannot simply be dismissed as skin effects on the sea surface. Rather, the cold water upwelled near the coast acts as dye, tracing features in the flow field.

The atlas conveys a much different impression of the upwelling circulation than that obtained from the mean field measurements discussed in Chapter 6. The mean field showed offshore flow occurring in a surface Ekman layer at velocities of order 10 cm sec or less. The synoptic maps, however, reveal greatly enhanced offshore flow occurring in narrow bands along the coast. Also observed in drifter records from the same period, Davis (1984a) has dubbed these features "squirts". On 27 April 1981 (Fig. 7.1), a 15 km wide squirt is seen centered 25 km south of Pt. Arena. Cold water dyes a portion of this squirt, but both the DAL thermistor record and the satellite image show that the squirt is somewhat wider than the cold tongue. Compensating onshore flow at depth does not occur within the DAL range of 150m; this flow is truly three-dimensional. To the north and south of the squirt, warm surface water accompanies shoreward flow. Another squirt carrying upwelled water seaward crosses the Ross line in the south (cf. Fig. 6.2a). Despite generally strong wind forcing, alongshore currents are weak, and the

coastal jet, which dominates the mean flow, is absent.

A week later, the region was resurveyed (Fig. 7.2) during a period of strong wind forcing. A much more classical flow is observed in this survey, with currents polarized alongshore over most of the shelf. However, off Pt. Arena the currents turn seaward, again carrying upwelled water away from the coast. Surface drifters deployed in a line off Pt. Arena dramatically echo this observation (see Fig. 5 in Davis (1984a)). Nearly 100 km from shore, strong narrow currents can be seen deforming the temperature field in the southern portion of the survey.

Fig. 7.3 makes it clear that energetic eddies centered over the continental slope can reach onto the shelf and deform the temperature field, sweeping upwelled water from the shelf and even recirculating it back again. This survey appears to show a counter-rotating eddy pair, joined along Pt. Arena. The strong on/offshore currents from these eddies were still apparent when the area was resurveyed (Fig. 7.4).

Figs. 7.7 through 7.11 chronicle the development of the temperature and current fields over a two week period in mid-July 1982. The winds varied greatly at NDBO 46013 during this period (Fig. 6.1) and shipboard winds (Huyer, *et al* 1984) show strong variability during the course of each survey. Even so, strong features are observed in the currents, measured over several days, which correspond well to features in the sea surface temperature, measured in minutes by the satellite. Two cold tongues are observed in the images of 9-15 July 1982. The northern tongue is swept out to sea along the southern edge of a strongly sheared current feature which hugs the coast north of Pt. Arena. The southern tongue exhibits weaker flow along its axis and weaker shear across it. By the last survey (Fig. 7.11), the southern tongue, and the currents associated with it, have disappeared. The development of a cyclonic eddy between the two cold tongues can be seen in the IR and also in the current measurements of Figs. 7.10 and 7.11. This eddy, centered over the continental slope, dominates the dynamic topography during the 16-19 July survey (Huyer, *et al.* 1984), and one surface drifter was trapped by the eddy for nearly 8 days, completing 3 circuits around its core.

In summary, the maps show a current field which varies strongly in both x and y , and which only rarely resembles the smooth average field described in Section 6.2. Instead of occurring in a simple surface Ekman layer, significant offshore transport of cold coastal water is seen in very active regions of short horizontal scale. A jet in the alongshore current, the most prominent feature seen in the mean field, is seen only occasionally in the individual maps. Strong current fluctuations from the mean field are present at a wide range of scales, and coherent eddy-like structures centered beyond the shelf break carry water upwelled at the coast far out to sea.

Two striking features of the DAL maps deserve discussion.

7.4. Wind Relaxation of April 1982

The survey from Leg 6 of CODEL 2 affords a well defined example of a relaxation of the current field on cessation of strong upwelling favorable wind forcing. Following sustained equatorward winds which commenced on 14 April 1982 and apparently triggered the spring transition (Huyer, Sobey and Smith 1979) to the upwelling dynamical regime in the CODEL region (Lentz and Winant, in preparation), the winds over the entire CODEL 2 array calmed dramatically on 19 April, and remained calm until 25 April. The coastal current field was mapped by shipboard DAL during 20-24 April. The satellite image from this period (Figs. 7.5 and 7.6 in the atlas) shows a wedge of warm surface water close to the coast, with cooler water lying offshore. Simultaneous hydrographic measurements (Fleischbein, Gilbert and Huyer 1983) show that the warm surface water is accompanied very close to shore by a thin layer of low salinity. The Russian River, flowing at an average rate of $105 \text{ m}^3 \text{ sec}^{-1}$ during this period (Markham *et al.*, 1984) is a possible source for the fresh water, but is probably too small to explain the extent of the anomalously warm water.

The observed flow field is remarkable (Figs. 7.5 and 7.6). Near the coast, strong poleward flow is associated with the band of warm water. This flow occurs in the absence of any significant wind forcing. Further offshore, a strong equatorward jet is present. Unlike the other realizations of the flow field shown in the atlas, this flow is strongly polarized in the alongshore direction. The depth structure of the alongshore flow across a series of CTD transects covering a 36 hour period is shown in Fig 7.12, displayed from north to south. Nearshore poleward flow is observed in each transect, albeit strongly reduced at the Irish Gulch Line north of Pt. Arena. The observed cyclonic horizontal shear is strongest along the Arena Line, where $\partial v / \partial x$ is somewhat larger than the Coriolis parameter f . The observed vertical shear structure is interesting. The poleward flow is relatively barotropic, while the offshore zone shows strong vertical shear of $\sim 10^{-2} \text{ sec}^{-1}$ and more. This suggests that the nearshore zone is barotropically forced, as by an alongshore sea level gradient. The barotropic component of the flow can not be determined hydrographically. As a result, the surface dynamic height maps from this period fail to detect the poleward flow near the coast (Fleischbein, Gilbert and Huyer 1983).

The persistence of the strong structures discussed here is also noteworthy. During this cruise, the Central line was surveyed 4 times. Fig 7.13, which shows offshore profiles of the alongshore current at 28m depth for each survey, shows that the cross-shelf profile of v changed very little in more than 3 days within 20 km. of the coast; beyond 25 km offshore, the equatorward jet in v apparently sharpened somewhat

between the second and third surveys. Sections from each survey, Fig 7.14, are also relatively unchanged over 3 days, except for some weakening of the field seen in the last survey. Any theory which seeks to account for these relaxation events must explain this long decay time.

An interesting footnote to this discussion concerns the near-surface shear field during relaxation events (Fig 7.15). Prior to the spring transition, the near surface shear field shows strong amplitude fluctuations at diurnal and higher frequencies. For most of the post-transition data, these fluctuations are strongly damped. During periods of wind relaxation, however, the usually well mixed surface layer of water restratifies, allowing near surface shears to be supported, and the amplitude of the shears increases dramatically. For C3, the restratification occurs not only in temperature (Fig 7.15) but also in salinity, as can be seen from the hydrographic data (Fleischbein, Gilbert and Huyer 1983). So, for this site, advection possibly supplemented by local surface heating form a strong surface signature in the density field during relaxation events. When this density structure is present, strong vertical shears can be supported, and are observed, near the surface. Strong near-surface vertical shear is usually associated with strong wind forcing, not with its absence. The energy is concentrated in motions with diurnal and semi-diurnal periods, suggesting tidal forcing.

Examination of features seen during relaxation events has provided insight into aspects of the momentum balance. In the next section, we shall examine features which may have importance to the ways in which mass, heat, salt and nutrients are exchanged between coastal and offshore waters.

7.5. Jet Surveys, July 1981 and July 1982

The features in the CODE measurements which have drawn the most interest are the prominent tongues of cold water, a particularly active example of which is shown in Fig. 7.16. First observed in satellite imagery (Bernstein, *et al.* 1972, Breaker and Gilland 1981, Traganza *et al.* 1981, Kelly 1983), these features can extend from the coastal upwelling zone to several hundred kilometers offshore. In the example shown, at least 4 strong cold-water bands are seen in the 800 km stretch of coastline from Cape Mendocino to Pt. Conception. The potential importance of these structures to the cross-shore mass and heat balances has been noted by Davis (1984b). If these modes of property transport are significant, their transient nature and strong spatial variability imply that an understanding of such balances based on moored data alone will be difficult, at best.

The earliest findings in the first weeks of CODE with both DAL (Figs. 7.1-7.4) and surface drifters (Davis, 1983) were that unexpectedly large cross-shelf currents on narrow scales were associated with the cold water zones observed in the satellite images of Kelly (1982). As a result, we undertook DAL and hydrographic surveys of the cold

water features in July of 1981 and again in July 1982. Contributions to the 1981 survey were made by Jane Huyer and Martin Olivera of OSU (hydrography), and supplementary information useful in cruise planning and later analysis were provided by Kathryn Kelly of SIO (satellite image and analysis) and Larry Breaker of NESS (satellite analysis). The 1982 survey drew on the resources of Jane Huyer (hydrography), and Pierre Flament, Libe Washburn and Larry Armi of SIO (underway thermosalinograph, tow-yo CTD measurements, and shore to ship transmission of satellite images). Although the latter group's primary interest was in small scale mixing processes at the boundaries of these cold water structures, their satellite images and underway data allowed much more effective planning of survey strategies for, and scientific understanding of, the mesoscale structures which were the primary interest of the DAL and hydrographic groups.

Maps of the currents at 28m depth from the two surveys, the first conducted on 4-10 July 1981, the second on 22-26 July 1982, are shown in Figs. 7.17 and 7.18. Both surveys show a tongue of cold water riding on very swift (up to 75 cm sec) offshore currents from their apparent points of origin in the coastal upwelling zone, extending over 250 km out to sea. Within the broad (0/75 km wide) tongues of cold water, a narrow (0/5 km wide) band of even colder water lies toward the northern edge. Some evidence of recirculation back toward the coast in the southern diffuse portion of the tongue is seen in the 1981 survey. Flament (personal communication) has noted this recirculation in sequences of satellite images for the 1982 survey; unfortunately in 1982 our *in situ* measurements did not extend far enough south to sample this region.

The survey of 22-26 July 1982 was the more successful at obtaining sections of oceanic variability across the cold tongue, primarily because of the shipboard availability of satellite images from as late as 22 July 2300 UT. By the time the survey was conducted, clouds had obscured the area, and the detailed structure of the field had altered, but the data from the surface thermosalinograph allowed the actual locations of features in the survey to be identified.

The ship track for the 1982 survey, annotated with the day of the year and time (UT), is shown in Fig. 7.19 (a gap in the DAL data occurred on 24 July (day 205) from 1450-1911 UT). Some eleven crossings were made of the thin band of coldest water at the northern edge of the cold tongue. When the underway thermosalinograph data from this period is plotted as a T-S diagram (Fig. 7.20), a strong separation of T-S behavior across the cold tongue is found. The left branch of the curve, made up of samples within and north of the coldest ribbon of water, represents relatively fresh water whose salinity varies little over a temperature range of nearly 3°C. The right hand branch has higher salinity and lies south of the coldest ribbon. From CTD sample on stations in the 1981 survey, Olivera (1982) also postulates a separation of surface water types, and

attributes the northern, fresher water mass to a diluted remnant of Columbia River plume.

In order to resolve the DAL currents into sections showing their structure with depth and position, a coordinate system must be chosen. The choice is not obvious, however, since the jet changes its orientation at each crossing. I have adopted acrossjet/alongjet coordinates (x, y) with currents (u, v) defined to lie across/along the direction of mass transport measured with the DAL across each transect. Sections were then plotted as functions of the acrossjet coordinate x . Because the jet always points offshore, the northern, low salinity water is always at high x ; the origin of x is arbitrary. For each section, currents were averaged over bins of 5 km in x . The alongjet currents have been contoured at 10 cm/sec intervals; the acrossjet currents are shown as arrows using a scale of 5 km in x for 50 cm/sec in u . Shown above each section are the concurrent T , S , and density (as σ_t) at 5 m depth from the underway thermosalinograph.

At each crossing, a surface intensified jet in v is observed, with peak currents ranging from over 70 cm/sec to less than 40 cm/sec. Within the jet, the alongjet flow is 20 cm/sec or more to at least 100 m depth. The jet appears to achieve its maximum velocity not at the sharp temperature front where the coldest water is found, but only after the temperature begins to rise again at larger x , i. e., within the northern water mass. The data show that the dramatic temperature front seen in the satellite images is strongly salinity compensated, so that surface density changes little across it, while the slow rise in surface temperature north of the front is accompanied by fairly constant salinity, resulting in a gentle density gradient. This density gradient will in turn be accompanied by a rise in geostrophic alongjet current. Thus, at least near the surface, the salinity structure contributes independently to the density field, and estimates of geostrophic flow based on temperature measurements alone will be in error.

Within the DAL field of view, the measured alongjet transport varies from 0.7 to 2.3 Sv ($1 \text{ Sv} = 10^6 \text{ m}^3 \text{ sec}^{-1}$), with an average of 1.5 Sv over complete transects. This will be an underestimate of the mass transport since, in many cases, the measurements did not reach deep enough nor far enough north to define the boundaries of the flow. Nonetheless, this represents a stunning amount of water flowing offshore. For comparison, the offshore Ekman transport resulting from a surface windstress τ of 1 dyne cm^{-2} is $\tau/\rho f = 1 \text{ m}^2 \text{ sec}^{-1}$. If this transport were to be provided by a convergence of Ekman transport from the coastal zone, it would require gathering all the Ekman transport generated by a 1.5 dyne cm^{-2} wind over 1000 km of coastline. Clearly the bulk of the water travelling offshore is not being provided by simple convergence of water upwelled at the coast. Moreover, any flow initially restricted to the shelf would have to be prodigious indeed to supply this much mass: the total diversion of a current averaging 75 cm/sec over the entire breadth and depth of a 20 km wide shelf 100m deep would be

required to produce such a transport. The implication is that such features must receive significant contributions from flows located off the continental shelf, such as eddies in the deeper ocean.

Finally, a word about geostrophy and the cold tongues. The use of hydrographic data to infer currents by assuming a geostrophic balance of forces is a common place. However flows for which relative vorticity terms are large will not be in simple geostrophic balance. Joyce and Stancup (1984) show the importance of cyclostrophic terms to the balance of forces in a Gulf Stream warm core ring. Similar considerations apply to the convoluted flow fields accompanying the cold tongues which we have been discussing. For the 1981 survey, the cold water leaving the coastal upwelling zone circulates anticyclonically around a warm feature off Pt. Arena. Assuming the circulation is centered around $38^{\circ}15'N$, $124^{\circ}3'W$, the relative vorticity is found to be approximately $-0.4f$, so that the total vorticity is only 60% of its value in the absence of relative vorticity. With effectively less total rotation, a given density gradient requires a larger vertical shear to remain in equilibrium. Thus currents estimated using geostrophic balance will substantially underestimate the actual current magnitudes. On the other hand, flows with strong cyclonic relative vorticity will be overestimated by the assumption of geostrophy.



Fig. 7.1. DAI currents at depth of 28m, obtained during a survey from 26 April 0045 to 28 April 1400, 1981 (all times are L.T.), plotted over a NOAA6 IR image from 27 April 1611. The marks every 30 minutes of latitude and longitude (56 and 41 km, respectively) and a scale vector for the currents are shown. Pt. Arena (38° 57' N, 123° 44' W) serves as a landmark. Lighter shades correspond to colder water. For clarity of presentation all measurements within a 3 km radius have been averaged. Note the concentrated zones of flow in which cold water upwelled at the coast is carried offshore. Such flow structures may make significant contributions to the property transport budgets of the coastal zone.

AD-A157 040

SHIPBOARD ACOUSTIC CURRENT PROFILING DURING THE COASTAL
OCEAN DYNAMICS EXPERIMENT(U) SCRIPPS INSTITUTION OF
OCEANOGRAPHY LA JOLLA CA P M KOSRO MAY 85 SIO-REF-85-8
N00014-80-C-0440

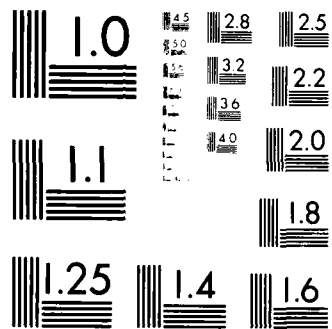
2/2

UNCLASSIFIED

F/G 17/1

NL





MICROCOPY RESOLUTION TEST CHART
 U.S. GOVERNMENT PRINTING OFFICE: 1963-O



Fig. 7.2 - Same as Fig. 7.1, except for ship survey of 2 May 1800 to 6 May 0330, 1981 and NOAA6 image from 6 May 0345. Survey was made during a period of sustained strong equatorward winds (Fig. 6.1). Compare with Davis' Fig. 5 (1984a).



Fig. 7.3 : Ship survey from 18 May 1600 to 22 May 0300, 1981. NOAA6 image from 20 May 1550.

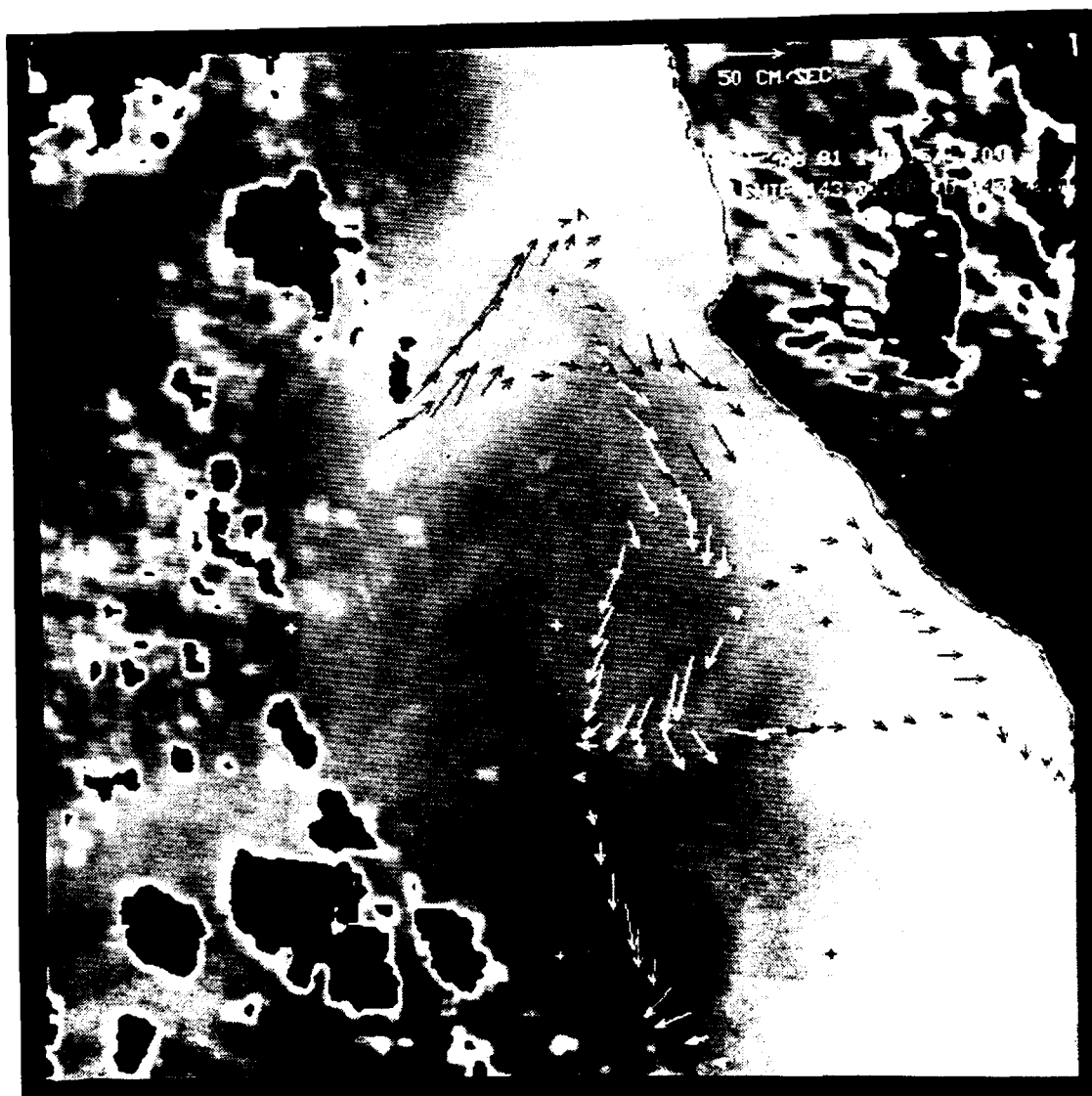


Fig. 7.4 : Ship survey from 23 May 0100 to 25 May 0600, 1981. NOAA6 image from 20 May 1550 (same as Fig. 7.3).



Fig. 7.5 : Ship survey from 20 April 1600 to 22 April 1200, 1982. NOAA7 image from 24 April 2210 (note delay from survey time). This flow occurred during a cessation of winds following a period of strong southward wind forcing, and is discussed in Section 7.3.



Fig. 7.6 : Ship survey from 22 April 1400 to 24 April 1130, 1982. NOAA7 image from 24 April 2210 (same as Fig 7.5).

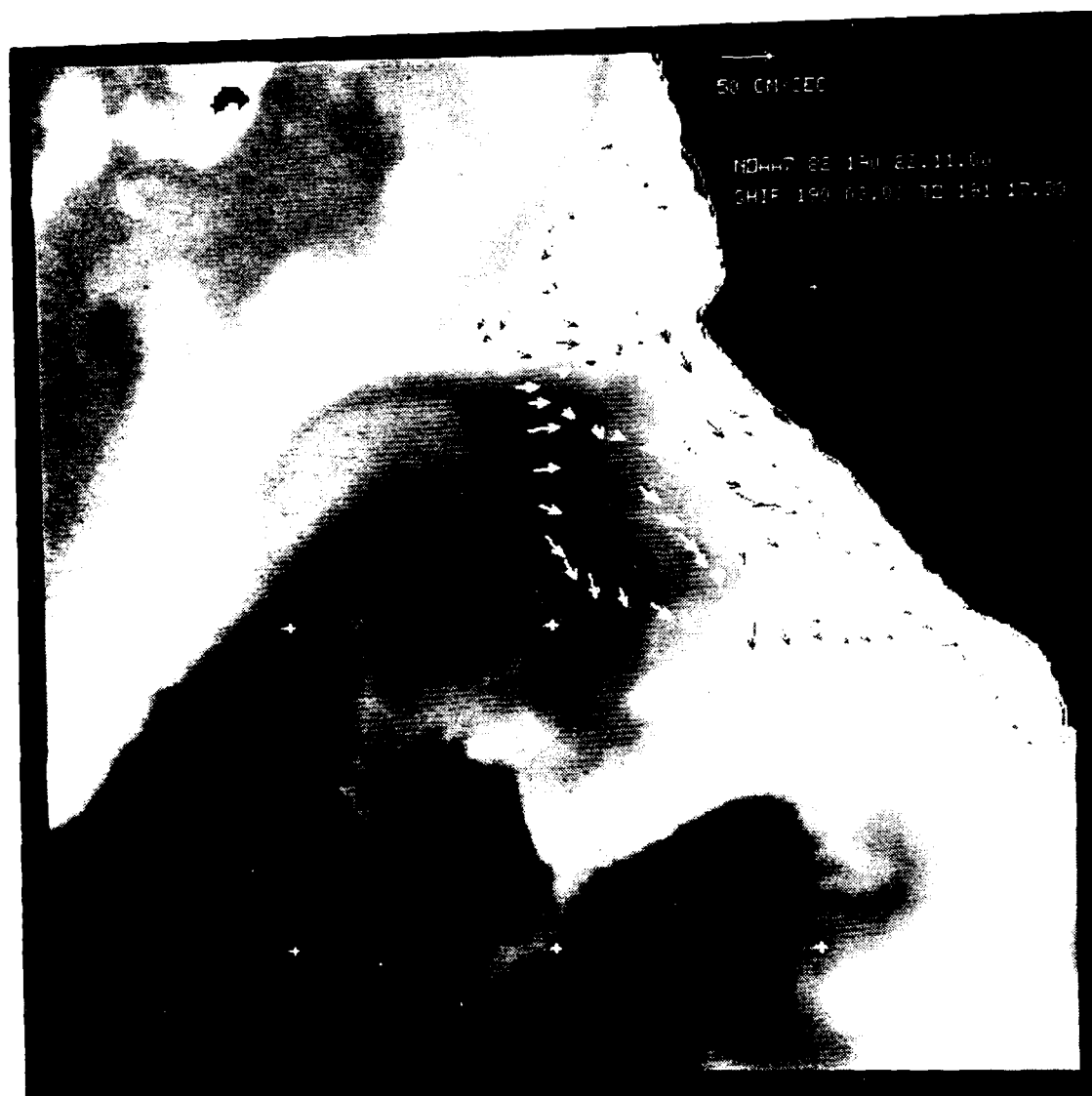


Fig. 7.7 : Ship survey from 9 July 0300 to 10 July 1730, 1982. NOAA7 image from 9 July 2211.



Fig. 7.8 : Ship survey from 11 July 1100 to 13 July 1400, 1982. NOAA7 image from 9 July 2211 (same as Fig. 7.7).



Fig. 7.9 : Ship survey from 14 July 1400 to 16 July 0920, 1982. NOAA7 image from 14 July 2254. Wind forcing was very strong and increasing during the survey period. Note the strong current magnitudes and shears across the northern transects.

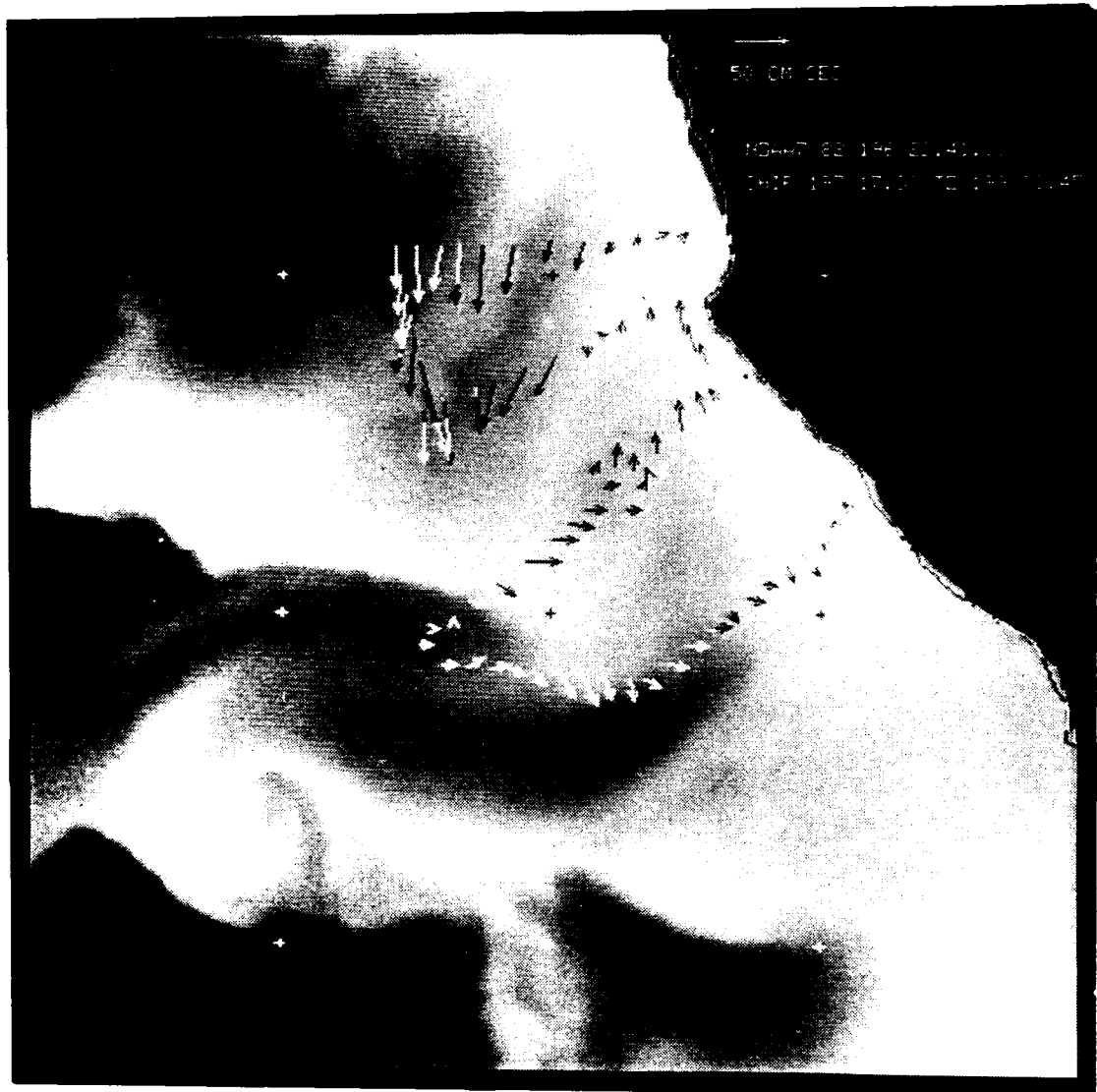


Fig. 7.10 : Ship survey from 16 July 1730 to 18 July 0845, 1982. NOAA7 image from 15 July 2241. Survey was performed from south to north: winds were strong to moderate along the Central and North lines, but had calmed to airs during the surveys of the Arena and Irish Gulch lines. Northward flow at the inshore ends of the CTD lines is seen, although the flow at the offshore end of the two northern lines remains strong and strongly sheared. Note the developing eddy along the North line.

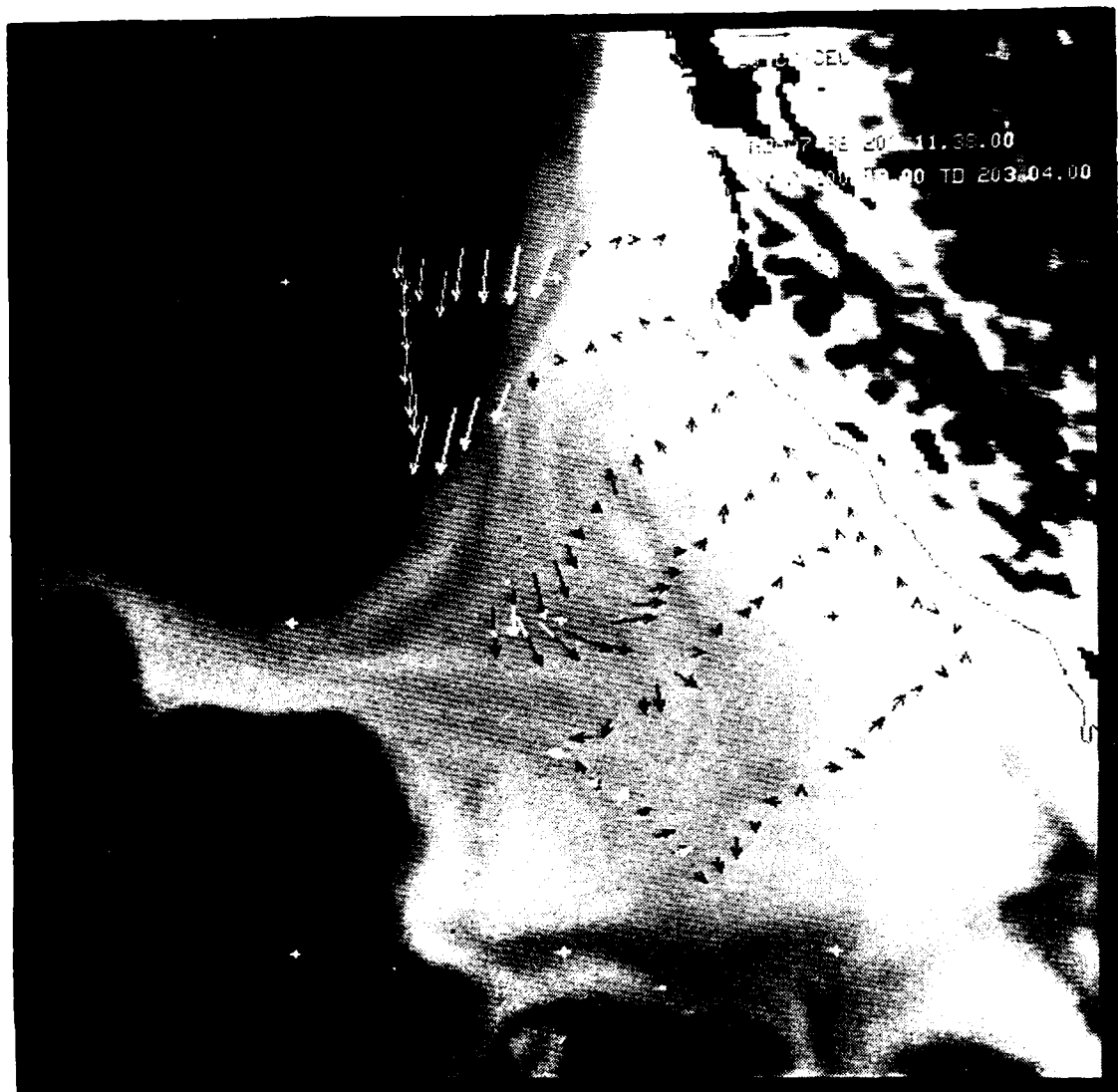
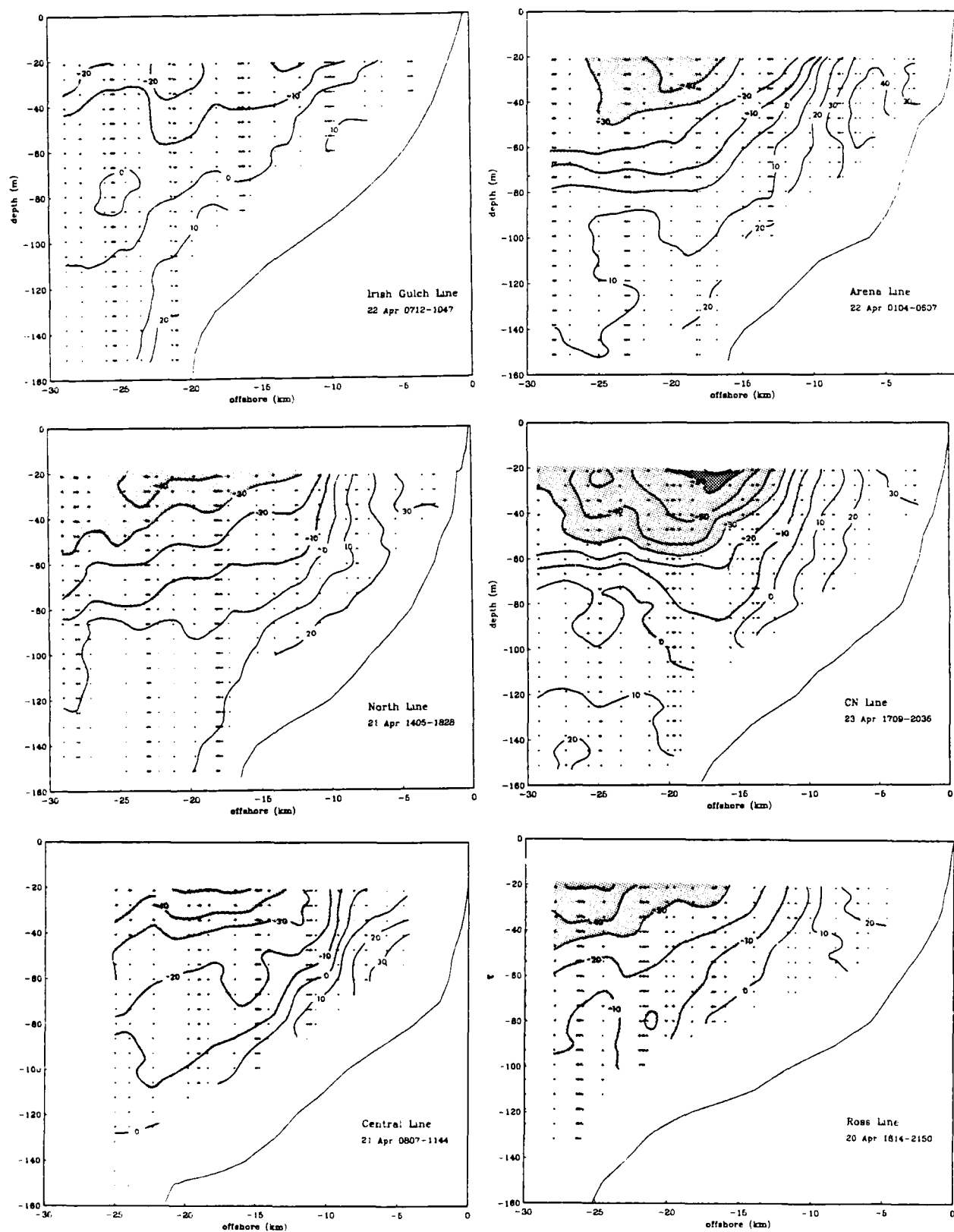


Fig. 7.11 : Ship survey from 19 July 1900 to 22 July 0400, 1982. NOAA7 image from 22 July 2259. Winds were calm during the survey of southern 3 lines, but were moderate to strong along the northern 3 lines. The eddy along the North line has developed strongly. Davis (1983) shows tracks of surface drifters which circulated in this eddy for a week and more, making several circuits.



Figs. 7.12 : Cross-shelf sections of alongshore current with depth during the wind relaxation of April 1982. Sections are from the five primary CTD lines, plus a CN line midway between the Central and North lines. Plusses show location of measurements. Contour interval is 10 cm/sec. Equatorward currents are shaded.

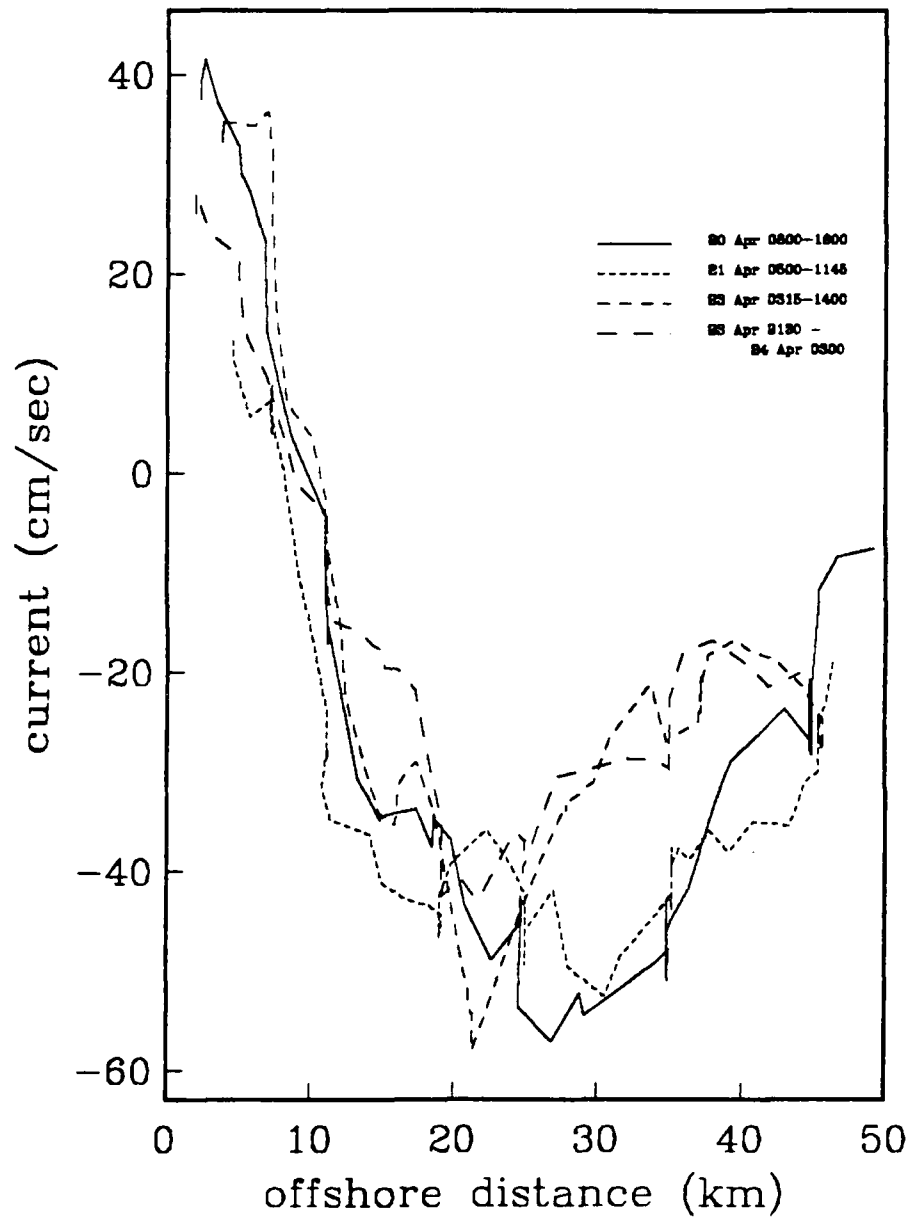


Fig. 7.13 : Alongshore current $v(x)$ at 28m for the 4 Central line occupations from 20-24 April.

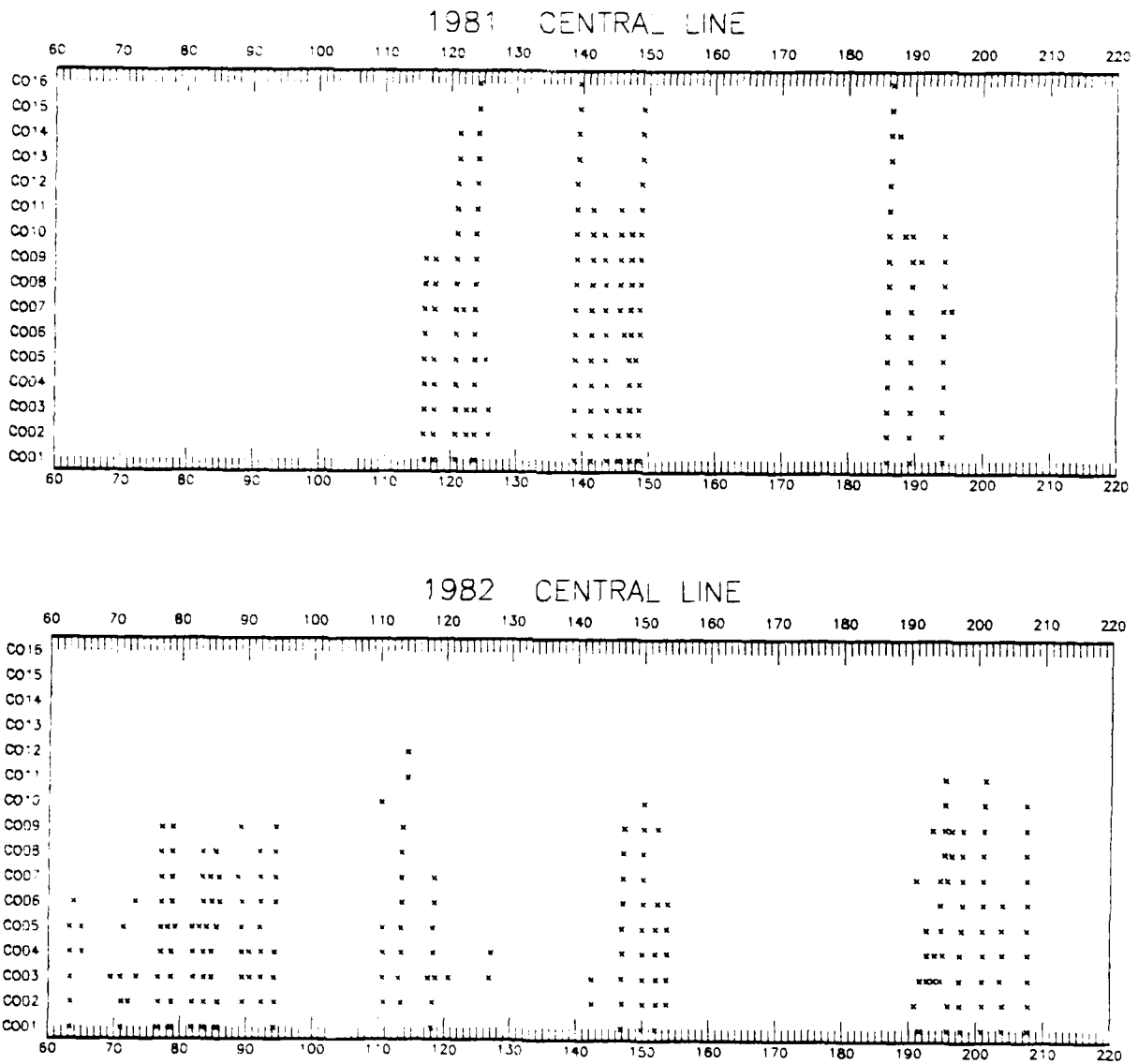


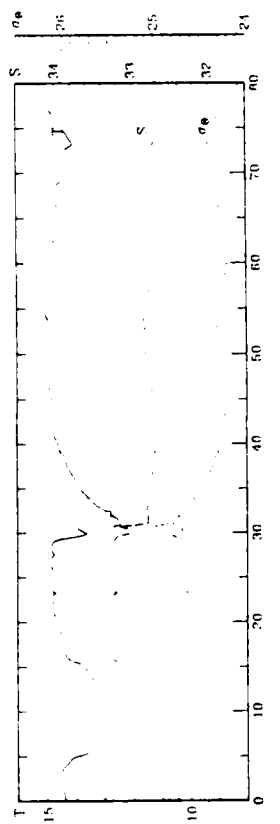
Fig. A.1 : Central Line occupations vs. day of year.

Appendix

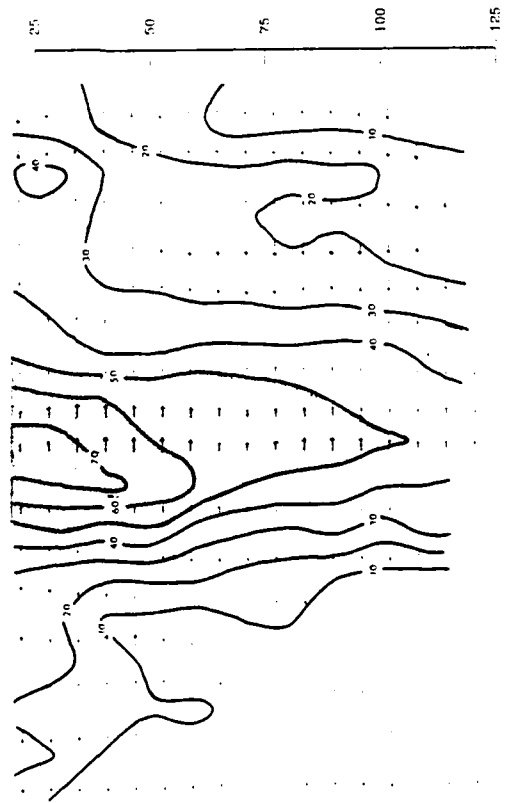
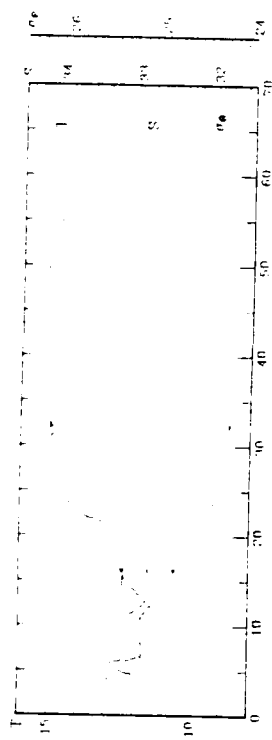
DAL SAMPLING AT HYDROGRAPHIC STATIONS

This appendix shows the times (day of the year) at which DAL data were collected at each hydrographic station shown in Fig. 6.1. Occupations separated by less than 1 day are not shown.

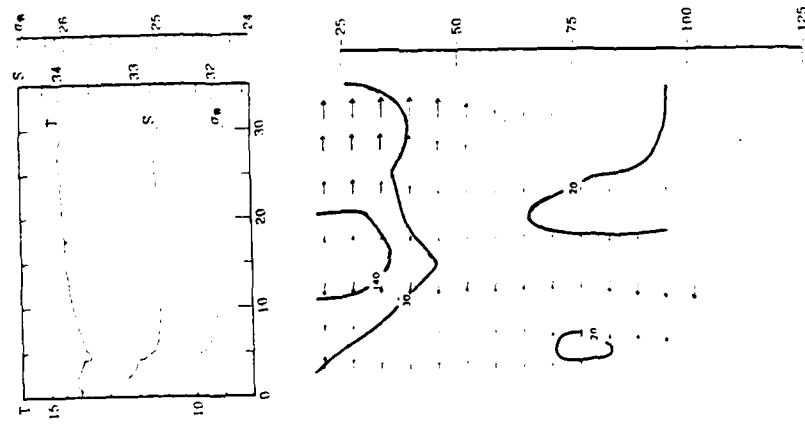
TRANSECT FROM 206/0130 TO 206/1200



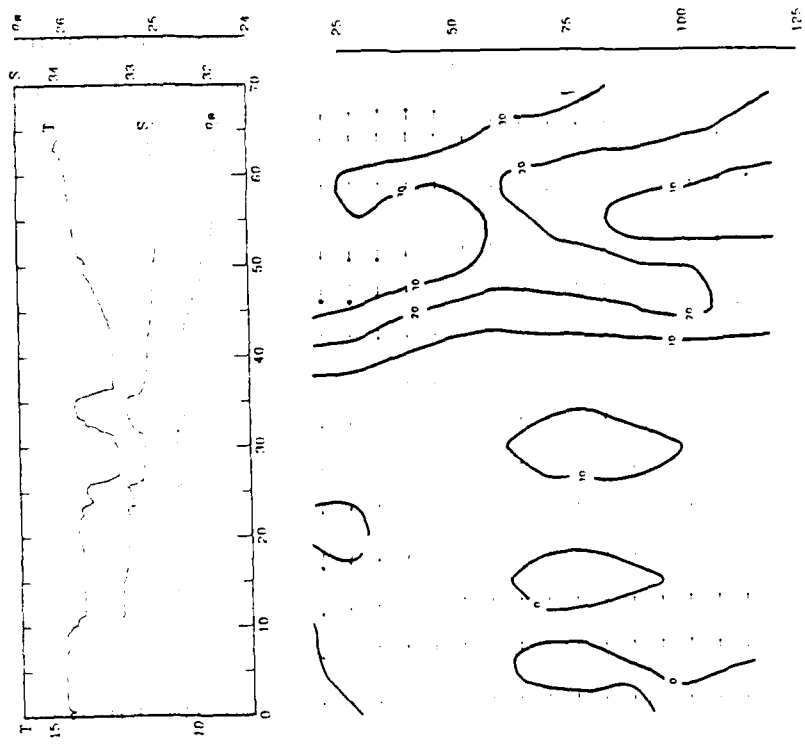
TRANSECT FROM 206/1200 TO 206/1930



TRANSECT FROM 205/19 11 TO 205/22 05

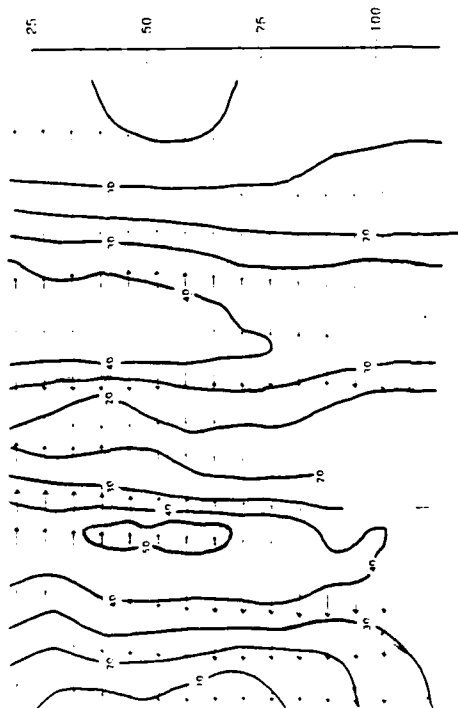
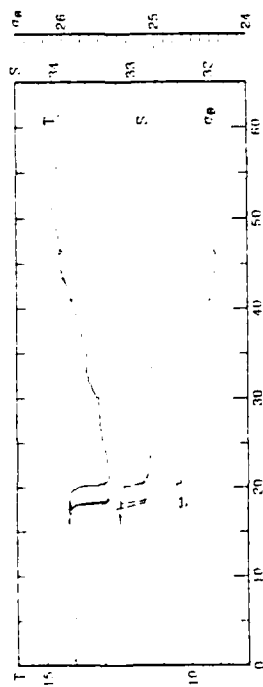


TRANSECT FROM 205/22 05 TO 206/03 30

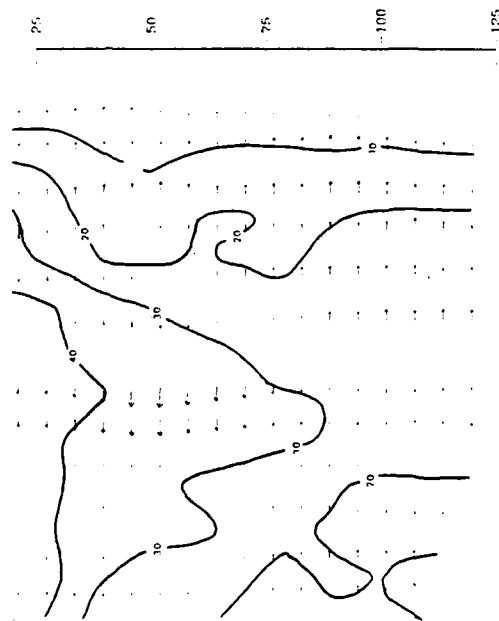
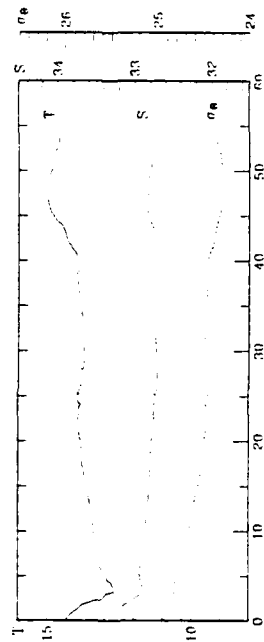


Figs. 7.21 : continued

TRANSECT FROM 204/22.00 TO 205/10.30

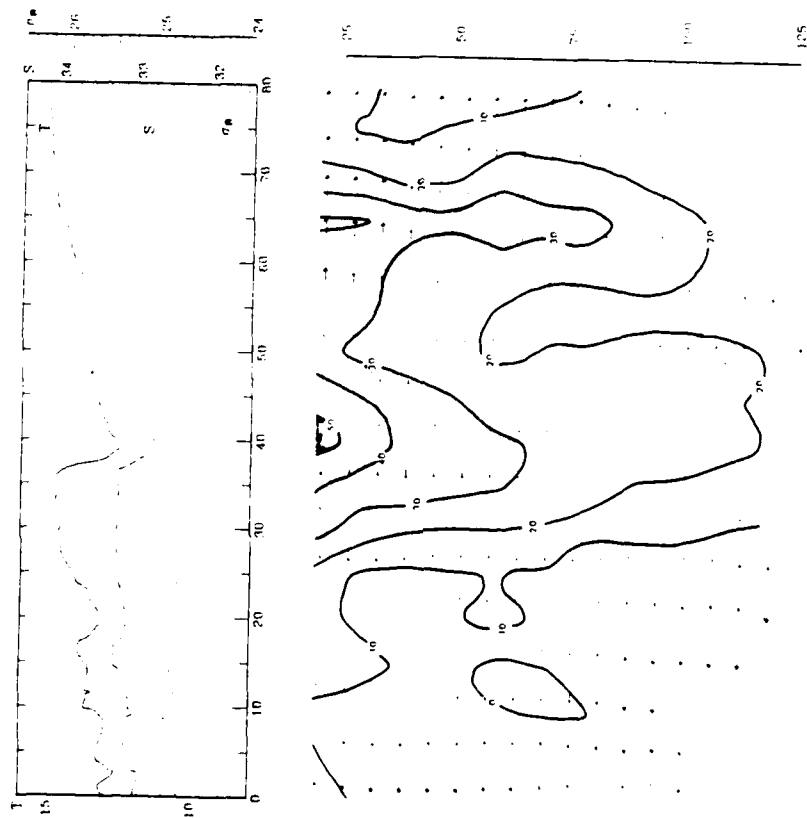


TRANSECT FROM 205/10.30 TO 205/14.50



Figs. 7.21 : continued

TRANSECT FROM 204/00 15 TO 204/15 00



Figs. 7.21 : Across-jet sections of along-jet currents through the cold tongue and adjacent waters. Also shown are the temperature, salinity and density (as σ_θ) at 5m depth from the underway thermosalinograph (data kindly made available by Pierre Flament, Libe Washburn and Larry Armi).

T-S diagram for jet survey, 204/08:15 to 206/19:30

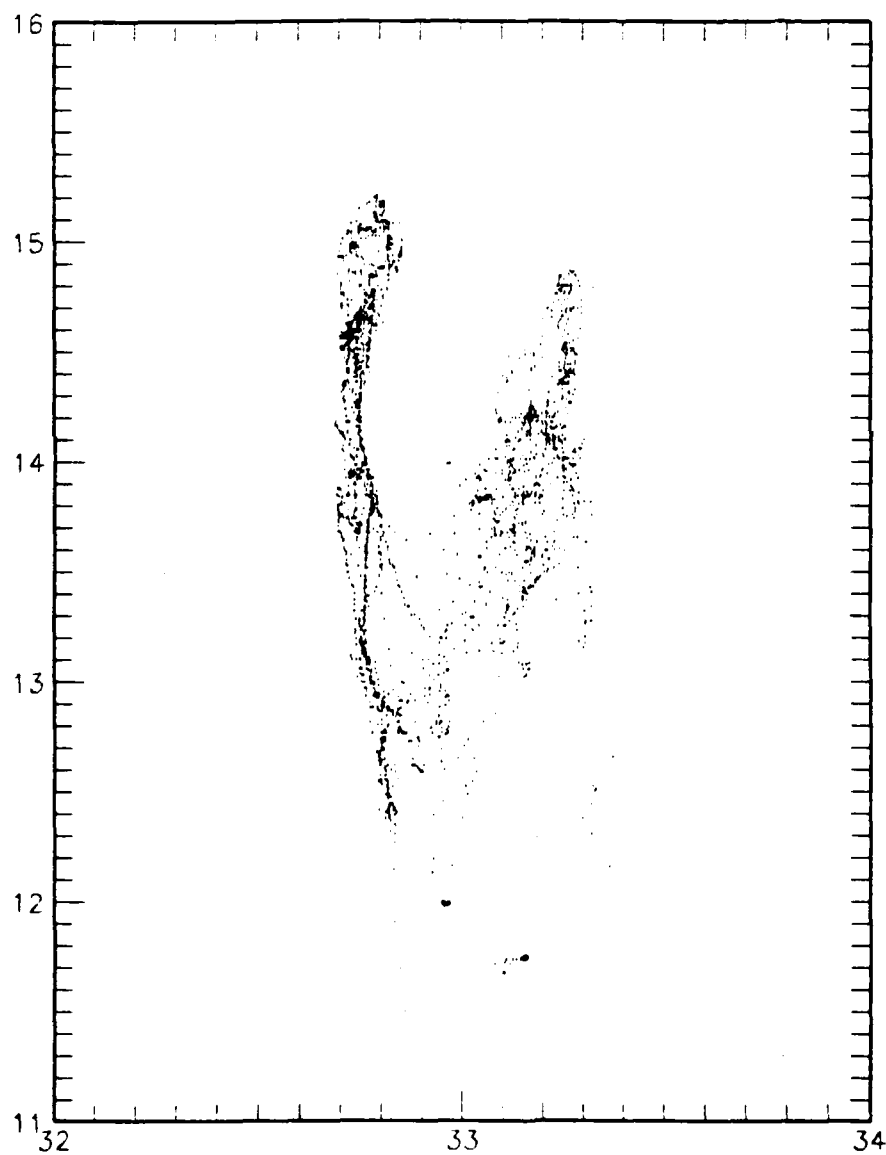


Fig. 7.20 : T-S diagram from underway thermosalinograph during jet survey (data kindly made available by Pierre Flament, Libe Washburn and Larry Armi). Sampling depth is approximately 5m.

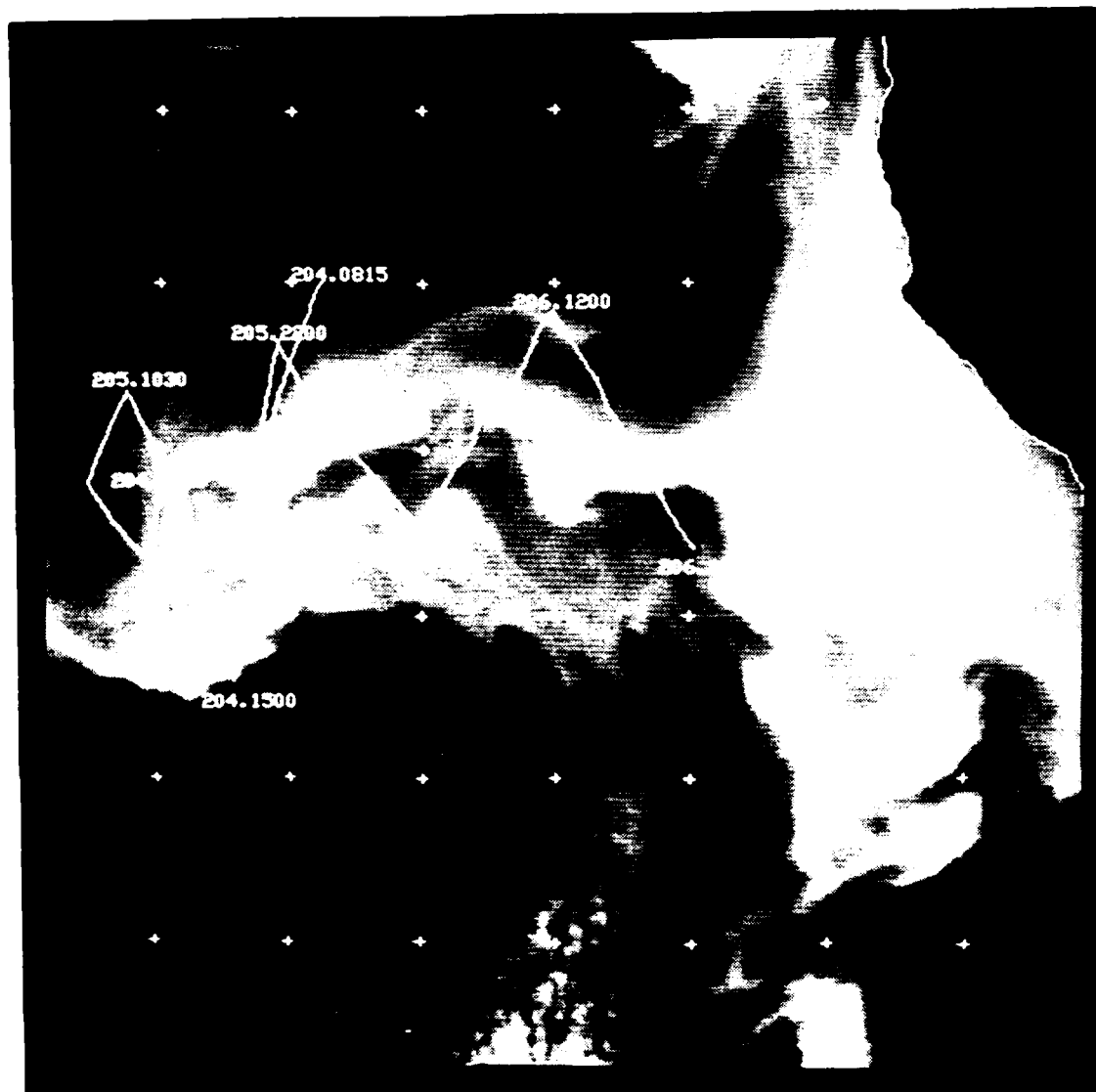


Fig. 7.19 : Ship track during 1982 offshore survey, indicating locations of sections through the cold water tongue. Clouds obscured the area during the actual survey time, and the location of the front and detailed structure of the temperature field were not available from satellite IR.

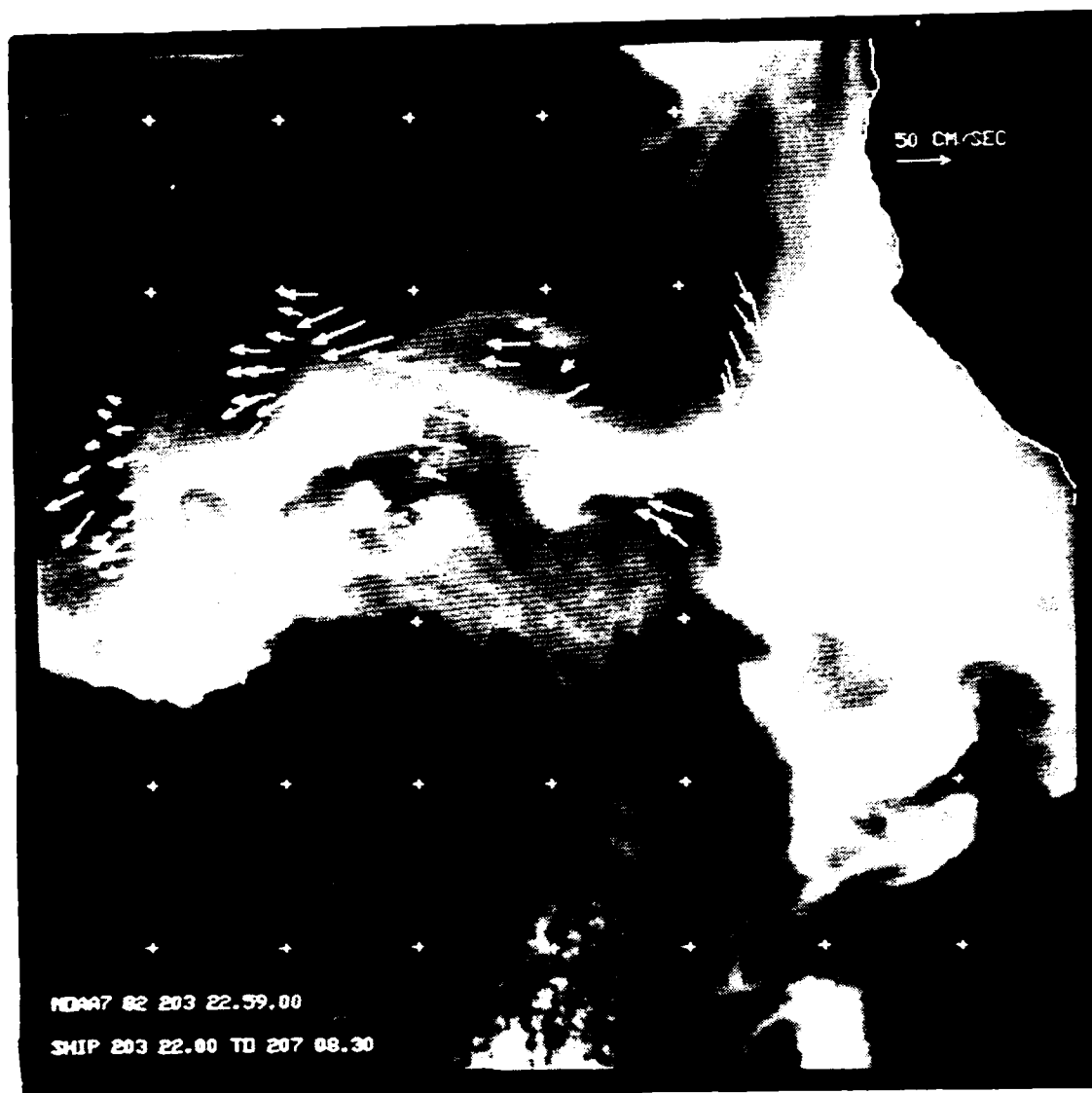


Fig. 7.18 : Currents at 28m depth from offshore survey of 22-26 July 1982, overplotted on NOAA7 IR image of sea surface temperature from 22 July.



Fig. 7.17 : Currents at 28m depth from offshore survey of 4-10 July 1981, overplotted on NOAA6 IR image of sea surface temperature from 8 July.



Fig. 7.16 : At least 4 large tongues of cold water are seen in this NOAA AVHRR image of sea surface temperature between Cape Mendocino and Pt. Conception (image provided by Pierre Flament).

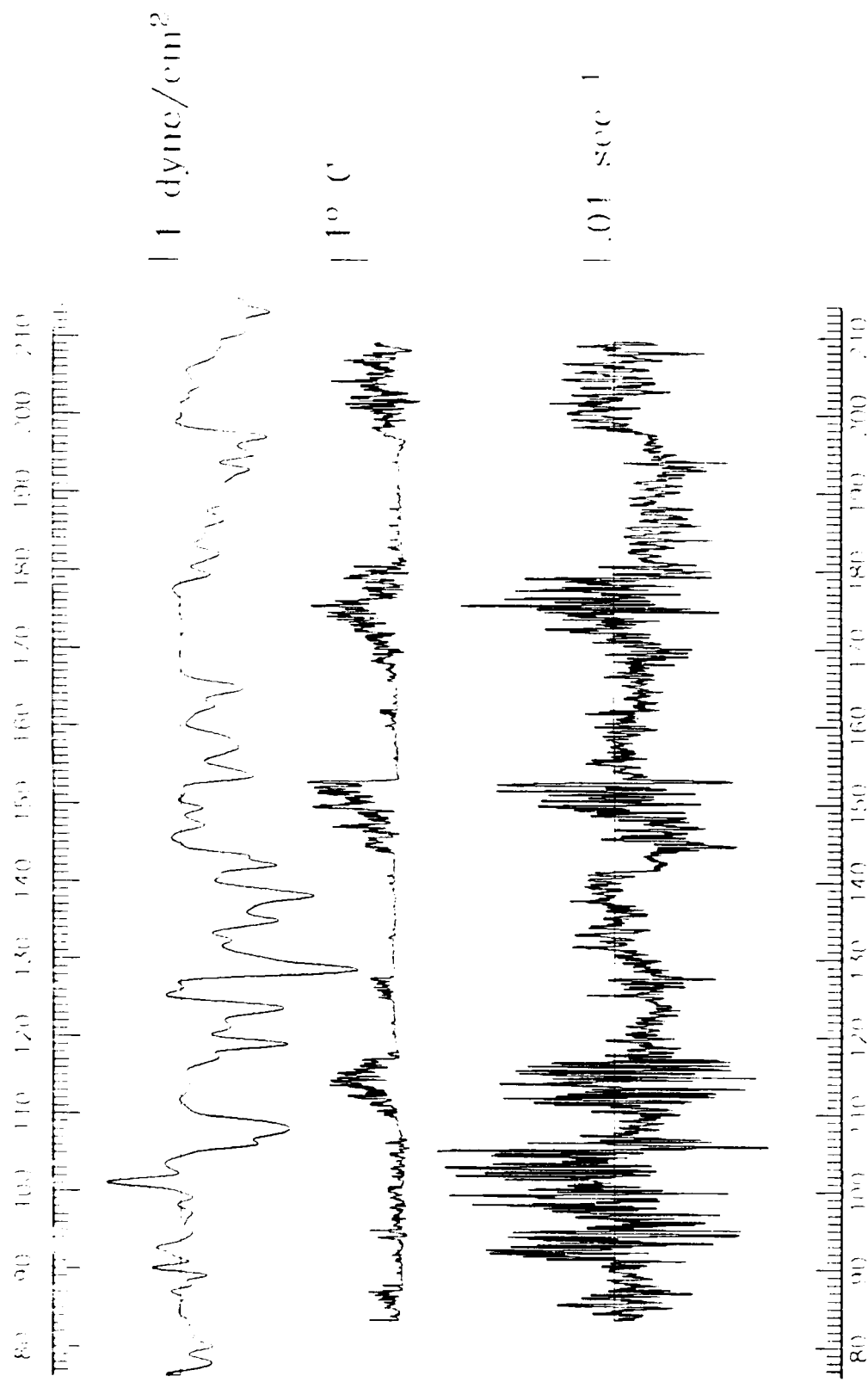


Fig. 7.15 : Time series of moored measurements showing alongshore component of wind stress τ at NDBO 46013, and temperature difference and $\partial v / \partial z$ between instruments at 5 and 10m depth at C3 vs day of 1982.

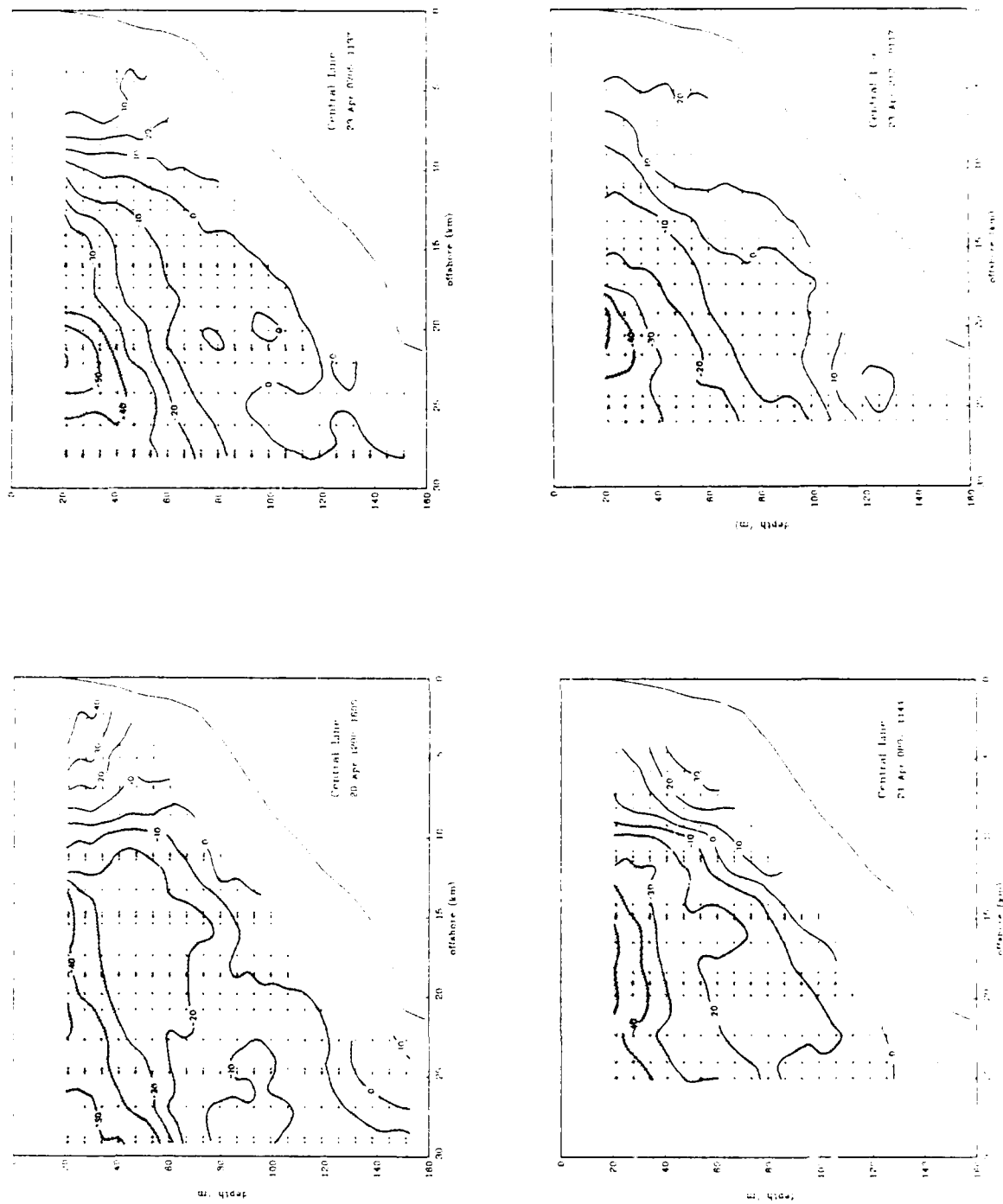


Fig. 7.14 : Cross-shelf sections of alongshore currents with depth for the four surveys of the Central line from 20-24 April.

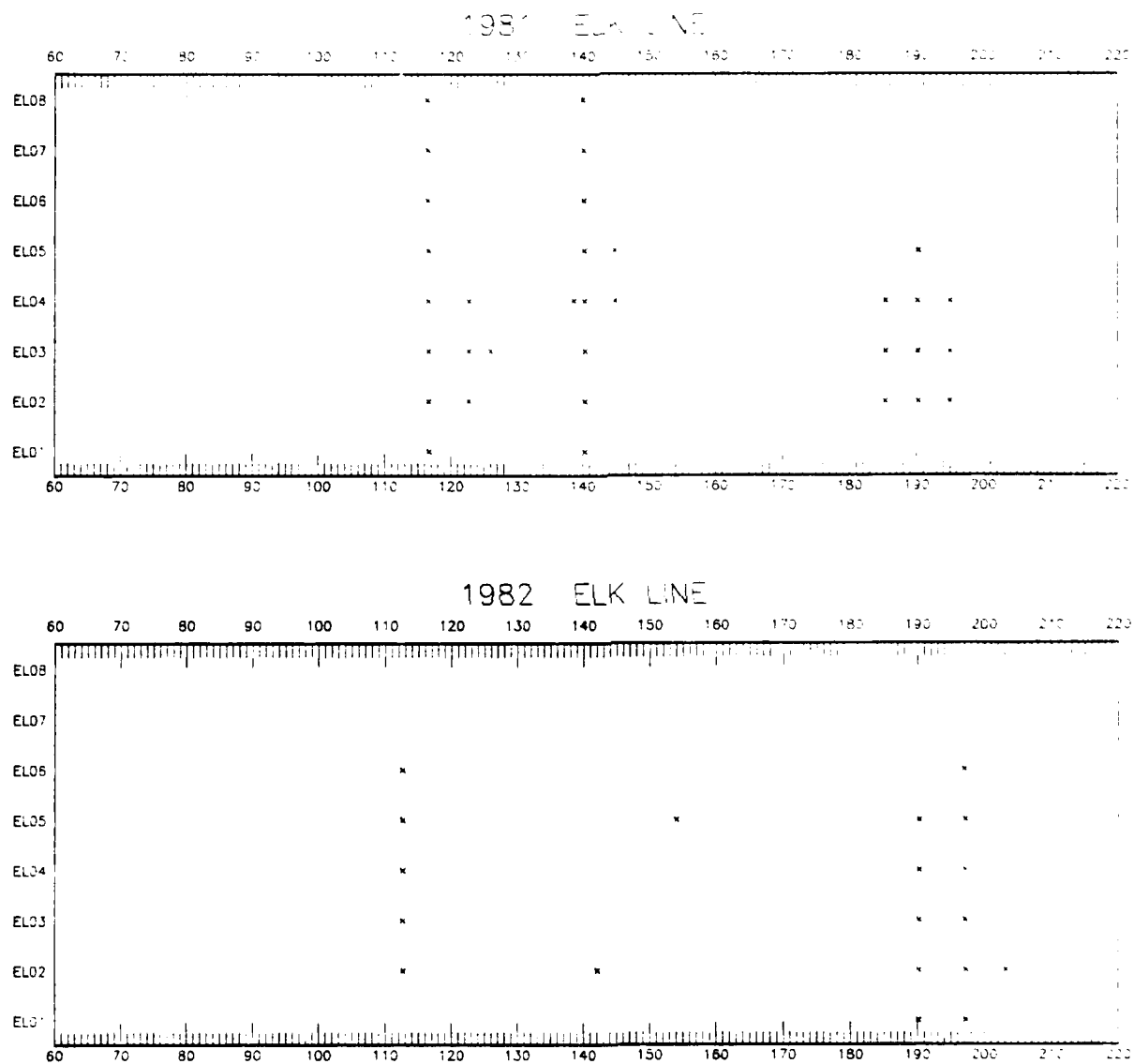


Fig. A.2 : Elk Line occupations vs. day of year.

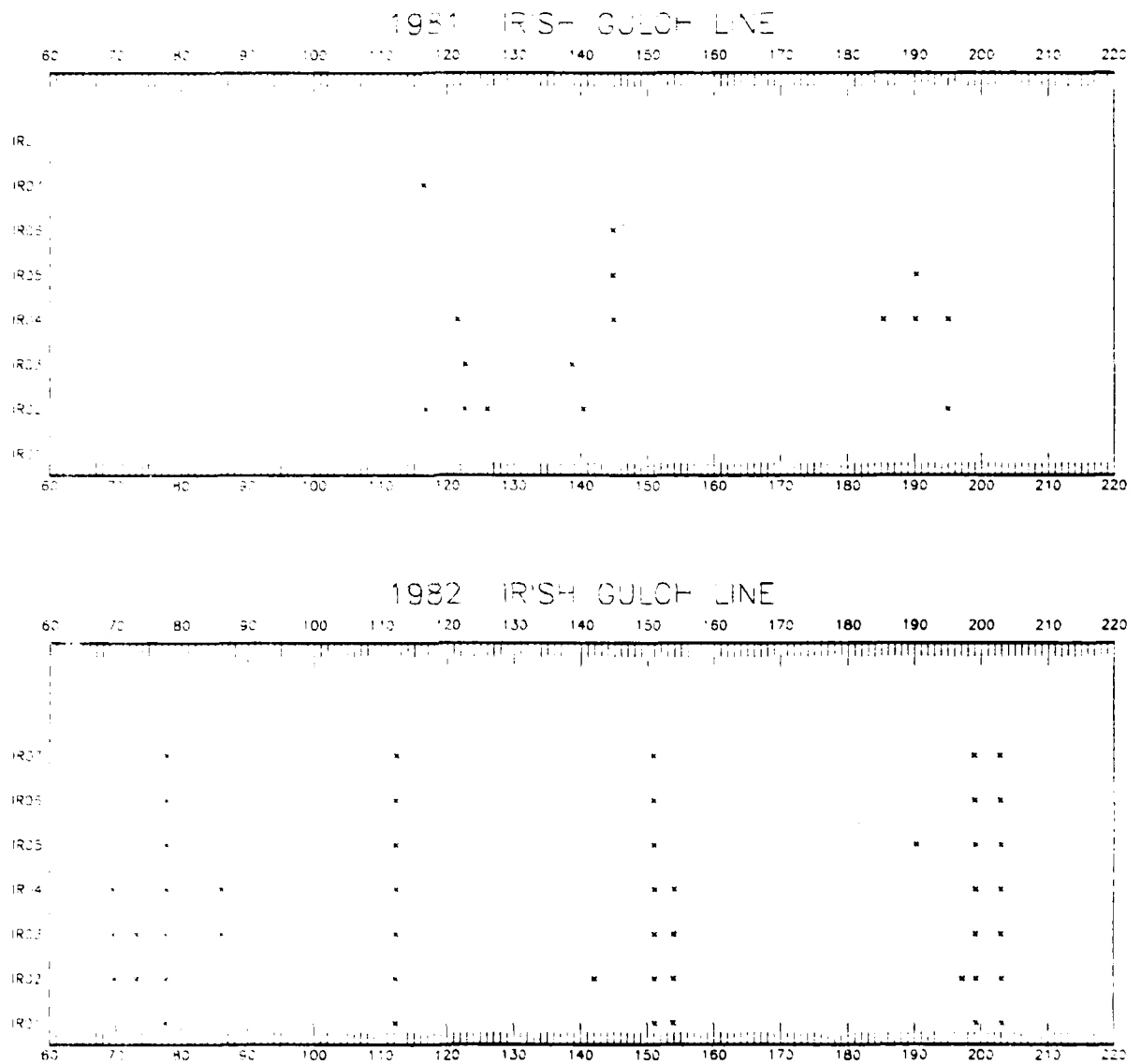


Fig. A.3 : Irish Gulch Line occupations vs. day of year.

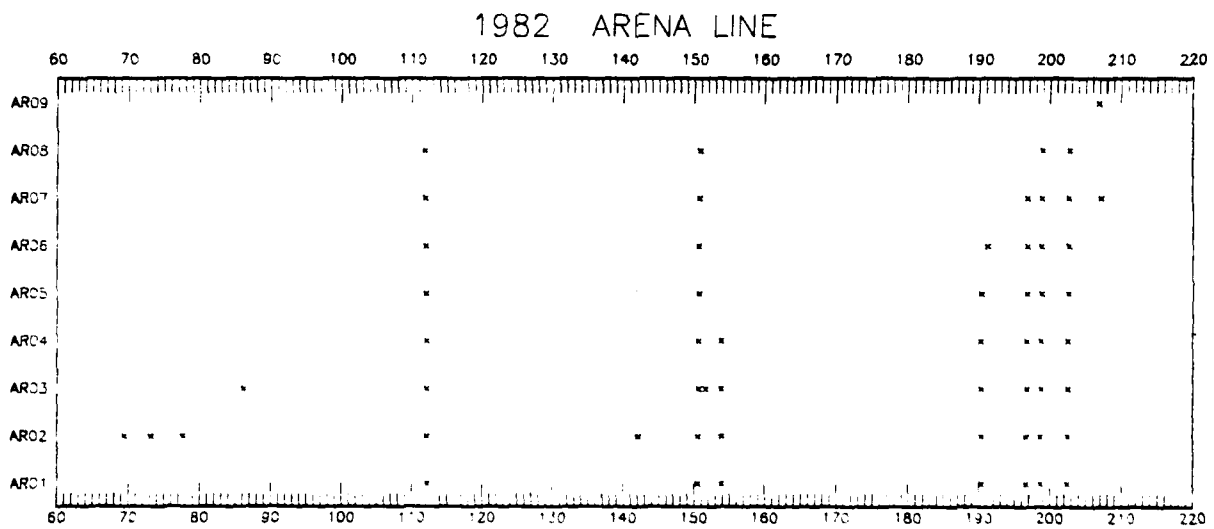
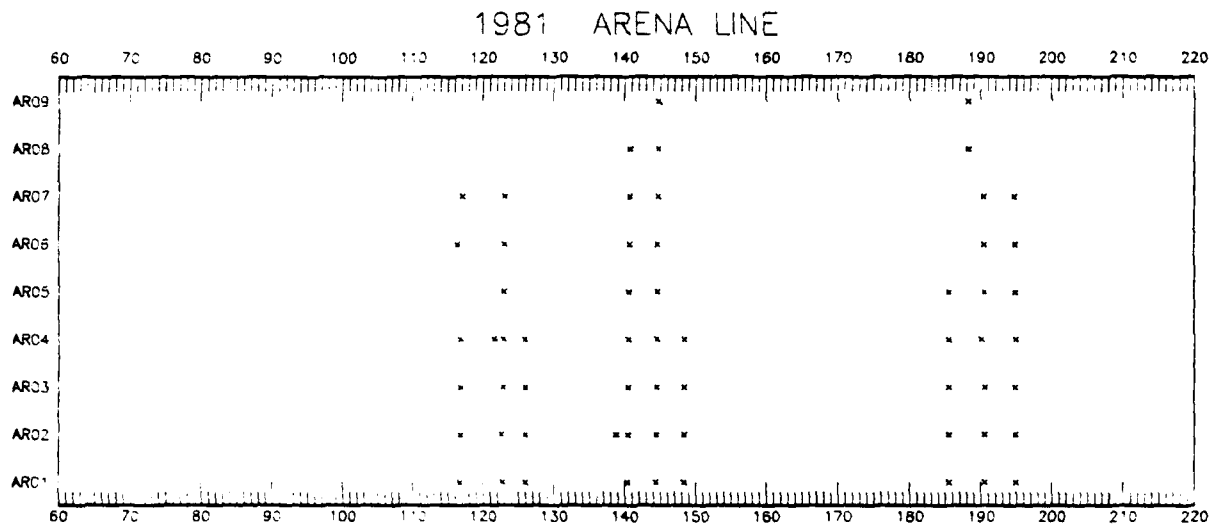


Fig. A.4 : Arena Line occupations vs. day of year.

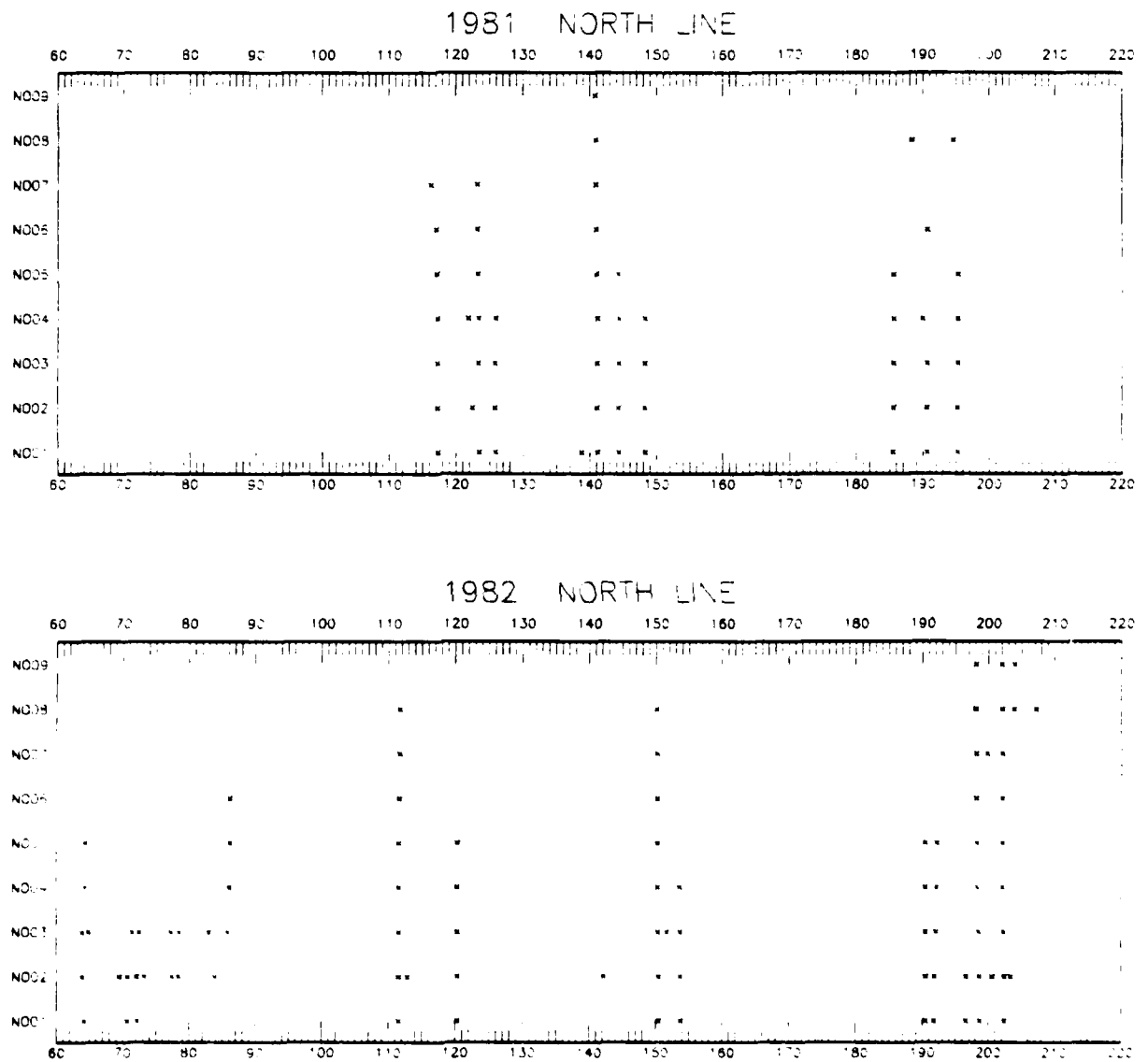


Fig. A.5 : North Line occupations vs. day of year.

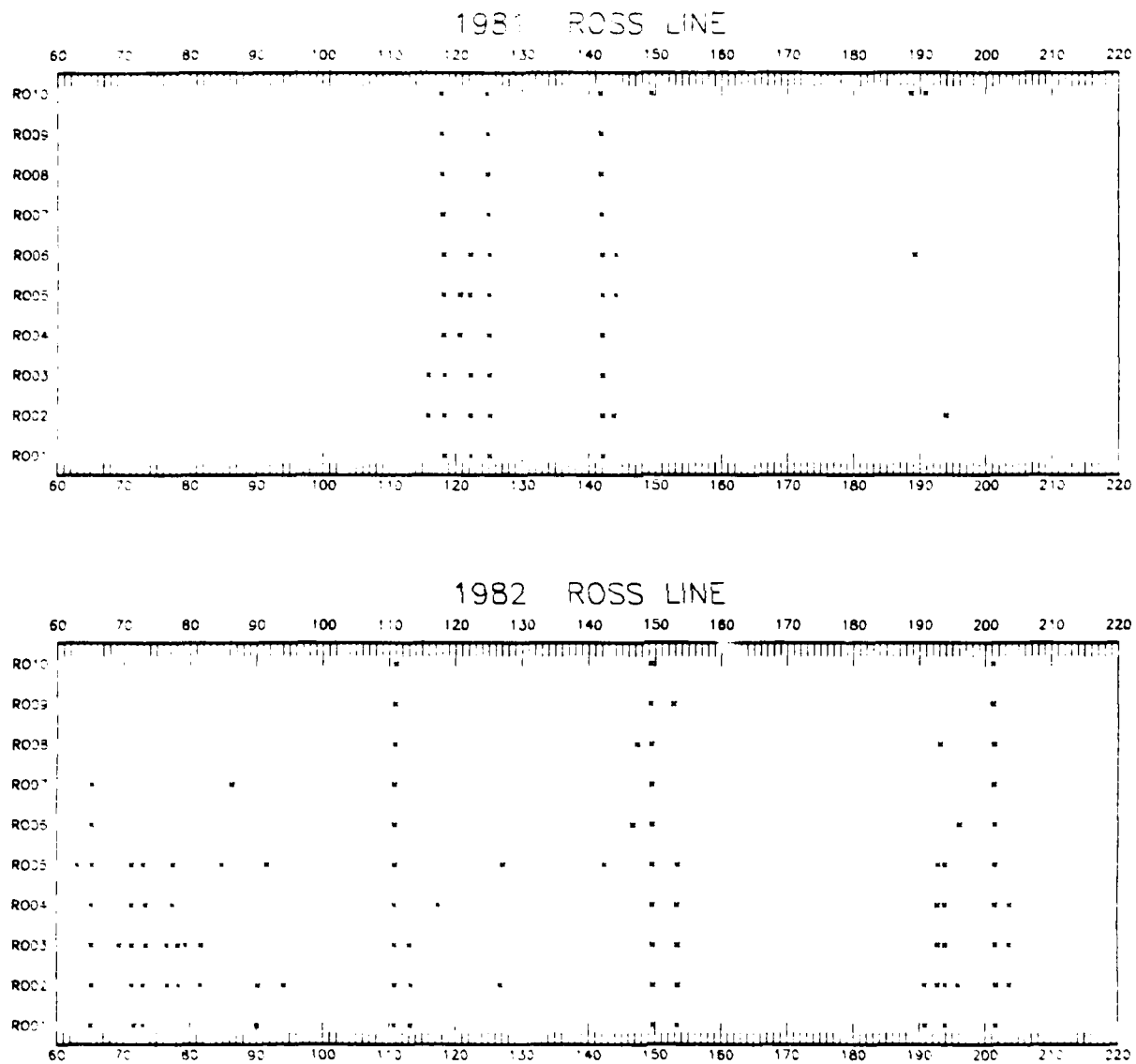


Fig. A.6 : Ross Line occupations vs. day of year.

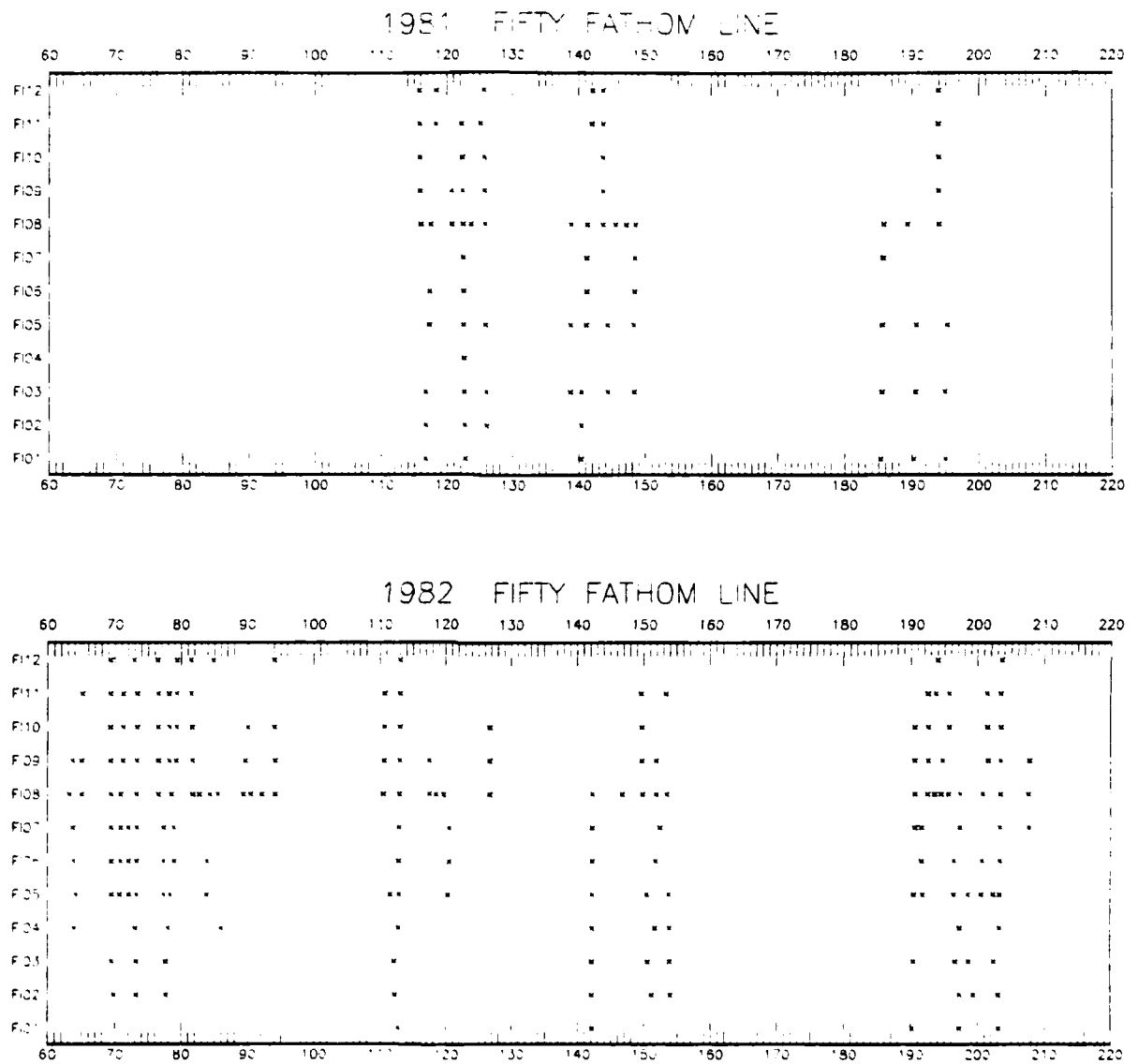


Fig. A.7 : Fifty Fathom Line occupations vs. day of year.

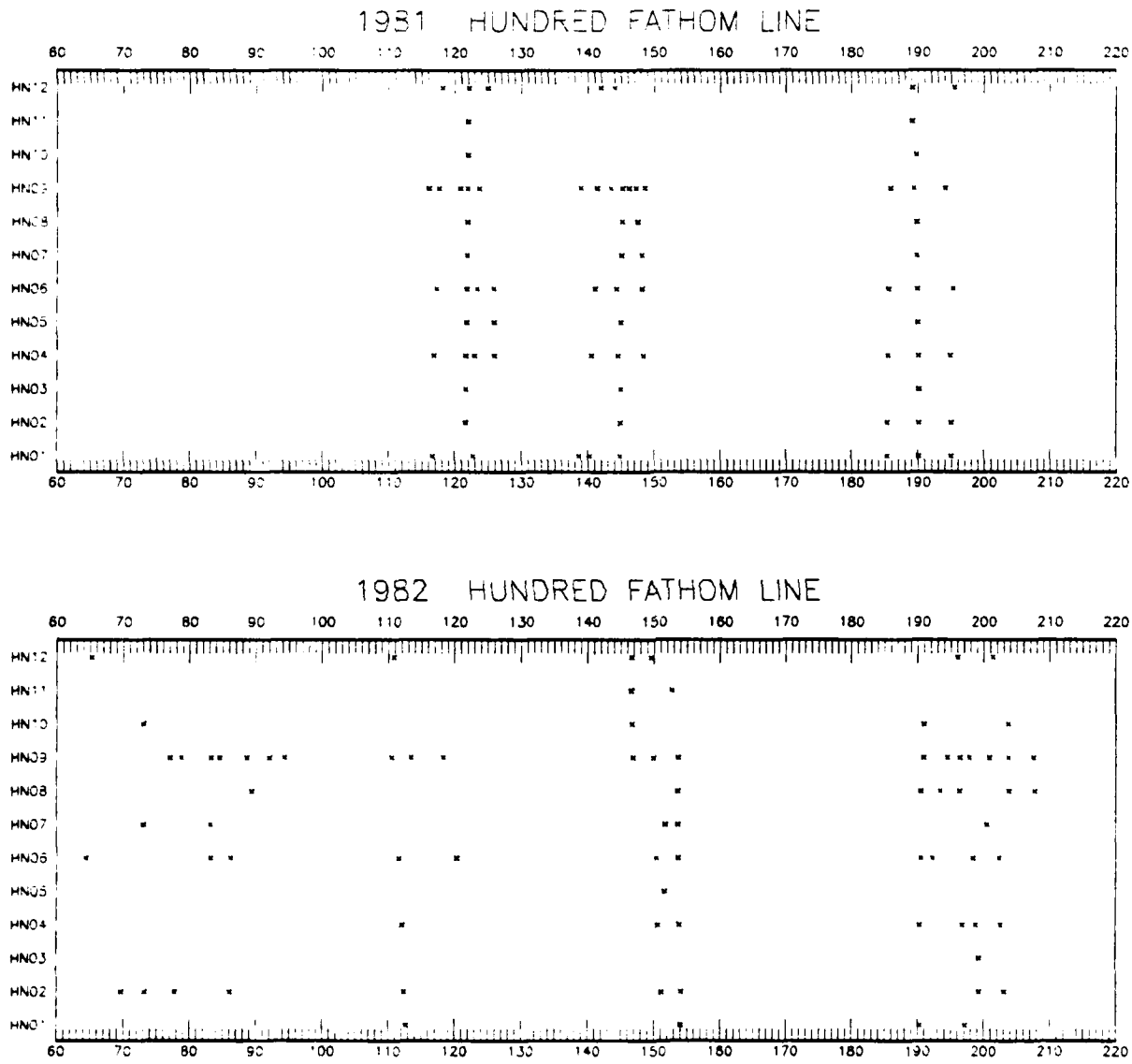


Fig. A.8 : Hundred Fathom Line occupations vs. day of year.

References:

- Allen, J. S., 1980: Models of wind-driven currents on the continental shelf. *Ann. Rev. Fluid Mech.*, **12**, 389-433.
- Arnold, R. W. and L. Maunder, 1961: *Gyrodynamics and its Engineering Applications*. Academic Press, New York, x + 484 pp.
- Bernstein, R. L., L. C. Breaker and R. Whritner, 1972: California Current eddy formation: ship, air and satellite results, *Science*, **195**, 353-359.
- Breaker, L. C. and R. P. Gilliland, 1981: A satellite sequence on upwelling along the California coast. In: *Coastal Upwelling*, F. A. Richards, ed., American Geophysical Union, Washington, D. C., pp. 87-94.
- Brink, K. H., 1983: The near-surface dynamics of coastal upwelling. *Prog. Oceanog.*, **12**, 223-257.
- Campbell, A.C., 1968: LORAN to Geographic Conversion and Geographic to LORAN Conversion. Informal Report IR No. N-3-64, 2nd printing, U.S. Naval Oceanographic Office.
- Chilowsky, C., 1932: Method and means for the observation and measurement of the speed of a vessel by directed beams of ultra-audible waves. U.S. Patent 1,864,638.
- Clay, C. S. and H. Medwin, 1977: *Acoustical Oceanography: Principles and Applications*. John Wiley and Sons, New York, xvii + 544 pp.
- Cochran, N. and D. D. Sameoto, 1983: Changes in acoustic backscattering intensity in response to ship's lights. *Trans. Amer. Geophys. Union*, **64**(52), 1023, abstract only.
- CODE Group, 1983: Coastal ocean dynamics. *Trans. Amer. Geophys. Union*, **64**, pp. 538-539.
- Davis, R. E., 1976: Predictability of sea surface temperature and sea surface pressure anomalies over the North Pacific Ocean. *J. Phys. Oceanog.*, **8**, 233-246.
- Davis, R. E., 1983: Current following drifters in CODE. Scripps Institution of Oceanography Ref. No. 83-4, 73 pp.

- Davis, R. L., 1984a: Drifter observations of coastal surface currents during CODE: the descriptive view, submitted to *J. Geophys. Res.*.
- Davis, R. L., 1984b: Drifter observations of coastal surface currents during CODE: the statistical and dynamical views, submitted to *J. Geophys. Res.*.
- Dean, W. N., 1978: Diurnal variations in LORAN-C groundwave propagation. Proceedings of the Ninth Annual Precise Time and Time Interval Applications and Planning Meeting, March 1978. NASA Technical Memorandum 78104. NASA, Goddard Space Flight Center, Greenbelt, MD, 20771.
- Fasham, M. J. R., 1976: Misalignment angle and calibration of a two-component electromagnetic log, *J. of Navigation*, **29**(1), 76-81.
- Fleischbein, J., W. E. Gilbert and A. Huyer, 1982: Hydrographic Data from the First Coastal Ocean Dynamics Experiment: Leg 4, 25 April - 7 May 1981. Oregon State University, School of Oceanography, Ref 82-2, 149pp.
- Fleischbein, J., W. E. Gilbert and A. Huyer, 1983: Hydrographic Data from the Second Coastal Ocean Dynamics Experiment: Leg 6, 18-24 April 1982. Oregon State University, School of Oceanography, Ref 83-4, 86pp.
- Huyer, A., 1983: Coastal upwelling in the California Current system, *Prog. Oceanog.*, **12**, 259-284.
- Huyer, A., 1984: Hydrographic observations along the CODE Central line off Northern California, 1981, *J. Phys. Oceanogr.* (in press).
- Huyer, A., E. J. C. Sobey and R. L. Smith, 1979: The spring transition in currents over the Oregon continental shelf, *J. Geophys. Res.*, **84**, 6995-7011.
- Huyer, A., J. Fleischbein and R. Schramm, 1984: Hydrographic Data from the Second Coastal Ocean Dynamics Experiment: R/V Wecoma, Leg 9, 6-27 July 1982. Oregon State University, School of Oceanography, Ref 84-7, 130pp.
- Johler, J. R., W. J. Keller, and L. C. Walters, 1956: "Phase of the Low Radio Frequency Ground Wave", NBS Circular 573, June 1956.
- Joyce, T. M. and M. C. Stalcup, 1984: An upper ocean current jet and internal waves in a Gulf Stream warm core ring, *J. Geophys. Res.*, **89**, 1997-2003.
- Joyce, T. M., D. S. Bitterman and K. E. Prada, 1982: Shipboard acoustic profiling of upper ocean currents, *Deep Sea Res.*, **29**, 903-913.
- Kelly, K. A., 1982: Infrared satellite data from the first Coastal Ocean Dynamics Experiment, March-July 1981. Scripps Institution of Oceanography Ref. 82-15, 58 pp.

- Kelly, K. A., 1983: Swirls and plumes or Application of statistical methods to satellite-derived sea surface temperatures. *Scripps Institution of Oceanography Ref.* 83-15, 210 pp. 87-94.
- Kundu, P. K. and J. S. Allen, 1976: Some three-dimensional characteristics of low-frequency current fluctuations near the Oregon coast. *J. Phys. Oceanogr.*, **6**, 181-199.
- Lhermitte, R., 1973. Meteorological Doppler radar. *Science*, **182**, 258-262.
- Markham, K. L., V. Piro, W. F. Shelton and M. W. Weston, Jr. 1984: Water Resources Data for California, Water Year 1982, Vol 2. Pacific Slope Basins from Arroyo Grande to Oregon State Line except Central Valley. U.S. Geological Survey, Water Resources Division, 417pp.
- Olivera, R. M., 1982: A complex distribution of water masses and related circulation off Northern California in July, 1981. Master's thesis, Oregon State University, 53pp.
- Pettigrew, N. R. and J. D. Irish, 1983. An evaluation of a bottom-mounted Doppler acoustic profiling current meter. *IEEE Proceedings of Oceans 83*, 182-186.
- Pinkel, R., 1980: Acoustic Doppler Techniques. In: *Air-Sea Interaction, Instruments and Methods*, F. Dobson, L. Hasse and R. Davis, eds. 171-200.
- Regier, L., 1982: Mesoscale current fields observed with a shipboard profiling acoustic current meter. *J. Phys. Oceanogr.*, **12**, 880-886.
- Reid, J. L. and A. W. Mantyla, 1976: The effect of geostrophic flow upon coastal sea elevations in the North Pacific Ocean. *J. Geophys. Res.*, **81**, 3100-3110.
- Rowe, F.D and J.W. Young, 1979: An ocean current profiler using Doppler sonar. *IEEE Proceedings, Oceans 79*: 292-297.
- Traganza, E. D., J. C. Conrad and L. C. Breaker, 1981: Satellite observations of a cyclonic upwelling system and giant plume in the California Current. In: *Coastal upwelling*, F. A. Richards, ed. American Geophysical Union, Washington, D. C., pp. 228-241.
- Wrigley, W., W. M. Hollister and W. G. Denhard, 1969: *Gyroscopic Theory, Design, and Instrumentation*. MIT Press, Cambridge, Mass., xiv + 444 pp.

END

FILMED

8-85

DTIC